

Thermal Transport and Photo-induced Charge Transport in Graphene

A Thesis
Presented to
The Academic Faculty

by

Daniel K. Benjamin

In Partial Fulfillment
of the Requirements for the Degree
Doctor of Philosophy

School of Physics
Georgia Institute of Technology
December 2011

Thermal Transport and Photo-induced Charge Transport in Graphene

Approved by:

Professor Zhigang Jiang
School of Physics
Georgia Institute of Technology, Chair

Professor Edward Conrad
School of Physics
Georgia Institute of Technology

Professor Andrew Zangwill
School of Physics
Georgia Institute of Technology

Professor Samuel Graham
School of Mechanical Engineering
Georgia Institute of Technology

Professor Phillip First
School of Physics
Georgia Institute of Technology

Date Approved: July 14, 2011

To my parents Leanne and Roy Benjamin.

And to my grandfather Joseph “Fred” Scoville for inspiring me.

ACKNOWLEDGEMENTS

I want to thank all the friends, advisers, professors, and others that have helped and encouraged me during my graduate school experience. I express my gratitude to all my committee members Dr. Phillip First, Dr. Edward Conrad, Dr. Samuel Graham, and Dr. Andrew Zangwill. I am forever grateful for the guidance and good nature of my PhD adviser Dr. Zhigang Jiang. He gave me renewed interest in physics, and without him I would not have accomplished my goals. I'll always be impressed by his incredible drive, knowledge, and willingness to lend a helping hand. I want to thank all of my labmates including Xunchi Chen, Jeff Chen for keeping my work experience interesting, and especially Wenlong Yu for being a great racquetball partner. I especially thank Dr. Anton Sidorov for all of his help performing the work done for this thesis, and the interesting discussions we've had. Also, I want to thank all of the undergrads I've worked with and mentored for reminding me how awesome it is to have a thirst for knowledge. I want to thank all my old buddies from Marchenkov's lab for having such a great time with me. Dr. Sanjay Bidisaria, Dr. Brandon Donehoo, Dr. Zhenting Dai, and especially Dr. John "Brooks" Howard all had the best of attitudes, in even the toughest of situations. I'm grateful for Dr. Andrew Zangwill seeing me through my years at Georgia Tech, and pointing me in the right direction. Finally, I want to thank my fiance Mary for always keeping me motivated, and being the best travel companion anybody in the world could have.

TABLE OF CONTENTS

DEDICATION	iii
ACKNOWLEDGEMENTS	iv
LIST OF TABLES	vii
LIST OF FIGURES	viii
SUMMARY	xii
I INTRODUCTION	1
1.1 Highlights of Graphene Properties	1
1.2 Applications of Graphene	3
1.3 Outline of the Thesis	7
II OVERVIEW OF GRAPHENE	8
2.1 Physical Properties of Graphene	8
2.2 Electronic Structure of Graphene	9
2.2.1 Calculation of the Band Structure of Graphene	9
2.2.2 Massless Dirac Fermions	12
2.2.3 Bilayer Graphene	15
2.3 Electric Field Effect	17
III EXPERIMENTAL	21
3.1 Mechanical Exfoliation	21
3.2 Chemical Vapor Deposition Growth	25
3.2.1 Transfer of CVD grown graphene	30
3.3 Raman Spectroscopy	34
IV THERMOELECTRIC POWER OF GRAPHENE	41
4.1 Theoretical Background	41
4.1.1 The Mott Formula for $S(T)$	42
4.1.2 Deviations From the Mott Formula	43
4.2 Experimental Setup	44
4.3 Results & Discussion	48
4.3.1 Vacuum Annealing	48

4.3.2	Sensing Applications	52
4.4	Conclusion	54
V	THERMAL CONDUCTIVITY OF GRAPHENE	56
5.1	Theoretical Background	57
5.1.1	Phonon Contribution to κ	58
5.2	Comparative Measurement of Thermal Conductivity	61
5.3	AFM Measurements	68
5.4	Conclusion	72
VI	PHOTOCONDUCTIVITY OF GRAPHENE IN HIGH MAGNETIC FIELDS . . .	73
6.1	Theoretical Background	73
6.2	Experimental Methods	77
6.2.1	Graphene on h-BN	78
6.2.2	Optical Measurement Setup	79
6.2.3	Modulation Technique for Photoconductivity	82
6.3	Results & Discussion	84
6.4	Conclusion	90
VII	CONCLUSION	91
	APPENDIX A — TECHNIQUES FOR GRAPHENE SAMPLE PRODUCTION . .	93
	REFERENCES	102
	VITA	110

LIST OF TABLES

3.1	Indices of refraction used to model graphene on an oxidized silicon wafer, and layer thicknesses.	23
4.1	Coefficients used to calibrated K-type thermocouple voltage vs. temperature as in Eq. (4.17).	47
5.1	Comparison of various measurements of thermal conductivity κ for graphene. . . .	56

LIST OF FIGURES

1.1	Graphene is a single sheet of carbon atoms arranged in a honeycomb lattice. Taking sections of graphene, other dimensional structures of carbon can be formed. It can be rolled into buckminster fullerenes (0D), or carbon nanotubes (1D), or stacked to form graphite (3D). Picture taken from [1].	2
1.2	Graphical illustration of Moore's law: the number of transistors in CPUs doubles every 24 months. Graph shows the evolution of the gate length in MOSFETs from the International Technology Road map for Semiconductors, and number of transistors per processor chip with the year. Picture from [2].	4
1.3	<i>Above:</i> Image of a two inch wafer of graphene, containing the fastest top gated FET transistors to date. <i>Below:</i> Schematic cross-section of a single epitaxial graphene transistor. Epitaxially grown (Si-face) graphene on top of SiC is gated using a HfO ₂ and Ti/Pd/Au contacts. <i>Right:</i> Current gain performance as a function of frequency, illustrating the cut-off frequency of 100 GHz. Picture adapted from [3].	6
1.4	(a) Example of CVD grown graphene based transparent electrode used for touch screens. (b) Optical transmittance for optical wavelengths shown for 1 - 4 layer graphene. (c) Sheet resistance for various optically transparent materials highlighting the superior performance of graphene. Picture adapted from [4].	7
2.1	(a) A small section of the real space crystal structure of graphene. Red and black dots indicate the two inequivalent basis atoms of the hexagonal lattice, which are usually defined as A and B in the literature. The blue arrows represent primitive lattice vectors, and the green arrows indicate the positions of the nearest neighbors of a single carbon atom. (b) The first Brillouin zone of the reciprocal space lattice, with the corresponding lattice vectors shown in blue. The zone is labeled with high symmetry points.	9
2.2	Electronic energy dispersion of graphene near one Brillouin zone. The vertical axis is the electron energy (in units of t) with $t = 2.7$ eV, and $t' = -0.2t$. A zoomed in view of the dispersion near one of the K or K' points is shown on the right side. . .	12
2.3	Top down view of a small section of bilayer graphene with AB (Bernal) stacking order. Solid lines show C-C bonding between carbon atoms in the top layer, and dashed lines showing C-C bonding between carbon atoms in the bottom layer. . .	16
2.4	(a) Plot of the low energy dispersion of bands in bilayer graphene given by Eq. (2.34), with $V = 0$. (b) Plot of the corresponding energy bands with a non-zero potential $V = 0.1$ eV.	17
2.5	Scanning electron micrograph of exfoliated graphene patterned into a hall bar structure. The lighter contrast areas on the edge of the graphene flake are metal contacts. The central graphene channel is 2 μ m wide.	18

2.6	Electron energy dispersion Dirac cones near a K point in graphene. As V_g is swept from negative to positive voltages (relative to the conductivity minimum), (a) there are filled electron states above the Dirac point, and (b) empty electron states below the Dirac point.	20
3.1	Stacking sequences of graphene sheets into three-dimensional graphite. Picture taken from [5].	22
3.2	(a) Optical microscope image of a mechanically exfoliated flake of graphene on an oxidized silicon wafer. The lightest color contrast area is monolayer graphene, with darker areas corresponding to bilayer and thicker few-layer graphene. (b) Schematic view of the graphene on this typical substrate, showing the normally incident light observed by a microscope.	23
3.3	Block Diagram of CVD growth system.	25
3.4	Schematic of CVD growth process showing process temperature versus time. The horizontal axis is not to scale.	27
3.5	Optical images of (a) as delivered copper foil from Alfa Aesar, and (b) copper foil after annealing with high temperature and H_2/Ar flow.	27
3.6	Optical images of graphene grown by the CVD process for short amounts of time.	29
3.7	Schematic showing the growth and transfer process of CVD grown graphene. (a) The CVD graphene growth process starts with a 99.8% pure copper foil (25 μm thick). (b) Graphene is grown on both surfaces by the CVD method described above. (c) A layer of polymer (950 MW PMMA) is spin coated onto one of the graphene cover surfaces. (d) A reactive ion etch using oxygen plasma removes the non-polymer coated graphene. (e) The copper is chemically etched away using $Fe(NO)_3$, leaving the polymer coated graphene floating in solution. (f) The graphene is fished out onto the desired substrate. (g) Final removal of the PMMA in acetone leaves the CVD graphene alone on the substrate.	31
3.8	Optical micrograph of CVD grown graphene transferred onto oxidized silicon wafer. Scale bar is 50 μm	33
3.9	Scanning electron micrograph of graphene coated with SiO_2 nanoparticles. Scale bar is 200 nm.	33
3.10	A typical Raman spectrum on CVD grown monolayer, taken from a single point on the sample.	35
3.11	(a) Raman processes in monolayer graphene (taken from [6]). Raman double-resonant processes for the G' peak in (b) monolayer graphene, and (c) bilayer graphene (taken from [7]).	36
3.12	G' peak in the Raman spectra of (a) monolayer CVD grown graphene, (b) bilayer exfoliated graphene, and (c) bilayer CVD grown graphene. The red curves are fits to a single Lorentzian peak (monolayer), and four Lorentzian peaks (bilayer). The green curves in (b) are the individual Lorentzian peaks used for the overall curve fit.	39

3.13	Two-dimensional mapping of the intensity of the D peak for a chain of three graphene crystal grains. <i>Inset</i> : Optical image of the area shown in the Raman mapping.	40
4.1	<i>Right</i> : Two-dimensional mapping of the Raman spectrum of the graphene sample used for the TEP measurement. The color contrast is the ratio of the peak intensities ($I_{G'}/I_G$). Panels (a)-(c) show selected spectra from individual points on the sample marked by circles.	45
4.2	(a) 3D diagram of the TEP measurement setup with electrical connections and measured voltage responses. (b) Circuit diagram for the same measurement setup.	46
4.3	Optical micrograph of the junction between bare Alumel and Chromel wires, forming a K-type thermocouple.	47
4.4	Simultaneous measurements of (a) the Seebeck coefficient S and temperature T , (b) sample resistance R and T , and (c) S and T during the annealing process. . . .	50
4.5	Electronic band structure lineup of graphene with its surroundings for (a) ambient conditions and (b) the degassed SiO_2 substrate.	51
4.6	Response of the thermoelectric power of graphene upon exposure to various gaseous species.	53
4.7	Change of the resistance of CVD graphene samples with the introduction of water (blue) and blood (red).	54
5.1	Dispersion of the phonon modes of graphene calculated using the valence-force field method. Taken from [8].	59
5.2	Grüneisen parameters for each phonon mode in graphene, calculated <i>ab initio</i> using the quasiharmonic approximation in density-functional perturbation theory. Taken from [9].	60
5.3	(a) Schematic of the sample setup for the (all electrical) measurement of the thermal conductivity of graphene. (b) Photograph of an actual measured sample mounted on the sample stage.	64
5.4	<i>Left</i> : Typical thermocouple response. <i>Right</i> : Corresponding ratio of thermocouple voltages.	65
5.5	Temperature dependence of κ_{gr} for supported CVD grown graphene on glass. Blue squares represent data taken during cooling from room temperature. Red circles are data taken while warming from the lowest to the highest achievable temperatures.	66
5.6	Temperature dependence of κ_{gr} for supported CVD grown graphene on SiO_2/Si . Black circles show the upper boundary limit for κ_{gr} , while red circles show the lower boundary limit. The solid blue line is a fit of the data to our theoretical model.	67
5.7	(a) Block diagram outlining the measurement setup for SThM mode (from Park website: www.parkafm.com). (b) SEM image of a microfabricated SThM cantilever and tip.	69

5.8	<i>Left</i> : AFM topographic mapping of CVD graphene on gold. <i>Right</i> : Thermal conductivity contrast mapping of the same region.	70
5.9	Various AFM measurements on the same chain of three single crystal grains of graphene on Si/SiO ₂ . The <i>top middle</i> image is an optical micrograph taken with the camera mounted on the AFM. All other images are labeled with their respective mode.	71
6.1	(a) Energy spectrum for quantized Landau levels. (b) Corresponding density of states for electrons in graphene in a magnetic field.	75
6.2	Quantized Hall conductivity for graphene in high magnetic field and low temperature. The red/black curves show measurements from the lowest/highest gate voltages swept in the given directions.	76
6.3	(a) Photograph of linear polarizer and aperture for laser conditioning and alignment. (b) Infrared photograph of the same setup. (c) Infrared photograph of the same setup with the laser beam on.	80
6.4	(a) Optical setup for the photoconductivity measurement. Measurement schemes for (b) single modulation, and (c) double modulation.	81
6.5	Measured photoresponse and longitudinal voltage for graphene in a magnetic field. The photoconductivity features appear at the edge of the QH states as labeled. . .	85
6.6	Contour map showing the photoresponse as a function of magnetic field and gate voltage.	86
6.7	Lock-in response of the longitudinal voltage (black curve), and the Hall voltage (red curve) measured at frequency $\omega = 2\omega_{\text{ch}}$. Photoresponse (blue curve) measured at frequency ω_{ch} (scaled by 500 \times). Measurement taken at $T = 4.2$ K, and $B = 35$ T, with an excitation frequency $\omega = 2\omega_{\text{ch}}$	88
6.8	Photoresponse of monolayer graphene on h-BN at odd integer values of magnetic field between 1 T and 35 T. The black lines are visual guides tracking the $\nu = \pm 1$ QH states.	89
A.1	Final thickness of spin coated PMMA versus angular speed. The graph shows three concentrations (% anisole) of the solvent. Taken from the Microchem data sheet. .	95
A.2	Optical micrograph of a graphene flake coated by PMMA. The +’s on the right side are alignment mark that have been exposed and developed in the resist.	97
A.3	Optical micrograph of a Hall bar patterned onto a graphene flake after the plasma etch of exposed graphene.	97
A.4	Optical micrograph of a graphene/gold contact lines after developing the PMMA. .	98
A.5	Optical micrograph of the graphene Hall bar, with gold contact lines after evaporation.	99
A.6	Optical micrograph of a graphene device after wire bonding to the gold contact pads.	100
A.7	Optical micrograph of a Hall bar patterned onto a graphene flake after the developing the PMMA.	101

SUMMARY

The electronic material graphene has attracted much attention for its unique physical properties such as, linear band structure, high electron mobility, and room temperature ballistic conduction. The possibilities for device applications utilizing graphene show great variety, from transistors for computing to chemical sensors. Yet, there are still several basic physical properties such as thermal conductivity that need to be determined accurately.

This work examines the thermal properties of graphene grown by the chemical vapor deposition technique. The thermoelectric power of graphene is studied in ambient and vacuum environments and is shown to be highly sensitive to surface charge doping. Exploiting this effect, we study the change in thermoelectric power due to introduction of gaseous species. The temperature dependent thermal conductivity of graphene is measured using a comparison method. We show that the major contribution to the thermal conductivity is the scattering of in-plane phonons.

Graphene also shows promise as an optoelectronic material. We probe the Landau level structure of graphene in high magnetic fields using a differential photoconductivity technique. Using this method we observed the lifting of spin and valley degeneracies of the lowest Landau level in graphene.

CHAPTER I

INTRODUCTION

There has been much excitement about graphene since it was first discovered as one of the few truly two-dimensional crystals. It has become such an important and popular research topic for physicists that the 2010 Nobel Prize in physics was awarded to two of its pioneer researchers from the University of Manchester, Andre Geim and Konstantin Novoselov. The number of citations for graphene journal articles is increasing exponentially, and researchers from many fields outside of physics recognize its potential. This introduction will give a sampling of properties of graphene that make it so desirable, and highlight possible applications for the material for the present and the future.

1.1 Highlights of Graphene Properties

Graphene is made entirely of carbon atoms. It is the missing link in the various forms of carbon materials ranging from 0D (Bucky balls) to the commonplace 3D graphite (pencil lead). Figure (1.1) shows the various forms of carbon materials, and emphasizes the fact that any of the other structures can be thought of as being derived from a sheet of graphene. The past thirty years have seen continuing efforts pursuing 2D carbon crystals via different mechanisms [1]. It is argued that small 3D warping out of the 2D plane (wrinkles, ripples, etc.) leads to an overall minimization of the total free energy making it thermodynamically stable. It is also remarkable that suspended graphene structures have long range crystalline order and still display this out-of-plane deformation (~ 1 nm) [10].

The fact that graphene is entirely made of carbon has the potential to make it one of the cheapest electronic materials, due to the overwhelming abundance of carbon on Earth. Currently, small samples of graphene in the tens of thousands of square microns cost about \$1,000, but the cost is decreasing very rapidly. Furthermore, methods of epitaxial growth (SiC sublimation, chemical vapor deposition (CVD) growth) are providing means for large scale production of graphene making

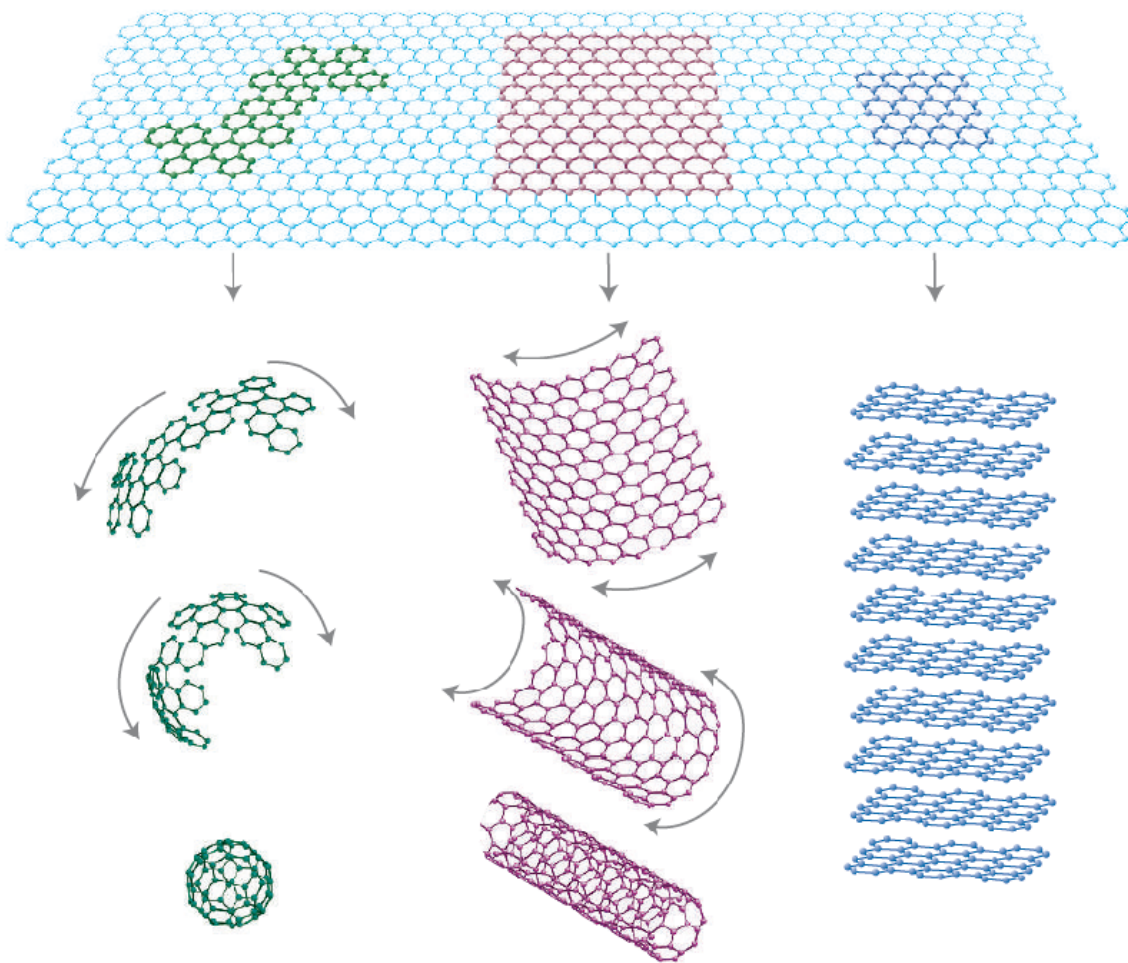


Figure 1.1: Graphene is a single sheet of carbon atoms arranged in a honeycomb lattice. Taking sections of graphene, other dimensional structures of carbon can be formed. It can be rolled into buckminster fullerenes (0D), or carbon nanotubes (1D), or stacked to form graphite (3D). Picture taken from [1].

it more efficient, and more attractive to industrial developers. Especially in the case of CVD grown graphene, the starting materials have a minimal cost compared to that of the SiC wafers required for the sublimation method, but as yet have lesser quality.

There are several electrical properties of graphene that theoretically would make for very powerful electronic devices. Electron mobility in graphene is exceptionally high approaching $\mu \sim 60,000 \text{ cm}^2 \text{ V}^{-1} \text{ s}^{-1}$ in some devices [11]. This high mobility is due to the very low scattering rate of charge carriers in graphene, and relatively temperature independent even up to room temperature. In some cases this provides samples with mean free path lengths on the order of 10s of microns, which is significantly larger than the present day gate lengths of transistors in most electronic devices. Furthermore, graphene can carry an exceptionally large amount of current. The breakdown current density of some graphene nanoribbon devices is in the range of 10^8 A/cm^2 [12].

Mechanically, monolayer graphene is one the strongest materials ever measured, with a Young's modulus of $E = 1.0 \text{ TPa}$ (for comparison steel has $E = 200 \text{ GPa}$), with a breaking strength of 43 N m^{-1} [13]. Although this property is only for the in-plane, one could envision a composite using graphene which could exploit this property. Graphene is chemically inert to most substances and requires extremely harsh chemicals to oxidize. Graphene is also very well transparent, with a single layer absorbing only $\pi\alpha \approx 2.3\%$ of white light, ($\alpha \approx 1/137$ is the fine structure constant) [14]. For few to several layers the optical transparency is proportional to the number of layers, with each layer decreasing the transmission by $\pi\alpha$.

These are some of the major properties that have led to much research towards applications using graphene. This is not a full exposition of all the properties of graphene, but serves to highlight how graphene can be used to engineer new and exciting devices and products.

1.2 Applications of Graphene

As discussed above, there are several material properties of graphene that make it very appealing for engineers and physicists alike. This section illustrates some of the major applications and devices that could be made possible with graphene. Some devices have already been realized at an early stage of development, but the possibilities are endless and are becoming closer to reality as research in this field advances.

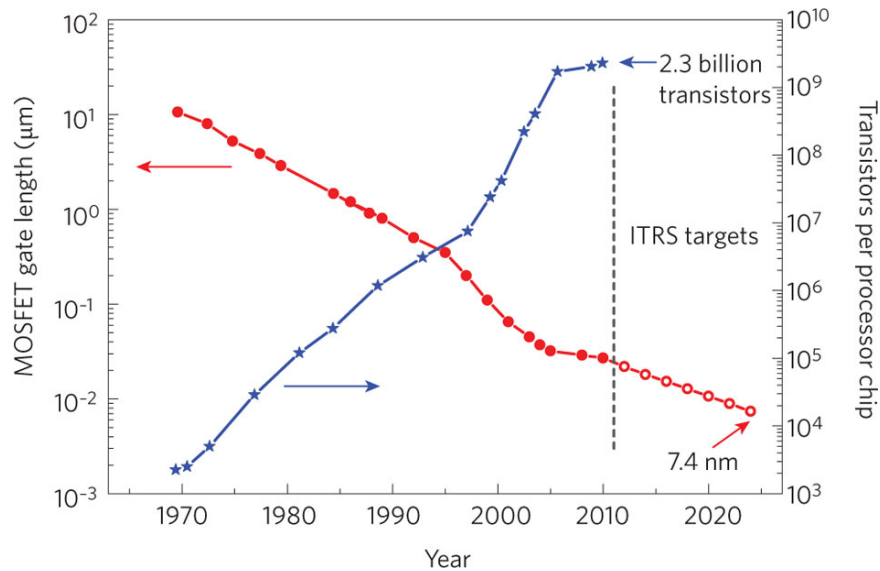


Figure 1.2: Graphical illustration of Moore's law: the number of transistors in CPUs doubles every 24 months. Graph shows the evolution of the gate length in MOSFETs from the International Technology Road map for Semiconductors, and number of transistors per processor chip with the year. Picture from [2].

Today's world is driven by technology more than at any time in the past. Almost every American owns a personal electronic device of some kind, be it a PC, a smart phone, a flat panel television, or anything else. The internet is becoming more interactive all the time with the advent of social media, cloud computing, and mobile sharing. And so, the demand for increasingly fast computing, ever smaller devices, and increased functionality (all at a cheap price) have become the major drivers of technology and thus research and development.

Today, we still live in a silicon world, where almost every integrated circuit (IC) you would find is a tiny chip of silicon wafer containing thousands to millions of transistors and other circuit elements. It is often quoted that we are reaching the physical limits of silicon, and there is a huge question about what will be the next step in electronics evolution to maintain the pace of advancement. Gordon Moore, the co-founder of Intel corporation, famously posited, "The number of transistors incorporated in a chip will approximately double every 24 months." The main driver is miniaturization of individual transistors, the building block of an IC. Scientists and engineers have come up with ingenious means for maintaining this standard, including immersion lithography, phase shift optical masks, extreme-UV exposure, and so on. Furthermore, as the dimensions of individual transistors shrink, the heat flux density increases exponentially. This degrades the

electrical performance of the devices, and if not handled effectively can destroy them.

These technical challenges require imagination and skill to handle, but at a certain point the physical limitations of the materials become insurmountable. Fortunately, researchers are working all the time on possible successors to silicon as the material of choice for electronics. In fact, carbon is a leading candidate for this, including carbon nanotubes (CNTs) and graphene. Graphene in particular is attractive because of its 2D nature, which would readily allow for integration of the material into current integrated circuit processing paradigms.

There have been several reports of transistors fabricated with graphene, with the fastest transistor to date having a cut-off frequency of 100 GHz [3] using epitaxial graphene with a HfO_2 gate insulator. Figure 1.3 shows the realization of these high-speed transistors. The mobility for charge carriers in the channel of a graphene metal-oxide semiconductor (MOS) have reached as high as $23,600 \text{ cm}^2 \cdot \text{V}^{-1} \cdot \text{s}^{-1}$. As will be discussed, graphene is a zero-bandgap semimetal. Transistor operation requires a bandgap to allow for switching between zero current/finite current states (off/on). There are several possibilities for producing a bandgap in graphene: creating 1D nanoribbons, electrically biasing bilayer graphene, and inducing strain being the most promising. Nanoribbons on the order of 10s of nanometers in width can produce bandgaps that are roughly inversely proportional to the width ($E_g = 200 \text{ meV}$ for $w < 20 \text{ nm}$). Also, since graphene has such a larger thermal conductivity ($\kappa \sim 1,800 \text{ W/m}\cdot\text{K}$) they have a greatly reduced need for extra heat removal by active (energy consuming) methods.

There are still many technical challenges to be overcome. Fabricating clean zigzag or armchair edges at the few nanometer width scale, free of disorder, is not possible presently. To obtain bandgaps on the same order as the nanoribbons, for bilayer graphene, requires quite large electric fields $\sim 10^7 \text{ V/cm}$ [15]. The requirements for uniaxial strain are larger than 20% for the onset of a bandgap in graphene [16] which is also difficult to create practically. Further, the effects of the contacts aren't fully understood. The lowest reported metal-graphene contact resistances are still no better than $\lesssim 1,000 \Omega\cdot\text{cm}$ [17]. Even with these problems, building graphene transistors shows enough promise to warrant funding from several industrial companies like Intel, IBM, etc.

Beyond graphene transistors, there are several more exotic applications. The next most promising is the use of graphene as transparent electrodes. The current industry standard for touch screen

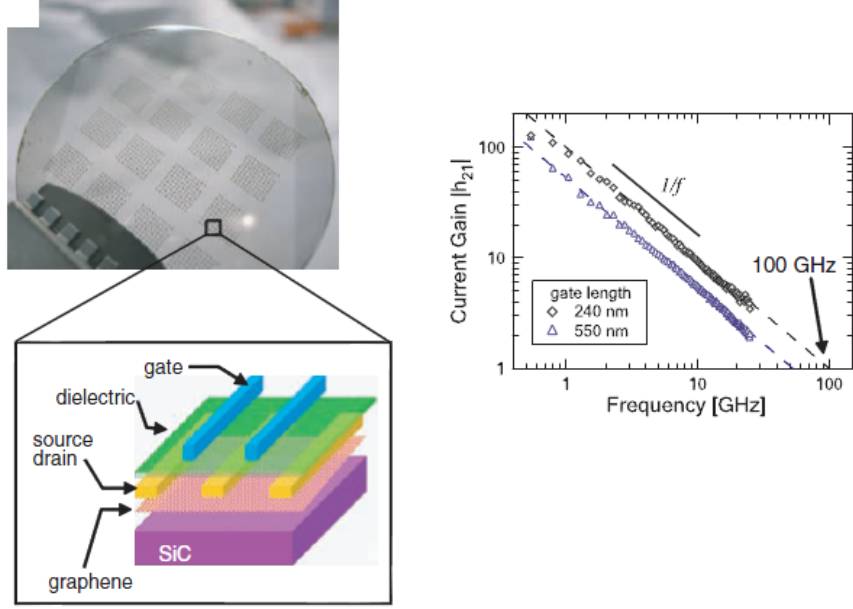


Figure 1.3: *Above:* Image of a two inch wafer of graphene, containing the fastest top gated FET transistors to date. *Below:* Schematic cross-section of a single epitaxial graphene transistor. Epitaxially grown (Si-face) graphene on top of SiC is gated using a HfO_2 and Ti/Pd/Au contacts. *Right:* Current gain performance as a function of frequency, illustrating the cut-off frequency of 100 GHz. Picture adapted from [3].

technology is indium-tin-oxide (ITO), which is expensive to manufacture due to the cost of indium. The trade off is between transparency and electrical resistivity. A Korean group has fabricated monolayer CVD grown graphene for use in transparent electrodes with sheet resistances of $125 \, \Omega \, \square^{-1}$ and 97.4% optical transmittance [4]. An optimum compromise between high transmission and low resistivity is reached with $30 \, \Omega \, \square^{-1}$ and $\sim 90\%$ transparency. So not only does graphene provide better performance than ITO, but at a cheaper cost. Figure 1.4 shows the fabricated device, with the corresponding performance characteristics.

Further, graphene has been proposed as a material for use in gas sensing. Using the change in resistance of graphene with adsorbed gas molecules, it has shown sensitivity to single gas molecules of NO_2 [18]. It will be shown later in this thesis, there exists another material property, thermoelectric power (TEP), which we argue is a better gas sensing paradigm. Graphene has been used as a nanomechanical resonator with mass detection to less than $2 \, \text{zg} = 2 \times 10^{-21} \, \text{g}$ [19], which equals that for carbon nanotubes and has superior strength to tearing. There is also interest in various forms of conductive paper using graphene and graphene oxides, again with superior tensile strength [20].

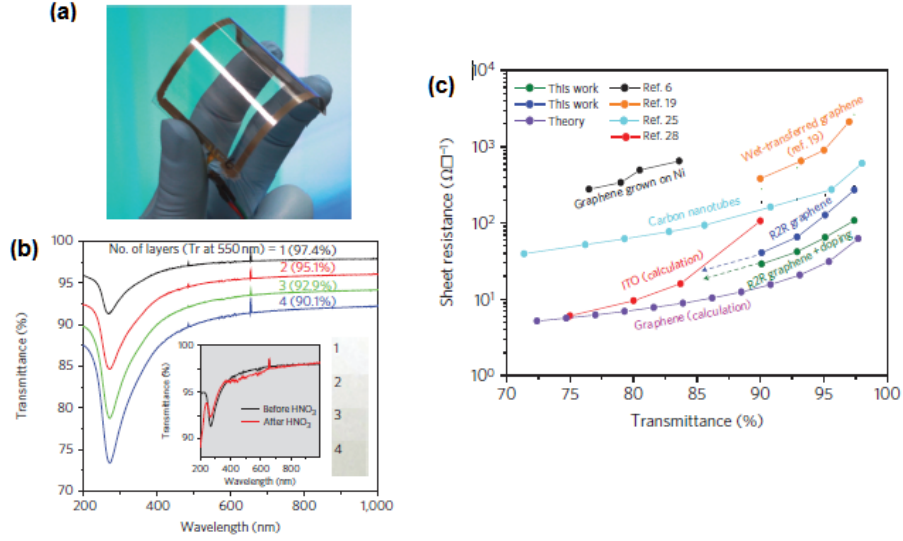


Figure 1.4: (a) Example of CVD grown graphene based transparent electrode used for touch screens. (b) Optical transmittance for optical wavelengths shown for 1 - 4 layer graphene. (c) Sheet resistance for various optically transparent materials highlighting the superior performance of graphene. Picture adapted from [4].

1.3 Outline of the Thesis

This thesis presents work on thermal and electronic properties of graphene. The basic properties of graphene which relate to this work will be reviewed. An overview of the method of chemical vapor deposition growth of graphene will be presented along with experimental techniques used to characterize this material in chapter 3. The remaining chapters will discuss the main areas of research for this thesis. Chapter 4 will discuss the thermoelectric power of CVD graphene and its use for gas sensing. Chapter 5 will present a novel measurement of thermal conductivity on CVD graphene. Finally, chapter 6 will present photoconductivity spectroscopy measurements on the Landau level structure of exfoliated graphene.

CHAPTER II

OVERVIEW OF GRAPHENE

2.1 *Physical Properties of Graphene*

In its purist form, graphene is a single atomic layer of carbon atoms arranged in a honeycomb lattice. Each individual carbon atom forms sp^2 hybridized bonds to three other carbon atoms, with dangling π electron orbitals perpendicular to the plane of the lattice. The carbon-carbon bond length is $a_0 = 1.42 \text{ \AA}$. The thickness of a graphene sheet is usually quoted as $d = 3.35 \text{ \AA}$. This is the distance along the c -axis direction, between planes of graphene in Bernal stacked (AB stacking) graphite. The real space crystal structure of graphene is described by a unit cell containing two inequivalent carbon atoms. These inequivalent atoms are labeled by different colors in Figure 2.1. Any two equivalent carbon atoms are connected by a translation vector $\mathbf{R} = n_1 \mathbf{a}_1 + n_2 \mathbf{a}_2$, where \mathbf{a}_1 and \mathbf{a}_2 are the primitive lattice vectors. In the coordinate system of Figure 2.1, they can be written as:

$$\mathbf{a}_1 = \sqrt{3}a_0(1, 0), \quad (2.1)$$

and

$$\mathbf{a}_2 = \sqrt{3}a_0\left(\frac{1}{2}, \frac{\sqrt{3}}{2}\right). \quad (2.2)$$

The three nearest neighbors are given by: $\delta_1 = a_0(0, 1)$, $\delta_2 = a_0(-\sqrt{3}/2, -1/2)$, and $\delta_3 = a_0(\sqrt{3}/2, -1/2)$. There are six next-nearest neighbors located at: $\pm\mathbf{a}_1$, $\pm\mathbf{a}_2$, and $\pm(\mathbf{a}_1 - \mathbf{a}_2)$.

The hexagonal lattice in real space also gives rise to a hexagonal lattice in reciprocal space. The reciprocal lattice vectors \mathbf{b}_j are defined from the condition that $\mathbf{a}_i \cdot \mathbf{b}_j = 2\pi\delta_{ij}$. They are given by:

$$\mathbf{b}_1 = \frac{4\pi}{3a_0}\left(\frac{\sqrt{3}}{2}, -\frac{1}{2}\right), \quad (2.3)$$

and

$$\mathbf{b}_2 = \frac{4\pi}{3a_0}(0, 1). \quad (2.4)$$

From these vectors, we can construct the Brillouin zone (BZ) by forming perpendicular bisectors of these reciprocal lattice vectors. This construction is shown in Figure 2.1(b), and gives a hexagonal

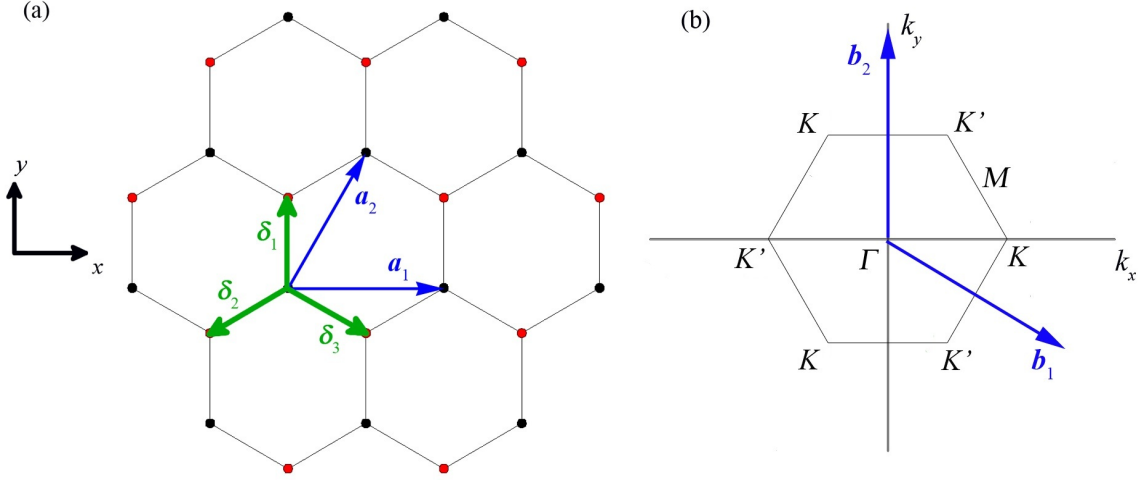


Figure 2.1: (a) A small section of the real space crystal structure of graphene. Red and black dots indicate the two inequivalent basis atoms of the hexagonal lattice, which are usually defined as A and B in the literature. The blue arrows represent primitive lattice vectors, and the green arrows indicate the positions of the nearest neighbors of a single carbon atom. (b) The first Brillouin zone of the reciprocal space lattice, with the corresponding lattice vectors shown in blue. The zone is labeled with high symmetry points.

BZ, with a few key high symmetry points. The Γ point is at the zone center, and there are two inequivalent points at the corners of the zone, labeled by K and K' . As will be shown later, these points give rise to the intriguing electronic behavior in graphene. The last interesting point is the M point located midway between points K and K' along the zone boundary.

2.2 Electronic Structure of Graphene

2.2.1 Calculation of the Band Structure of Graphene

Carbon atoms have four valence electrons. In graphene, three of these valence electrons form the hybridized sp^2 bonds with the three nearest neighbors. The fourth electron is considered in the $2p_z$ state, and is free for conduction. The resulting band structure of graphene can then be determined using the standard tight binding approximation. This calculation was first performed by Wallace in 1947 [21] in the context of understanding the electronic structure of graphite, and later widely cited in the studies of carbon nanotubes and graphene.

If we take the normalized wavefunction for the $2p_z$ orbital as $X(\mathbf{r})$, then the tight binding wave function can be written as

$$\psi = \varphi_1 + \lambda\varphi_2, \quad (2.5)$$

where

$$\varphi_1 = \sum_A e^{ik \cdot \mathbf{r}_A} X(\mathbf{r} - \mathbf{r}_A), \quad (2.6)$$

and

$$\varphi_2 = \sum_B e^{ik \cdot \mathbf{r}_B} X(\mathbf{r} - \mathbf{r}_B). \quad (2.7)$$

The A and B in the sums refer to all the atoms reached by lattice translations from the two inequivalent carbon basis atoms. It can be shown that these wavefunctions satisfy the conditions for Bloch's theorem for a periodic lattice.

In this basis we can construct the band structure $E(\mathbf{k})$ under the tight-binding approximation. It is assumed that the overlap between wavefunctions centered on different atoms is zero, so that

$$\int X(\mathbf{r} - \mathbf{r}_A) X(\mathbf{r} - \mathbf{r}_B) d^3\mathbf{r} = 0. \quad (2.8)$$

The rest of the calculation involves solving the equation

$$\mathbf{H}\psi = E(\mathbf{k})\psi, \quad (2.9)$$

with the wavefunction defined by Eq. (2.5). The non-trivial solutions to this equation are given by the secular equation

$$\det[\mathbf{H} - E(\mathbf{k})\mathbf{S}] = 0, \quad (2.10)$$

where \mathbf{S} is the overlap matrix with elements given by

$$S_{ij} = \int \varphi_i^* \varphi_j d^3\mathbf{r}. \quad (2.11)$$

Under our previous assumption Eq. (2.8), we know that $S_{AB} = S_{BA} = 0$. If we further assume that the wavefunctions ψ are properly normalized, we can write $S_{AA} = S_{BB} = 1$. In this case $\mathbf{S} = \mathbf{I}$, the 2×2 identity matrix. And we simplify the problem to finding the standard eigenvalues/eigenvectors of the 2×2 Hamiltonian matrix \mathbf{H} .

The matrix elements of \mathbf{H} are given by

$$H_{ij} = \int \varphi_i^* H \varphi_j d^3\mathbf{r}. \quad (2.12)$$

The diagonal elements of this matrix are just the energy of the $2p_z$ orbital for the lattice sites A and B . Due to the crystal symmetry, we set the elements $H_{AA} = H_{BB}$. Furthermore, we can define

this element as the zero point of the energy scale, leaving $H_{AB} = H_{BA}^*$ as the energy due to the interactions between the crystal atoms. The off diagonal elements are computed in Wallace's paper, and take the form

$$H_{AB} = -t(\exp[i\mathbf{k} \cdot \boldsymbol{\delta}_1] + \exp[i\mathbf{k} \cdot \boldsymbol{\delta}_2] + \exp[i\mathbf{k} \cdot \boldsymbol{\delta}_3]) = -tf(\mathbf{k}), \quad (2.13)$$

where $t > 0$ is the hopping integral for an electron to move between nearest neighbors (different sub lattices) only. More explicitly,

$$t = \int X^*(\mathbf{r} - \boldsymbol{\delta})(U - V)X(\mathbf{r}) d^3\mathbf{r} \approx 2.7 \text{ eV}, \quad (2.14)$$

where $\boldsymbol{\delta}$ is one of the nearest neighbor vectors defined above, U is the potential for an isolated carbon atom, and V is the periodic potential of the lattice [22]. Plugging in for the definition of each $\boldsymbol{\delta}_i$, one obtains the explicit form for H_{AB} :

$$H_{AB} = -t \left[\exp(ik_y a_0) + 2 \cos\left(k_x \frac{\sqrt{3}a_0}{2}\right) \exp\left(-ik_y \frac{a_0}{2}\right) \right]. \quad (2.15)$$

Using this expression in the secular equation (2.10) gives the desired energy

$$E_{\pm}(\mathbf{k}) = \pm t \sqrt{1 + 4 \cos^2\left(k_x \frac{\sqrt{3}a_0}{2}\right) + 4 \cos\left(k_x \frac{\sqrt{3}a_0}{2}\right) \cos\left(k_y \frac{3a_0}{2}\right)} = \pm t \sqrt{3 + f(\mathbf{k})}, \quad (2.16)$$

where the function $f(\mathbf{k})$ has been defined as

$$f(\mathbf{k}) = 2 \cos(\sqrt{3}k_x a_0) + 4 \cos\left(k_x \frac{\sqrt{3}a_0}{2}\right) \cos\left(k_y \frac{3a_0}{2}\right). \quad (2.17)$$

This calculation can be expanded to included next-nearest neighbors. In this case one must consider hopping between those next-nearest neighbors (within the same sublattice), with a corresponding energy given by $t' \approx 0.1 \text{ eV}$ [23] (defined similarly to that of Eq. (2.14) with the replacement of $\boldsymbol{\delta}$ by a next-nearest neighbor vector). In this expanded calculation, the energy dispersion is then given by [22]

$$E_{\pm}(\mathbf{k}) = \pm t \sqrt{3 + f(\mathbf{k})} - t' f(\mathbf{k}). \quad (2.18)$$

In both cases, the \pm signs refer to either the π -bonding state ($-$ sign), or the π^* -antibonding state ($+$ sign).

Based on Eq. (2.18), a three-dimensional plot of the energy dispersion can be obtained by taking the energy E as the vertical axis, and (k_x, k_y) as the horizontal axes. This plot is shown in Figure

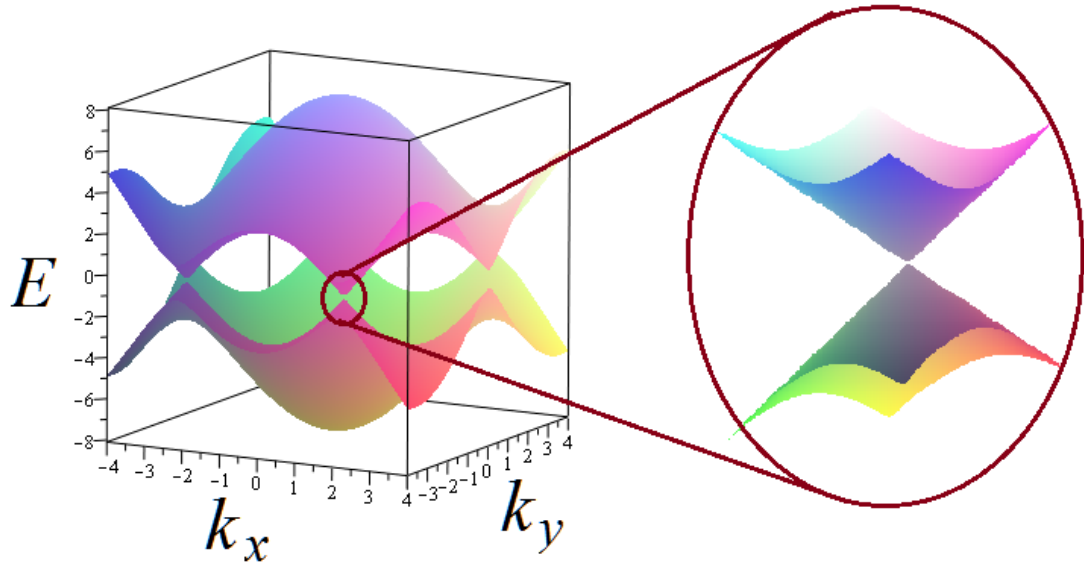


Figure 2.2: Electronic energy dispersion of graphene near one Brillouin zone. The vertical axis is the electron energy (in units of t) with $t = 2.7$ eV, and $t' = -0.2t$. A zoomed in view of the dispersion near one of the K or K' points is shown on the right side.

(2.2). This diagram is commonly referred to as the band structure of graphene. The most striking feature is what's shown in the magnified region of the figure. At low energy, the bands meet at a single (charge neutral) point, which is known as the Dirac point due to similarity of the dispersion with that of particles obeying the relativistic Dirac equation. The energy bands are conical (Dirac cones), which means if you take a slice of the bands through the Dirac point, the slice would produce a linear structure. There are six of these Dirac points at each of the six corners of the BZ, the K and K' points. Due to the complete symmetry of these points, there is a two-fold degeneracy, often referred to as the “valley” degeneracy. This is in addition to the two-fold symmetry due to the spin of the electron (or hole).

2.2.2 Massless Dirac Fermions

As is evident from the electronic energy dispersion graph, the band structure of electrons is mostly dominated by the behavior near the Dirac points of the BZ. The reason being is electrons would have to attain several eV of additional energy to reach the curved part of the dispersion bands. There is an analogy that can be made with electrons in graphene and massless particles that obey the Dirac equation, by approximating the energy dispersion near these Dirac points.

The basic idea of the $\mathbf{k} \cdot \mathbf{p}$ method is to expand the Hamiltonian near the Dirac points, with small momentum terms. Specifically we can write $\mathbf{k} = \mathbf{K} + \mathbf{q}$, or similarly for a K' point, and plug in this expression for momentum into Eq. (2.13). Near the point $\mathbf{K} = 4\pi/3 \sqrt{3}a_0(1, 0)$ it gives the following expression of the off diagonal elements of \mathbf{H} :

$$H_{AB} = -t \exp(i\mathbf{q} \cdot \boldsymbol{\delta}_2) [\exp(2\pi i/3) \exp(i\mathbf{q} \cdot \mathbf{a}_1) + \exp(-2\pi i/3) + \exp(i\mathbf{q} \cdot \mathbf{a}_2)]. \quad (2.19)$$

A simple Taylor expansion on the exponentials inside the brackets to first order gives the simplified expression

$$H_{AB} \simeq -t(1 + i\mathbf{q} \cdot \boldsymbol{\delta}_2) [\exp(2\pi i/3)(1 + i\mathbf{q} \cdot \mathbf{a}_1) + \exp(-2\pi i/3) + (1 + i\mathbf{q} \cdot \mathbf{a}_2)]. \quad (2.20)$$

Multiplying everything out, and keeping only the linear terms gives after some algebra

$$H_{AB} \simeq \frac{3a_0 t}{2} (q_x - iq_y). \quad (2.21)$$

With this final expression for the H_{AB} , we can write out the Hamiltonian matrix for the low-energy electrons [22],

$$\mathbf{H} = \frac{3a_0 t}{2} \begin{pmatrix} 0 & q_x - iq_y \\ q_x + iq_y & 0 \end{pmatrix}. \quad (2.22)$$

The factor in front bears the units of velocity, and is in fact an expression for the Fermi velocity of the electrons in graphene:

$$v_F = \frac{3a_0 t}{2\hbar} \approx \frac{c}{300}, \quad (2.23)$$

where c is the speed of light in a vacuum. This Fermi velocity has been measured by several different means, including photoconductive spectroscopy [23], similar to the measurement discussed in Chapter V of this thesis. By means of the Pauli spin matrices, this Hamiltonian can be written very compactly as

$$\mathbf{H} = \hbar v_F \mathbf{q} \cdot \boldsymbol{\sigma}. \quad (2.24)$$

There is a corresponding expression for the Hamiltonian near the K' point with a replacement of $\boldsymbol{\sigma} = (\sigma_x, \sigma_y)$ with $\boldsymbol{\sigma}^* = (\sigma_x, -\sigma_y)$. It is quite easily seen that the corresponding energy is then

$$E(\mathbf{q}) = \pm \hbar v_F q. \quad (2.25)$$

From this expression for the Hamiltonian of low-energy electrons, several key features of graphene can be gleaned. The first point is that the electron's energy is linearly proportional to its momentum. This is quite extraordinary given electrons in most any other materials have an energy that is parabolic,

$$E(\mathbf{k}) = \frac{\hbar^2 k^2}{2m^*}. \quad (2.26)$$

Another key difference from most materials is that the electron's energy does not depend at all on the mass, meaning that the Fermi velocity doesn't depend on mass either. These facts, and the similarity of this energy dispersion to that of light, have led to the label of electrons in graphene as massless Dirac fermions [24, 25]. Also, due to the conical nature of the band structure meeting at the Dirac points, there is no bandgap in pristine graphene. Thus graphene is usually referred to as a semi-metal (not quite a metal, not quite a semiconductor).

In the low-momentum limit, the wave functions $\psi(\mathbf{r})$ satisfy the Schrödinger equation

$$-i\hbar v_F \boldsymbol{\sigma} \cdot \nabla \psi(\mathbf{r}) = E \psi(\mathbf{r}). \quad (2.27)$$

Near the K point, the eigenenergies are $E_K = \pm \hbar v_F \boldsymbol{\sigma} \cdot \mathbf{q}$, for the π^* and π bands, respectively. The corresponding wavefunctions are given by

$$\psi_{\pm,K}(\mathbf{q}) = \frac{1}{\sqrt{2}} \begin{pmatrix} e^{-i\theta_q/2} \\ \pm e^{i\theta_q/2} \end{pmatrix}, \quad (2.28)$$

where

$$\theta_q = \tan^{-1} \left(\frac{q_x}{q_y} \right). \quad (2.29)$$

At the K' point, where the eigenenergies are $E_{K'} = \pm \hbar v_F \boldsymbol{\sigma}^* \cdot \mathbf{q}$, the corresponding wavefunctions are then

$$\psi_{\pm,K'}(\mathbf{q}) = \frac{1}{\sqrt{2}} \begin{pmatrix} e^{i\theta_q/2} \\ \pm e^{-i\theta_q/2} \end{pmatrix}. \quad (2.30)$$

The wave functions at both the K and K' points closely resemble those of spinors, and in fact this property for graphene is usually referred to as pseudospin (or chirality). This label of pseudospin comes from its mathematical character, in contrast to the physical spin of electrons. Notice that if the phase θ_q is rotated by 2π , i.e., $\theta_q \rightarrow \theta_q + 2\pi$, then the overall sign of the wavefunctions changes.

This is equivalent to a change of phase of π under rotation. This is the so-called Berry's phase of π for graphene.

The pseudospin property of graphene can be understood in terms of the helicity operator

$$h = \frac{1}{2} \boldsymbol{\sigma} \cdot \frac{\mathbf{p}}{|\mathbf{p}|}. \quad (2.31)$$

Comparing this operator to the expression for the Hamiltonian, Eq. (2.24), it is clear that the wavefunctions $\psi(\mathbf{r})$ defined above are also eigenfunctions of h , with eigenvalues $\pm 1/2$. For the K point, electrons have positive helicity and holes have a negative helicity, and vice versa for the K' point. Anything that induces an energy bandgap would invalidate this property, and does not hold for “high-energy” electrons/holes.

This property of pseudospin so closely related to the momentum is a major cause of the unusually high electron mobility in graphene. Long-range disorder such as charged impurities from the substrate have Fourier components $V(\mathbf{q})$ such that $|\mathbf{q}| \ll |\mathbf{K}|$, when we consider a scattering process $\mathbf{k} \rightarrow \mathbf{k}'$. These potentials do not couple to the pseudospin, therefore do not introduce scattering between K and K' points. The resulting matrix element between states is given by

$$|\langle \mathbf{k}' | V(\mathbf{q}) | \mathbf{k} \rangle|^2 = |V(\mathbf{k} - \mathbf{k}')|^2 \cos^2(\theta_{\mathbf{k}, \mathbf{k}'} / 2), \quad (2.32)$$

where $\theta_{\mathbf{k}, \mathbf{k}'}$ is the angle between initial and final states' momenta [26, 27]. From this expression it is clear that backscattering between states with momentum \mathbf{k} and $-\mathbf{k}$ are forbidden ($\theta_{\mathbf{k}, \mathbf{k}'} = \pi$). Short range interactions with $\mathbf{q} \sim \mathbf{K}$ do not have this restriction, and can therefore induce backscattering of electrons. Further, scattering between valleys requires a large change in momentum and generally does not occur.

2.2.3 Bilayer Graphene

Monolayer graphene is really quite a special material in terms of its electronic structure. A sample of two coupled sheets of graphene (bilayer graphene) has a completely different band structure for low energy electrons. The most common crystal order of bilayer graphene is Bernal stacking, which is displayed in Figure 2.3. In this arrangement, the A and B sublattices in the top sheet are shifted so that the carbon atoms in the B' sublattice of the bottom sheet lay below the empty space in the

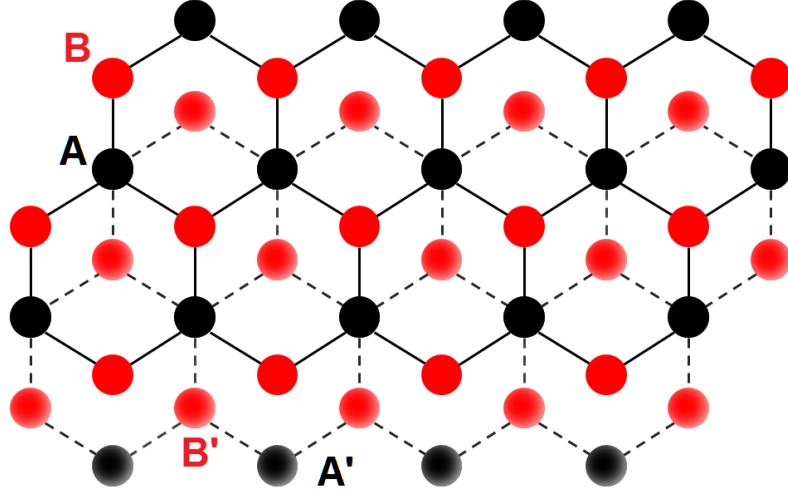


Figure 2.3: Top down view of a small section of bilayer graphene with AB (Bernal) stacking order. Solid lines show C-C bonding between carbon atoms in the top layer, and dashed lines showing C-C bonding between carbon atoms in the bottom layer.

middle of an upper hexagon. The A' sublattice atoms of the bottom sheet are directly below the A sublattice atoms of the top sheet.

The calculation of the band structure for bilayer graphene can also be performed using the tight-binding approximation. Again, for most electron transport in bilayer devices this is a good approximation. In this calculation we consider the following conduction paths with their corresponding energies [28]. The in plane hopping is the same as for monolayer graphene, but given the standard label for graphite $\gamma_0 = t$. The hopping energy between atoms A and A' is $\gamma_1 = t_{\perp} \approx 0.4$ eV. This model also considers hopping between B' atoms and B atoms with energy $\gamma_3 \approx 0.3$ eV, while higher order hopping terms are neglected. Furthermore, we can account for the possibility of a potential bias applied between the layers, by a shift of $2V$ of the chemical potential between the layers. If we define the in plane complex momentum as $q = q_x + iq_y$, then the Hamiltonian close to the K point of the top layer can be written as [22]

$$\mathbf{H} = \begin{pmatrix} -V & \hbar v_F q & 0 & 3\gamma_3 a_0 q^* \\ \hbar v_F q^* & -V & \gamma_1 & 0 \\ 0 & \gamma_1 & V & \hbar v_F q \\ 3\gamma_3 a_0 q & 0 & \hbar v_F q^* & V \end{pmatrix}. \quad (2.33)$$

In the simple case that we neglect $\gamma_3 = 0$, then the eigenenergies can be solved for using the

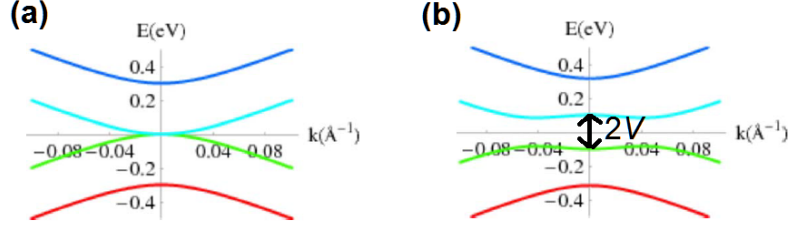


Figure 2.4: (a) Plot of the low energy dispersion of bands in bilayer graphene given by Eq. (2.34), with $V = 0$. (b) Plot of the corresponding energy bands with a non-zero potential $V = 0.1$ eV.

secular equation. There are four hyperbolic bands given by the expression

$$E_{\pm}^2(q) = V^2 + (\hbar v_F q)^2 + \frac{t_{\perp}^2}{2} \pm \sqrt{(2V\hbar v_F q)^2 + (t_{\perp}\hbar v_F q)^2 + \left(\frac{t_{\perp}^2}{2}\right)^2}. \quad (2.34)$$

Including a non-zero γ_3 would introduce trigonal warping of the bands even at the lowest energies (momenta).

A two-dimensional plot of these band is shown in Figure 2.4 for $\gamma_3 = 0$ so that there is full rotational symmetry about the vertical axis. In the case that $V = 0$, one pair of valence and conduction bands meet at zero energy, and exhibit the normal parabolic dispersion for small momentum. In the case where $V \neq 0$, there is a energy gap between the upper valence band and the lower conduction band. As mentioned in the previous Chapter, this is vital for the possibility of building bilayer graphene transistors.

2.3 Electric Field Effect

A final key property of graphene is its field effect. The introduction of an electric field, by applying a potential bias, can dramatically change the conducting properties of the charge carriers in graphene. Not only can the conductivity be tuned, but also the type of the majority charge carrier can be changed.

For pristine graphene in the absence of any kind of external bias, the Fermi level E_F is set at the Dirac point. Using simple statistical mechanics for a two-dimensional electron gas (2DEG) and the linear energy dispersion, the density of states can be written as

$$D(E) = \frac{g_s g_v}{2\pi(\hbar v_F)^2} |E|, \quad (2.35)$$

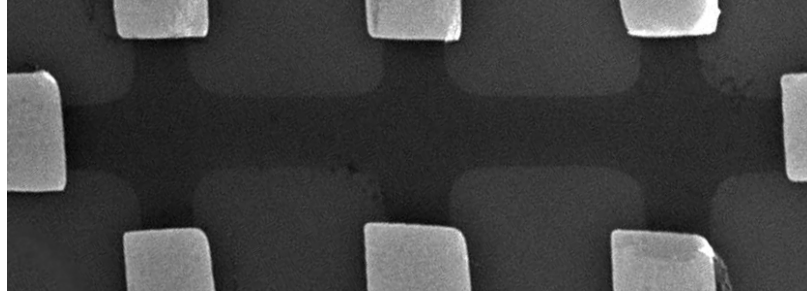


Figure 2.5: Scanning electron micrograph of exfoliated graphene patterned into a hall bar structure. The lighter contrast areas on the edge of the graphene flake are metal contacts. The central graphene channel is 2 μm wide.

where $g_s = 2$ and $g_v = 2$ are the spin and valley degeneracies, and E is relative to the Dirac point. The electron density (n) and hole density (p) can be calculated using the Fermi-Dirac distribution $f(E) = (1 + \exp[(E - E_F)/k_B T])^{-1}$, where k_B is the Boltzmann constant. The densities are evaluated as follows:

$$n = \int_0^{\infty} D(E) f(E) dE = \frac{2}{\pi} \left(\frac{k_B T}{\hbar v_F} \right)^2 F_1 \left(\frac{E_F}{k_B T} \right), \quad (2.36)$$

and

$$p = \int_{-\infty}^0 D(E) (1 - f(E)) dE = \frac{2}{\pi} \left(\frac{k_B T}{\hbar v_F} \right)^2 F_1 \left(\frac{-E_F}{k_B T} \right), \quad (2.37)$$

where $F_1(x)$ is the Fermi-Dirac integral. In thermal equilibrium these expressions are equal and define the intrinsic carrier concentration

$$n_i = n = p = \frac{\pi}{6} \left(\frac{k_B T}{\hbar v_F} \right)^2, \quad (2.38)$$

which at room temperature is $n_i \sim 9 \times 10^{10} \text{ cm}^{-2}$ [29].

This intrinsic carrier density can be tuned higher to a great degree by the application of an electric field. A common set of devices made for graphene measurements are graphene Hall bar structures. Figure 2.5 shows scanning electron micrograph of this type of device that is that adhered to the surface of an oxidized ($t_{\text{SiO}_2} = 300 \text{ nm}$) doped silicon wafer. The device is patterned from a larger flake of exfoliated graphene using standard electron beam lithography and plasma etching processes. Electrical contact to the graphene is made by evaporating Ti/Au (5 nm/30 nm thickness) leads connected to external voltage meters. The external bias is applied to the conducting silicon substrate and is usually referred to as the “gate voltage,” V_g .

The application of a gate voltage introduces a surface charge density in graphene

$$n = \frac{\epsilon_0 \epsilon}{t_{\text{SiO}_2} e} V_g \approx (7.2 \times 10^{10} \text{ cm}^{-2} \text{ V}^{-1}) V_g, \quad (2.39)$$

for $t_{\text{SiO}_2} = 300 \text{ nm}$, where ϵ_0 and ϵ are the permittivities of free space and SiO_2 , respectively, and e is the charge of the electron. At relatively high carrier densities, the measurements of the conductivity σ show linear dependence on the gate voltage, and therefore n , even at room temperature [30]. The carrier mobility μ can be extracted by comparing the slope of the conductivity versus gate voltage curves using the relation:

$$\mu = \frac{\sigma}{ne}. \quad (2.40)$$

Furthermore there is a crossover between majority carriers from holes to electrons as the gate voltage is swept through the Dirac point. Measurements of the Hall resistance of graphene in a magnetic field show a change in sign concurrent with the minimum of conductivity (Dirac point). For voltages below the Dirac point, the positive sign of the R_H indicates majority hole charge carriers, and vice versa, majority electrons for voltages above the Dirac point. This behavior is easily seen in Figure 2.6 as the gate voltage shifting the Fermi level above and below the charge neutral point. High quality dielectric layers can withstand gate voltages $\sim 100 \text{ V}$ before undergoing electrical breakdown and burning out. Other gating mechanisms are used as well involving polymer top gates [31], metal gates with high- κ (HfO_2) dielectric barriers [32], and the like. These gates offer higher possible carrier densities because of the reduced dielectric layer thickness and improved permittivity, but generally can't allow for such a high potential bias as the Si back gate approaches.

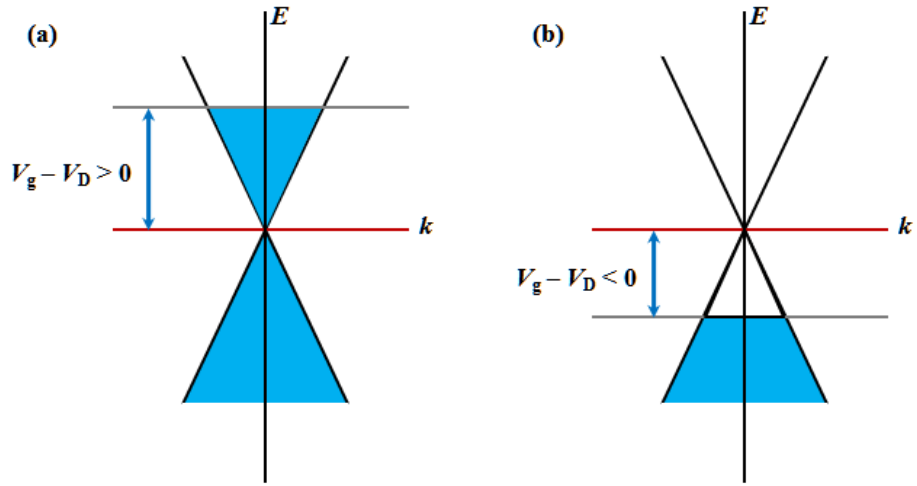


Figure 2.6: Electron energy dispersion Dirac cones near a K point in graphene. As V_g is swept from negative to positive voltages (relative to the conductivity minimum), (a) there are filled electron states above the Dirac point, and (b) empty electron states below the Dirac point.

CHAPTER III

EXPERIMENTAL

Currently there are several methods for obtaining graphene. These include mechanical exfoliation, epitaxial growth on SiC by sublimation, and chemical vapor deposition (CVD) on transition metal surfaces. Mechanical exfoliation was the first technique used by Andrew Geim [24] to obtain graphene flakes of sizes on the order of hundreds of square microns. While this is a low-tech method, and can be performed by a very unskilled person the size of samples and the relative yield are both small which makes this method unsatisfactory for industrial scale applications. The epitaxial growth and CVD growth methods are however scalable to large samples, but require the use of specialized equipment and training. All samples produced by our lab for the work in this thesis use either the exfoliation or CVD methods. These methods will be described in detail in this chapter.

3.1 Mechanical Exfoliation

As described above, graphite consists of stacked layers of graphene, which are only held together by relatively weak Van der Waals intermolecular forces. There are three forms of graphite stacking sequences: A (simple hexagonal), AB (Bernal), and ABC (rhombohedral). Of these, AB stacking is the most common, with only about 10-15% abundance of ABC stacked graphite occurring naturally, and almost no A stacking [5]. These stacking sequences of graphite are illustrated in Figure 3.1. There are several forms of graphite used to exfoliate graphene with highly-ordered pyrolytic graphite (HOPG), and Kish graphite being the two most popular. Since the graphene sheets in graphite are only weakly bonded it is rather easy to peel off (exfoliate) several layers from the bulk.

The process of exfoliating monolayer, bilayer, or thicker few-layer graphene samples exploits this bonding weakness. A piece of tape (originally Scotch Magic tape, from 3M company) is firmly pressed onto the surface of a graphite sample. This usually removes a still relatively thick piece of graphite (100s of graphene layers). This thinner graphite is repeatedly pressed onto fresh areas of the tape until the remaining graphite is quite thin (10s of graphene layers). This thin graphite

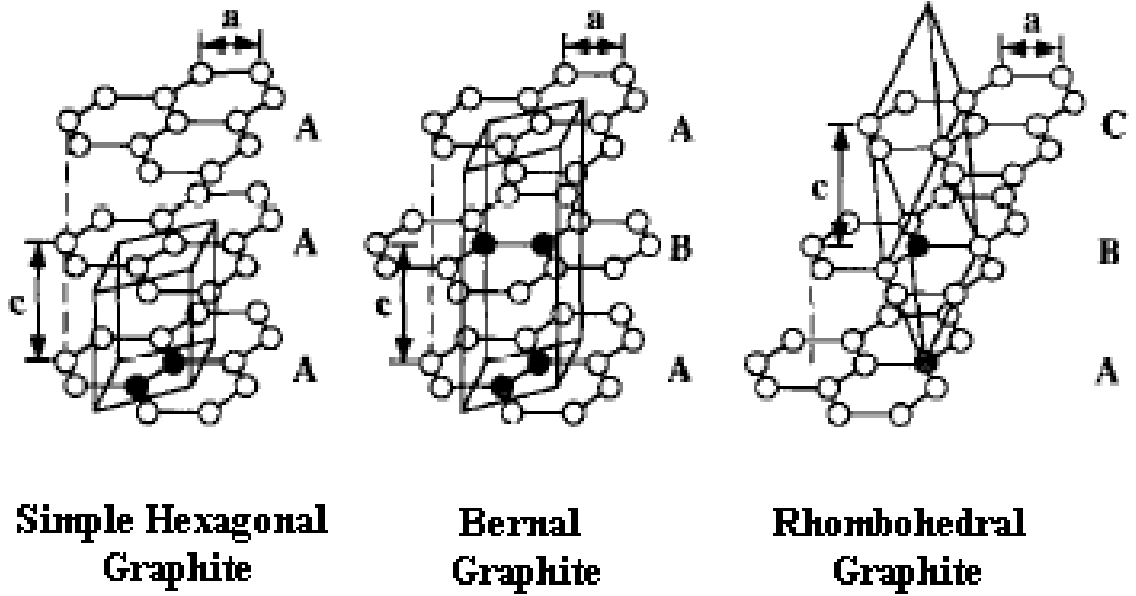


Figure 3.1: Stacking sequences of graphene sheets into three-dimensional graphite. Picture taken from [5].

coated tape is then pressed against the surface of whatever substrate and slowly peeled away. What is left is a random assortment of flakes of monolayer to few-layer graphene of varying sizes and thicknesses. The main issue with this method is locating the desirable flakes. Due to the very high optical transparency for monolayer and bilayer graphene locating and identifying the thickness of flakes is difficult.

There are several means to identify monolayer and thicker graphene samples including atomic force microscopy (AFM), scanning electron microscopy (SEM), Raman spectroscopy, and optical microscopy. The first three methods suffer from the fact that it requires a long time to scan a large area of a sample. Both AFM and Raman can accurately determine the flake thickness, but SEM is difficult to calibrate between contrast and thickness. The optical method allows for quickly scanning wafers of sizes $> 1 \times 1 \text{ cm}^2$ with a simple microscope (preferably with color filters).

The key to this method is the phase shift of reflected light through graphene and the substrate. The most common substrate used for identifying graphene flakes is an oxidized silicon wafer (Si/SiO_2). Figure 3.2 shows a typical graphene flake placed on a silicon wafer with 300 nm of thermally grown oxide. The oxide acts not only to enhance the visibility of the graphene flake, but also serves as insulating layer between the graphene and the silicon gate which can be useful

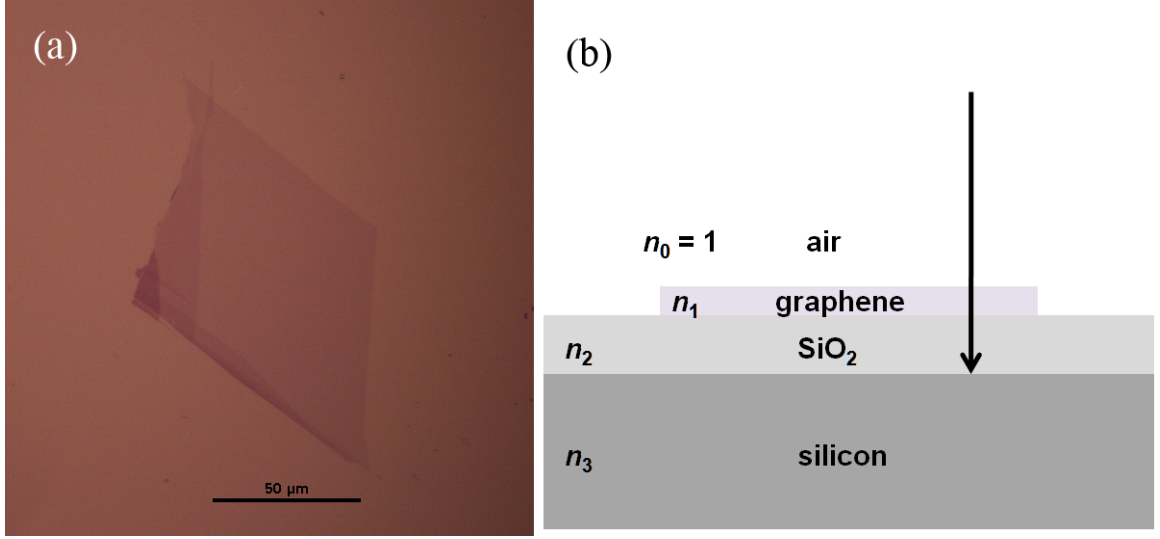


Figure 3.2: (a) Optical microscope image of a mechanically exfoliated flake of graphene on an oxidized silicon wafer. The lightest color contrast area is monolayer graphene, with darker areas corresponding to bilayer and thicker few-layer graphene. (b) Schematic view of the graphene on this typical substrate, showing the normally incident light observed by a microscope.

Table 3.1: Indices of refraction used to model graphene on an oxidized silicon wafer, and layer thicknesses.

Material	Layer index, i	n_i	d_i
air	0	1	semi-infinite
graphene	1	$2.0 - 1.1i$	0.335 nm (monolayer)
SiO ₂	2	1.47	300 nm
silicon	3	$5.6 - 0.4i$	semi-infinite

for making transistor-type devices. As is often the case, this flake has areas of minimal contrast (monolayer graphene) and with higher contrast (bilayer and thicker). The ideal samples are those which are uniform thickness and isolated from other graphene flakes.

This enhanced contrast is described using the reflection coefficient of light from a graphene/substrate multilayer system. This model accounts for normally incident and detected light, which is typically used as in the case of an optical microscope illuminating the top of the sample. We define n_i , with $i = 0, 1, 2, 3$ as the complex index of refraction for air, graphene, SiO₂, and Si, respectively. Also, d_i are the thicknesses of each corresponding layer. The values for n_i and d_i used in this model are given in Table 3.1 (taken from Ref [33]). Light passing through layer i will have a phase shift given

by the expression [34]:

$$\phi_i = 2\pi n_i \frac{d_i}{\lambda}, \quad (3.1)$$

where λ is the wavelength of the light passing through that medium. There is a reflection coefficient for each of the different interfaces (graphene/SiO₂, etc.) given by

$$r_1 = \frac{n_0 - n_1}{n_0 + n_1} \quad (\text{air/graphene}), \quad (3.2)$$

$$r_2 = \frac{n_1 - n_2}{n_1 + n_2} \quad (\text{graphene/SiO}_2), \quad (3.3)$$

and

$$r_3 = \frac{n_2 - n_3}{n_2 + n_3} \quad (\text{SiO}_2/\text{Si}). \quad (3.4)$$

Using Fresnel's equations the total reflected light intensity is given by

$$R(\lambda) = \left| \frac{r_a}{r_b} \right|^2, \quad (3.5)$$

where

$$r_a = r_1 e^{i(\phi_1 + \phi_2)} + r_2 e^{-i(\phi_1 - \phi_2)} + r_3 e^{-i(\phi_1 + \phi_2)} + r_1 r_2 r_3 e^{i(\phi_1 - \phi_2)}, \quad (3.6)$$

and

$$r_b = e^{i(\phi_1 + \phi_2)} + r_1 r_2 e^{-i(\phi_1 - \phi_2)} + r_1 r_3 e^{-i(\phi_1 + \phi_2)} + r_2 r_3 e^{i(\phi_1 - \phi_2)}. \quad (3.7)$$

The contrast between the graphene and the bare substrate is then given by

$$C(\lambda) = \frac{R_0(\lambda) - R(\lambda)}{R_0(\lambda)}, \quad (3.8)$$

where $R_0(\lambda)$ is the reflection coefficient without the contribution from graphene (i.e., $n_1 = 1$ and $d_1 = 0$).

Using this model, the optimal oxide thickness can be chosen for making monolayer graphene have the largest contrast. There are two values for oxide thickness that optimize the contract which are commonly used for graphene substrates (90 nm and 300 nm). Specifically for the 300 nm thick oxide, there is a contrast of about 8% for a wavelength of $\lambda = 550$ nm for monolayer graphene, with the contrast increasing linearly with the number of layers [33].

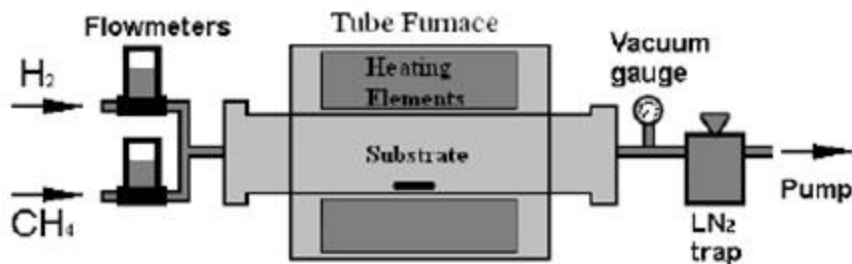


Figure 3.3: Block Diagram of CVD growth system.

3.2 Chemical Vapor Deposition Growth

Of the several methods for obtaining graphene, our group has focused on CVD growth of graphene as a means for obtaining large area samples. This section will describe in detail the process for this growth method, while outlining its key benefits and downfalls.

In general, the process of chemical vapor deposition starts with a substrate material in a reaction chamber. Various gases are introduced to the chamber at varying temperature and pressure, sometimes with the aid of a plasma. The gas molecules inside the reaction chamber are dissociated and reformed at the catalytic surface of the substrate. Growth occurs at various nucleation sites, as well as at the growth front of an ever increasing material layer. This growth process proceeds until the reaction is stopped by several means, including: cessation of gas flow, lowering of temperature, full catalyst surface coverage, or other factors. In fact, the CVD growth of graphene is finished by a combination of these factors.

Our specific growth method for CVD grown graphene has been adapted from previously reported recipes cited in the literature [35, 36]. A block diagram of our lab's CVD system is shown in Figure 3.3. The main reaction chamber is a 50 mm diameter quartz tube that can withstand the high temperatures needed for graphene growth. This quartz tube is placed inside a tube furnace with a programmable digital temperature control up to 1400 °C. The quartz tube is connected to vacuum/gas lines on either side by double O-ring seals from MTI corporation. The inlet of the reaction chamber is connected to parallel mass flow controllers which allow accurate control of the source gasses. The outlet of the reaction chamber is connected to a mechanical oil vane pump with a liquid nitrogen trap to keep impurities out of the pump.

As a starting material, we use 99.8% pure copper foil (25 μm thick) obtained from Alfa Aesar.

This foil comes in a large roll, which must be flattened out into smaller sheets. In principle, the graphene that will be grown is as large as the sheet of copper that is placed into the CVD chamber. But, for ease of processing after the growth, we only use small $1 \times 1 \text{ cm}^2$ squares. Care must be taken so that the delicate foil remains as flat and smooth as possible. Any folds or bends in the foil can affect the gas flow over the sample surface, and the subsequent graphene film quality. Since this foil is exposed to air, there is a small oxide layer on the surface of the copper to begin with. Another group has proposed using an acetic acid dip to remove this oxide layer before placing the sample in the CVD chamber.[37] From our own experiments, we have found that this acid dip doesn't appreciably increase the sample quality. It is possible that this small oxide layer may even be removed during the annealing step of the graphene growth process.

The small copper foil samples are placed on a 1 in. diameter half cylinder quartz "boat," and are placed in the heating center of the tube furnace. The purpose of the boat is to allow for ease of loading and removal of the samples, and also to elevate the samples closer to the center of the quartz tube, where there is a larger gas flow. The quartz tube is then sealed using the double O-ring seal. The entire system is pumped out (to the outlet of the gas flow controllers) by the mechanical pump. The system typically reaches a base pressure of $\sim 100 \text{ mTorr}$, which takes approximately 45 minutes. It is crucial to evacuate the CVD system to this low pressure to eliminate any gas present in the chamber, specifically oxygen, which can severely degrade the quality of the grown graphene films. In fact, several samples grown in the presence of oxygen show peaks in a Raman spectrum which are indicative of graphene oxide. As a note, there are several groups that perform growth under ambient pressure. We made extensive attempts at growth under this condition with various recipes with no success in obtaining monolayer graphene.

After the CVD system is pumped out, a mixture of H_2/Ar (10% H_2) gas is introduced to the reaction chamber. The system is pumped by the mechanical pump throughout the whole growth process. Due to the introduction of the gas to the system, the pressure at the inlet of the reaction chamber rises to $\sim 10 \text{ Torr}$, and is dependent on the actual flow rate of gas introduced. The tube furnace is heated to 1000°C at a rate of $70^\circ\text{C}/\text{min}$. The chamber remains at that temperature, with a constant H_2/Ar flow for 20 minutes. A schematic of this and subsequent growth steps is shown in Figure 3.4.

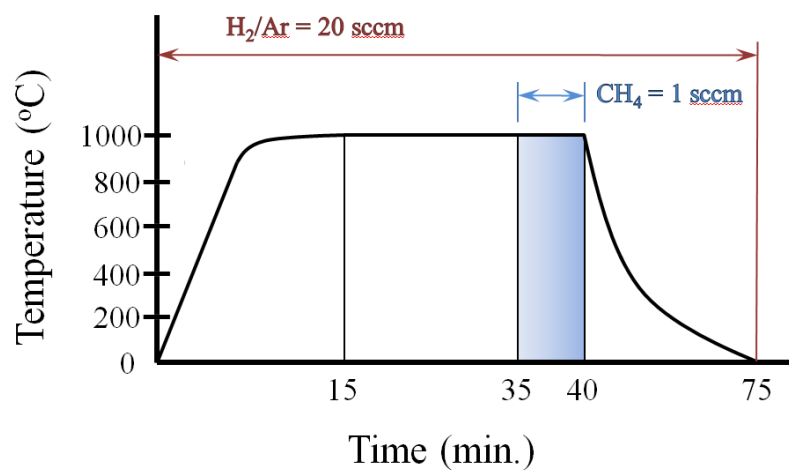


Figure 3.4: Schematic of CVD growth process showing process temperature versus time. The horizontal axis is not to scale.

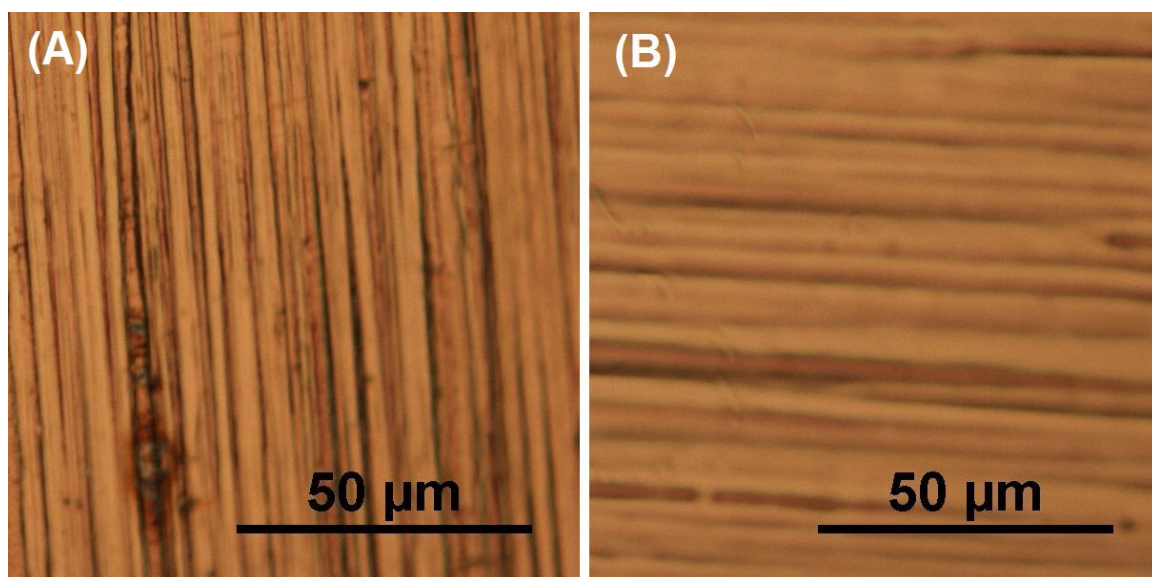


Figure 3.5: Optical images of (a) as delivered copper foil from Alfa Aesar, and (b) copper foil after annealing with high temperature and H_2/Ar flow.

There is no convenient way to measure the actual sample temperature inside the reaction chamber, which means the copper foil is a few degrees cooler than the temperature read by the furnace. Raising the foil temperature anneals the copper by allowing the copper atoms to reflow. This annealing removes some of the crystal defects, allows impurities in the copper to diffuse out of the metal, and increases the size of the copper single crystal grains. The addition of hydrogen gas aids in the removal of impurities and helps clean the surface of the foil. A visual comparison between pre and post-annealed copper samples is shown in Figure 3.5.

After the copper is annealed for 20 minutes, CH_4 gas is introduced. Methane is the source of carbon for the graphene that will grow on the surface of the copper foil. Some groups have also used ethylene [38], solvent based graphene growth [39, 40], or even solid sources of carbon for growth by the CVD method [41]. In this CVD process, it has been argued using molecular dynamics simulations that the partially dehydrogenated CH_x species nucleate on the surface of the copper, and are further dehydrogenated on the surface as other species bond to the original ones [42]. This nucleation of CH_x occurs at various points on the copper foil including step edges, folds, polish lines, and other thermodynamically advantageous features. The original nucleation point becomes an attractor of other carbon species and forms the growth front of a single crystal domain of graphene. Further C-H bond breaking occurs, leaving a lattice containing only sp^2 bonded carbon atoms remaining on the copper surface. Numerous nucleation sites are present on the copper foil, so the size of individual domains is limited by the free space between growth fronts of individual graphene crystals.

Depending on process parameters, a complete coverage of the copper foil with graphene can occur in the span of tens of seconds to a few minutes. In the ideal situation, the growth of graphene is limited by the availability of the area of the copper foil surface. In this case, the continued introduction of methane will not have any affect on the growth of additional graphene on top of the original monolayer. As illustrated later in this Chapter, this is not always the case. In light of this fact, the flow of methane is cut off after a full coverage of the copper foil with graphene is obtained. This time required for full coverage is determined empirically for a particular set of growth parameters. We have commonly used two sets of parameters to obtain full coverage of monolayer graphene. The first recipe uses 100 sccm H_2/Ar , 20 sccm CH_4 , with a growth time of 5

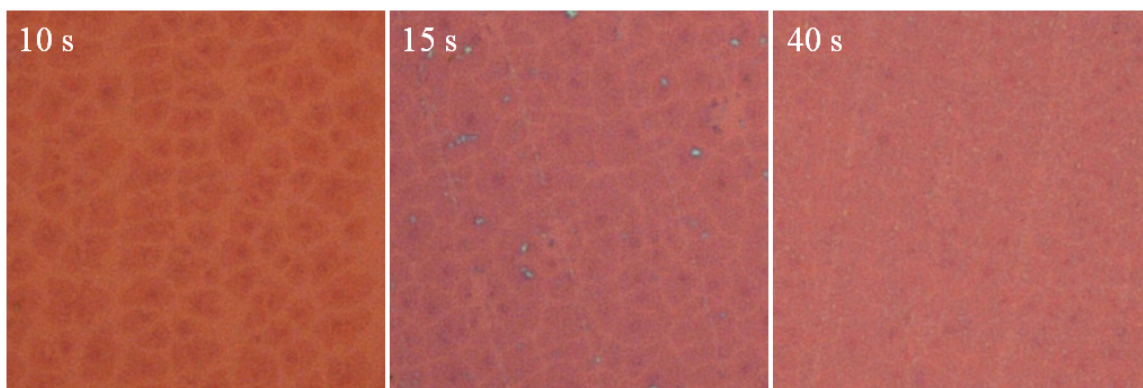


Figure 3.6: Optical images of graphene grown by the CVD process for short amounts of time.

minutes. The other recipe uses much lower flow rates of 20 sccm H_2/Ar , 1 sccm CH_4 , with a growth time of 2.5 minutes.

After graphene formation, the furnace is set to cool back to room temperature as rapidly as possible, and the samples cool naturally. While cooling the sample, the H_2/Ar gas remains flowing to prevent oxidation, and for faster cooling. The graphene coated copper foils are removed when the temperature reaches $\sim 200^\circ\text{C}$. In principle, the samples can be removed at any temperature without oxidizing the copper or graphene. It has been shown that graphene is an effective barrier to oxide formation [43].

For some studies, we were interested in obtaining graphene that did not cover the entire copper substrate. In fact, by adjusting the growth time, we were able to obtain graphene grains with different sizes. Figure 3.6 shows a set of graphene samples synthesized in this manner. Each microscope image in the figure shows graphene grown under the same set of process parameters but with varying amounts of time for the introduction of methane. These samples have been transferred onto oxidized silicon wafers, as will be discussed in the next section. The gas flow rates used for these growths were 20 sccm of H_2/Ar , and 0.5 sccm CH_4 . Apparently, even for the shortest time of 10 s there are several domains that have started to merge together. Also, some of the graphene crystals show the growth of a second layer near the center. This is evident by the darker optical contrast, and has been further verified by Raman spectroscopy. Clearly, increasing the amount of time that methane is introduced to the growth chamber creates further merging of individual crystal domains

and eventually full coverage. In principal, growth of isolated single graphene crystals could be performed with this method. Having precise control on the time is crucial, but is difficult for our setup. Other groups have obtained these types of samples, but with different recipes [44, 45].

3.2.1 Transfer of CVD grown graphene

Graphene samples grown by the above CVD process are generally of high quality, but suffer from the fact that the copper substrate is conductive. Most all samples required for our experiments, or several kinds of electronic devices require that the graphene is on an insulating substrate. This section describes the chemical method for transferring graphene as grown on copper to any desired substrate.

Graphene grown on copper foils is very well adhered to the copper surface. Furthermore, graphene generally coats both surfaces of the foil. An ideal situation would be to simply peel the graphene off of the copper and place it onto another substrate. Electrostatic deposition can be performed for this purpose [46], but suffers from the same limitations as from the mechanical exfoliation method. A better method is to etch away the copper surface, leaving graphene suspended in liquid. This does have the disadvantage of exposing graphene to various chemicals that can dope or chemically charge the samples. The overall process flow is illustrated in Figure 3.7.

Freshly grown graphene on copper foil is spin coated with 950 MW PMMA at 4000 rpm for 40 seconds. This polymer coating is only applied to one side, which is the final graphene sheet that will be transferred. This polymer is usually hard baked after spin coating to drive off excess solvent, but this leaves the polymer hardened. For the sake of keeping the polymer coated graphene flexible, the sample is not baked. The importance of this will be mentioned later. This still leaves the opposite side with freely exposed graphene to be removed. This is accomplished by isotropic reactive ion etching (RIE) with oxygen plasma. Specifically, the sample is loaded into the RIE chamber of a Samco RIE 1-C system, with the exposed graphene side facing up. The chamber is evacuated to low pressure, and then oxygen gas is introduced at a flow rate 4 sccm. Applying 16 W of RF power ignites a plasma in the chamber and is allowed to react for 30 seconds. This is enough time to remove up to a few layers of graphene, but not completely etch the protective polymer coating on the desired, remaining graphene. The remaining foil is now only coated on one side by graphene,

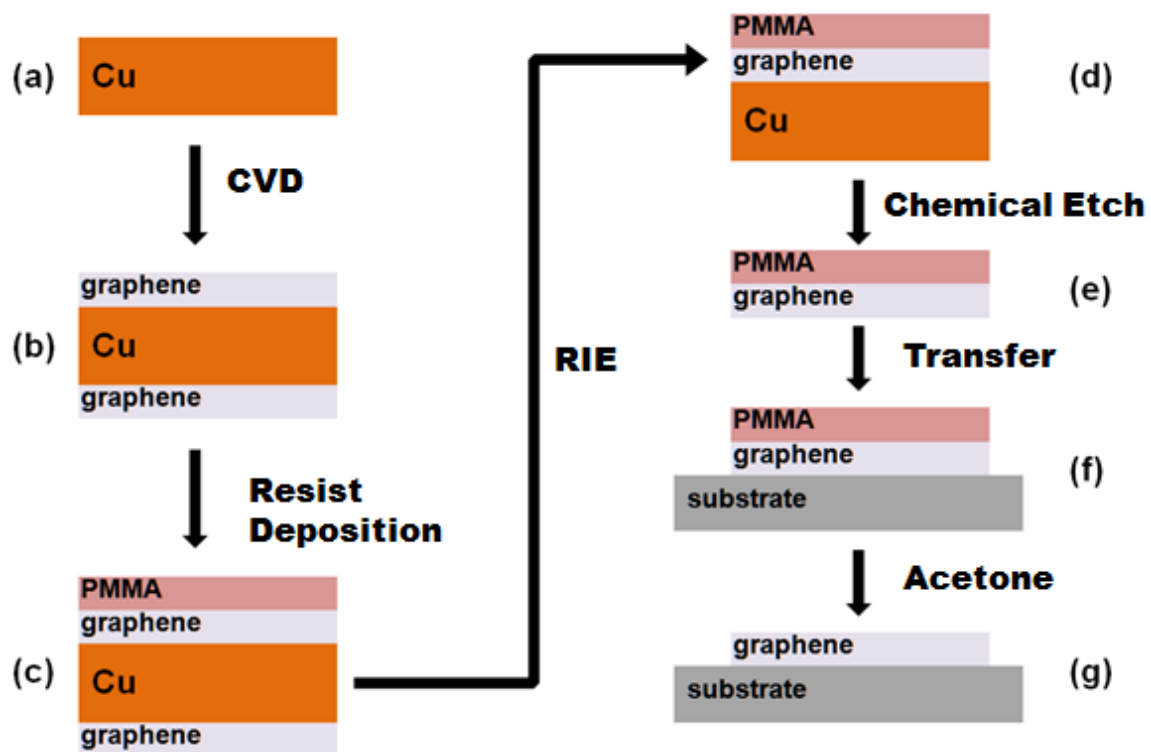


Figure 3.7: Schematic showing the growth and transfer process of CVD grown graphene. (a) The CVD graphene growth process starts with a 99.8% pure copper foil (25 μm thick). (b) Graphene is grown on both surfaces by the CVD method described above. (c) A layer of polymer (950 MW PMMA) is spin coated onto one of the graphene cover surfaces. (d) A reactive ion etch using oxygen plasma removes the non-polymer coated graphene. (e) The copper is chemically etched away using $\text{Fe}(\text{NO})_3$, leaving the polymer coated graphene floating in solution. (f) The graphene is fished out onto the desired substrate. (g) Final removal of the PMMA in acetone leaves the CVD graphene alone on the substrate.

still protected by the PMMA.

The graphene coated copper foil is placed in an aqueous bath of copper etchant. We typically use $\text{Fe}(\text{NO})_3$, with a concentration of 0.05 g/mL by weight. This concentration allows for etching of the copper in a reasonable amount of time, but is dilute enough to easily washed away later. The foil is carefully placed on the surface of the etchant bath, and floats due to surface tension. The samples are usually left to etch over night. After the copper is fully etched away, the graphene/PMMA is left floating in the etchant. Owing to the protective PMMA layer, it is visible to the naked eye. The graphene/PMMA is then lifting by a piece of silicon wafer from underneath and transfer to a bath of deionized (DI) water. By submerging the piece of wafer, the graphene/PMMA is left floating on the surface of the water, and left to sit for about 30 minutes. This process washes off residual copper etchant, and is repeated several times to fully clean the sample.

The cleaned graphene is then fished out onto the desired final substrate (glass, SiO_2/Si , etc.) and then placed onto a hot plate ($T = 65^\circ\text{C}$) to drive out the water. The heating is crucial to promote surface adhesion between the carbon atoms in graphene and the substrate. The polymer coated graphene still mostly conforms to the polymer instead of the flat substrate. To relax the graphene onto the substrate surface, a small amount of liquid PMMA is drop coated onto the graphene. This redissolves the dried protective coating of PMMA already present, further improving the graphene adhesion to the substrate. We noticed that for samples we performed a bake after spin coating, the graphene would poorly adhere to the substrate. By avoiding the baking step, the PMMA remains flexible, but is sturdy enough to survive the remaining process steps. As a final step, all of the PMMA is dissolved in acetone. The remaining graphene is cleaned in IPA/DI water baths.

An optical micrograph of a typical sample of CVD graphene is shown in Figure 3.8. Graphene is covering the entire area except for a few small spots which look lighter in color than most of the image. These are small holes in the graphene film from an imperfect transfer (one small hole in the upper middle portion, and several tiny holes in the bottom right corner). Another feature are the apparent darker lines, which are wrinkles in the otherwise flat graphene sheet. The wrinkles have been observed by other groups for graphene as grown on copper [47], but could also be formed during the transfer process as well.

The last notable item is the greenish colored spots which cover parts of the graphene. These

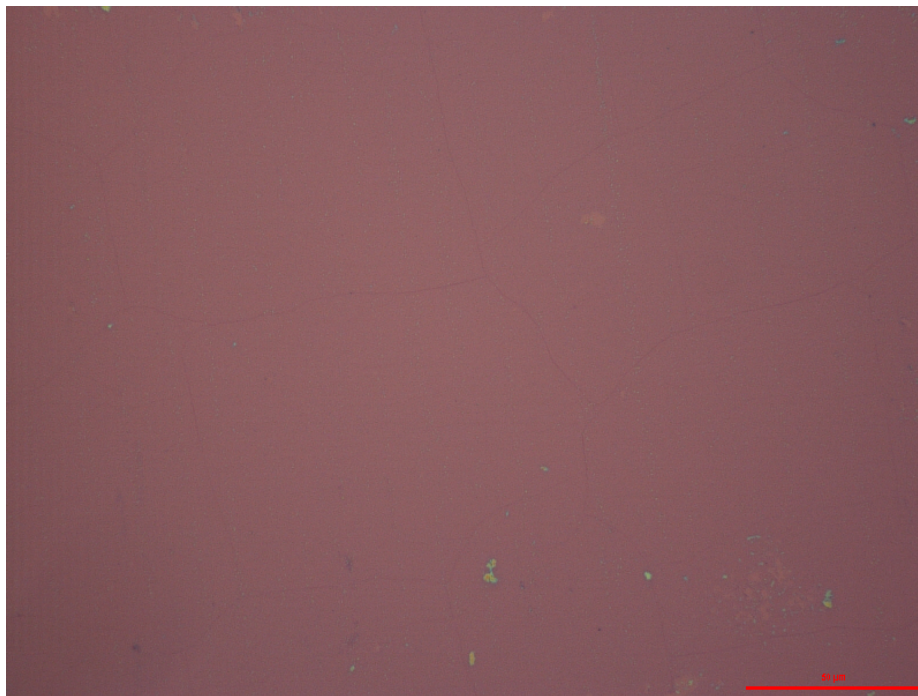


Figure 3.8: Optical micrograph of CVD grown graphene transferred onto oxidized silicon wafer. Scale bar is 50 μm .

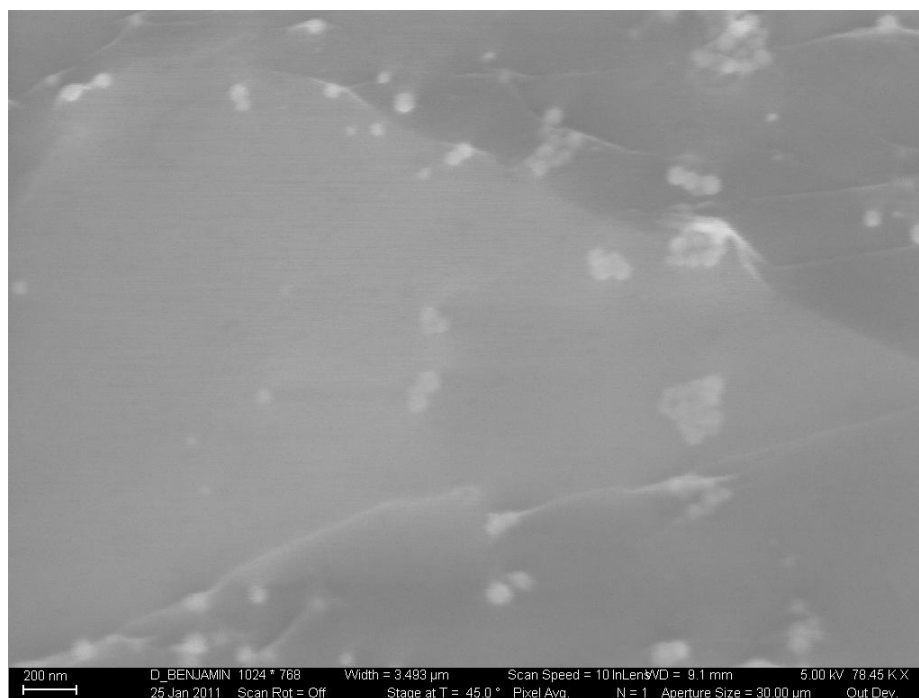


Figure 3.9: Scanning electron micrograph of graphene coated with SiO_2 nanoparticles. Scale bar is 200 nm.

spots are SiO₂ which have been etched from the quartz tube and redeposited on the graphene surface. They range in size from 10's of nm to a few microns, and are on either side of the graphene film. A SEM image of the particles is shown in Figure 3.9, which was taken with the sample tilted 45°. The image shows a region of torn graphene, with SiO₂ particles on both the top and underneath the graphene. The particles under graphene are evident by the wrinkles in the graphene draped over the top. Similar SiO₂ particles are observed in the reported work by other groups [35, 40]. As yet, there is no known method for eliminating the deposition of, or for removing these particles. The H₂ gas used in the growth process also etches the quartz tube, and this process is dependent on temperature. Graphene growth performed at temperatures below 800 °C does not suffer from this issue, but is too cold for actual graphene formation.

3.3 Raman Spectroscopy

As discussed in Section 3.1 monolayer and thicker graphene sheets can be identified using the phase shift of light reflected from certain substrates. For the standard oxidized silicon wafer this provides a quick identification of graphene flakes. Drawbacks of this method are: it relies on a contrast with the surrounding substrate, the color contrast can vary between microscopes and ambient light conditions, and it usually requires comparison with a graphene flake of known number of layers. For large area CVD graphene there often isn't a convenient spot of bare substrate to compare with. A method that can unequivocally measure the film thickness is required for assuring the sample character matches that required for a device or measurement. Raman spectroscopy offers the best method for this accuracy, which is not destructive to the samples.

The basis for this method is laser light (frequency ω_L) incident on a graphene sample interacts with the material, creating or annihilating a quantum excitation (frequency ω) and scattering light (frequency ω_s) away from the sample. When the quantum excitation is an optical phonon, this is referred to as the Raman effect after the physicist who discovered the effect in 1928. The frequency of the quantum excitation is dependent on the material, and by energy conservation must be given by $\omega = \omega_L - \omega_s$ (> 0 for Stokes scattering, < 0 for anti-Stokes scattering), and is usually referred to as the Raman shift. Besides energy conservation, momentum conservation requires that the quantum excitation has nearly zero momentum. This means for first-order Raman scattering the only mode

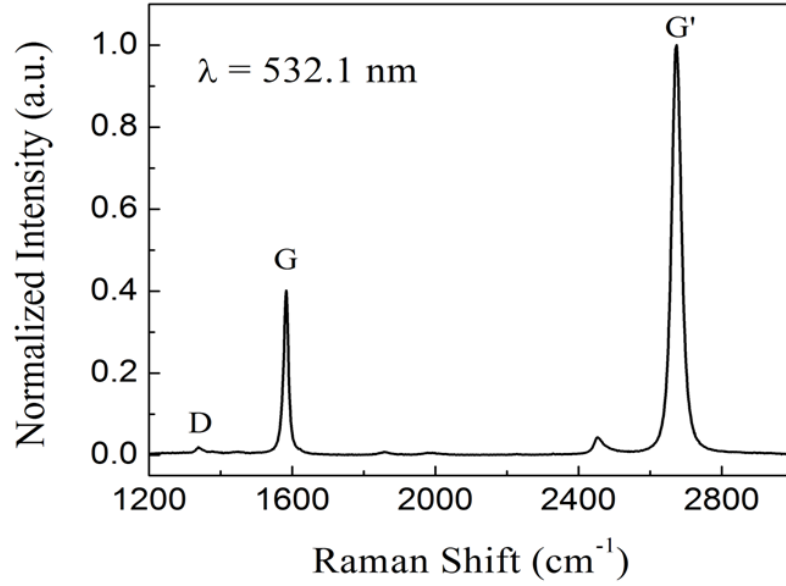


Figure 3.10: A typical Raman spectrum on CVD grown monolayer, taken from a single point on the sample.

allowed is for zone-center optical phonons ($k \approx \Gamma$). Second-order Raman processes involving two phonons (of opposite momentum) are allowed and are particularly strong in monolayer graphene [7].

A Raman spectrum measures the intensity of the scattered light versus the Raman shift over a certain range of frequencies. A typical spectrum taken on a single point of a CVD graphene sample (monolayer) is shown in Figure 3.10, which exhibits all the important features for identification of graphene thickness and quality. Three peaks are labeled on this figure, and are also referred to as bands due to the range of frequencies the peaks span: the *D* band (1337 cm^{-1}), *G* band (1583 cm^{-1}), and the *G'* band (2674 cm^{-1}). The locations of these peaks depend in general on the excitation energy, but for our measurements this is fixed. What is of key importance is the relative intensity of these three peaks, and also the line shape of the *G'* peak.

The physical origin of the three critical peaks in a Raman spectrum of graphene can be explained in terms of its band structure. Figure 3.11 (a) shows the processes that give rise to the above mentioned Raman bands [6]. The *G* band results from a first-order Raman process which satisfies the zero momentum shift condition. The incident laser light interacts indirectly with the doubly degenerate transverse optical (TO) and longitudinal optical (LO) phonon modes at the BZ center (Γ

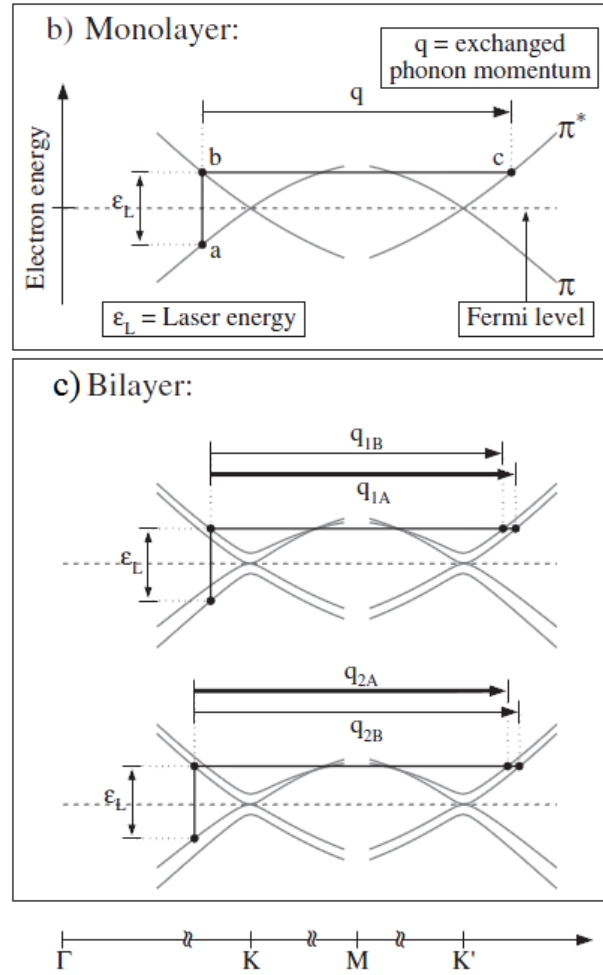
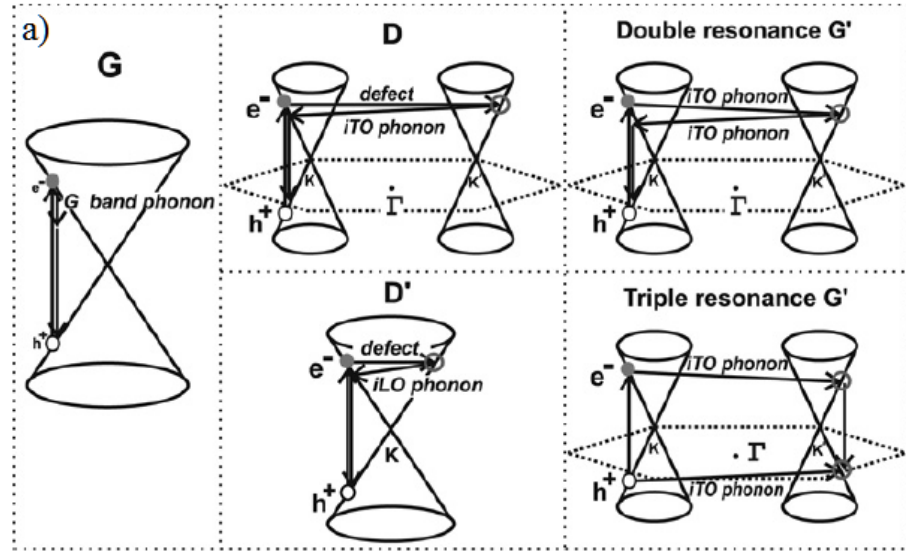


Figure 3.11: (a) Raman processes in monlayer graphene (taken from [6]). Raman double-resonant processes for the G' peak in (b) monlayer graphene, and (c) bilayer graphene (taken from [7]).

point). The incident laser light excites an electron from the valence band to the conduction band. The excited electron emits a BZ center phonon through the electron-phonon interaction, losing a small amount of energy. The electron then recombines with the hole, emitting the scattered photon at the shifted frequency.

The D band and G' band arise from two types of second-order double resonance processes. In each process, the incident photon creates a virtual electron-hole pair by exciting an electron to the conduction band. For the G' band process, the electron and hole both interact with a BZ boundary phonon with large momentum (either \mathbf{K} or \mathbf{K}'), and are scattered to an adjacent valley. In the case of the D band process, the electron/hole is scattered to the adjacent valley by a crystal defect (which is the basis for the label). In both processes, the electron and hole recombine in the other valley, and emit the scattered photon at the shifted frequency. Figure 3.11 (a) shows two other Raman processes as well, but are beyond the scope of this discussion.

The distinction between monolayer and thicker graphene samples comes from the band structure and the G' Raman mechanism. Figure 3.11 (b) and (c) show the corresponding double resonant processes for monolayer and bilayer (AB stacking) graphene, respectively. The process described for monolayer graphene also occurs in bilayer graphene, but with the possibility of four scattering paths. Due to the four electronic bands in bilayer graphene there are four possible laser excited transitions between either pair of valence and conduction bands for a given laser frequency. Two of these optical inter-band transitions are forbidden. Further, there are two possible phonon scattering events to an adjacent valley of slightly differing momentum transfer. Owing to these facts, there is a difference in the line shape of monolayer versus bilayer graphene. The G' peak for monolayer samples generally fits to a single Lorentzian line shape, while for bilayer it takes four Lorentzian peaks to fit the entire G' band. The resulting Raman spectra around the G' peak are shown in Figure 3.12. The G' peak for the monolayer (CVD grown) sample shows the Lorentzian (red) curve fit centered at 2673 cm^{-1} , with a width of 33 cm^{-1} . For the bilayer sample (exfoliated graphene), the G' peaks shows the overall curve fitting (red) of four individual Lorentzian peaks (green), each of varying intensity. These individual peaks are centered at: 2630 cm^{-1} , 2665 cm^{-1} , 2684 cm^{-1} , and 2701 cm^{-1} . The peaks' respective widths are: 23 cm^{-1} , 28 cm^{-1} , 27 cm^{-1} , and 21 cm^{-1} . Clearly the difference in line shape of the G' peak can be used to differentiate between monolayer and bilayer

(AB stacking) graphene.

The situation is a little different for CVD grown bilayer graphene. Figure 3.12 (c) shows the G' peak for such a sample. In this case, the peak is well fit by a single Lorentzian centered at 2680 cm^{-1} , with a width of 43 cm^{-1} . This peak is slightly shifted higher in frequency, and broadened compared with the CVD grown monolayer Raman spectrum. This type of single Lorentzian fit for CVD grown bilayer samples has previously been observed [48]. This indicates that the layers are decoupled, and do not show the same characteristics as the AB stacking bilayer samples. This decoupling has also been observed in epitaxial graphene grown on SiC [49]. In fact rotational disorder between layers can produce similar band structure in bilayer samples as in a monolayer sheet of graphene. This means for CVD grown graphene samples, another method must be used for determining layer thickness from Raman spectra.

The optical matrix elements for the bilayer (for both exfoliated and CVD graphene) transitions are smaller than those for the monolayer transition, which gives rise to a lower G' peak intensity [50]. The relative intensity is measured empirically as a ratio with the intensity of the G peak. For monolayer graphene $I_{G'}/I_G \gtrsim 2$, while for bilayer graphene $I_{G'}/I_G \sim 1$. For trilayer and thicker samples, there are nine and then more possible scattering mechanisms for the G' band, which induces even more peak broadening and a further decrease in the relative intensity of the G' peak. This effect is often used for identifying the layer thickness of graphene samples. This method allows one to quickly determine thickness without the need for complex line shape analysis.

The Raman spectroscopy measurements presented in this thesis were performed on a Horiba LabRAM-HR 800 system. The light source is a He:Ne laser with a wavelength of $\lambda = 532.1\text{ nm}$. The confocal system allows for accurate single spot measurements with a spot size $\sim 1\text{ }\mu\text{m}$ at the highest magnification. A mechanically controlled stage allows for two-dimensional mapping of point-spectra over large areas of a sample ($> 20 \times 20\text{ }\mu\text{m}^2$). This mapping ability is quite useful for determining the uniformity of samples. Figure 3.13 shows the intensity map of the D peak as an example. For this sample, a set of three crystal grains has merged together forming a chain. The intensity of the D peak shown gives a qualitative measure of the amount of crystal disorder from the perfect honeycomb lattice. The hexagonal outline of each grain is clearly evident, as well as strong intensity regions in the middle of the grains (the nucleation center). This same sample will

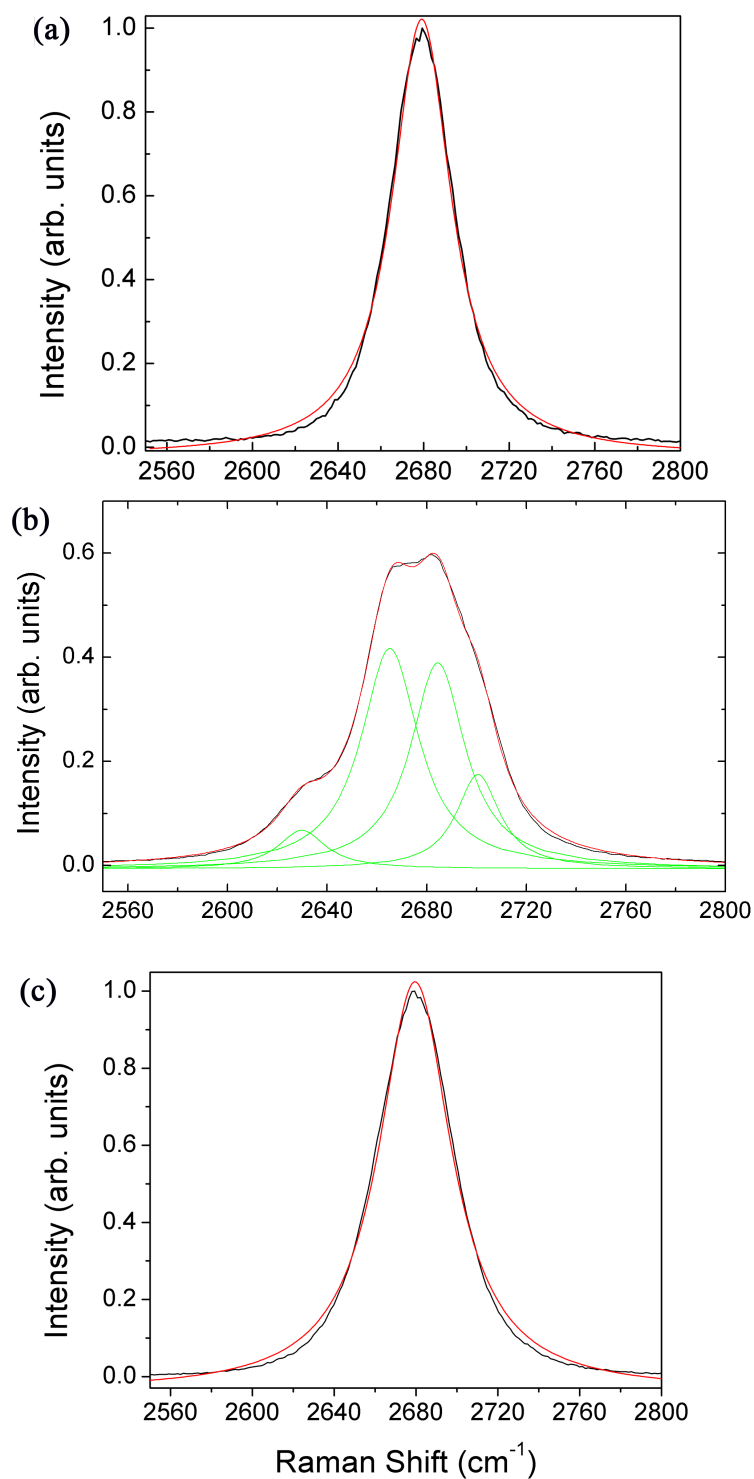


Figure 3.12: G' peak in the Raman spectra of (a) monolayer CVD grown graphene, (b) bilayer exfoliated graphene, and (c) bilayer CVD grown graphene. The red curves are fits to a single Lorentzian peak (monolayer), and four Lorentzian peaks (bilayer). The green curves in (b) are the individual Lorentzian peaks used for the overall curve fit.

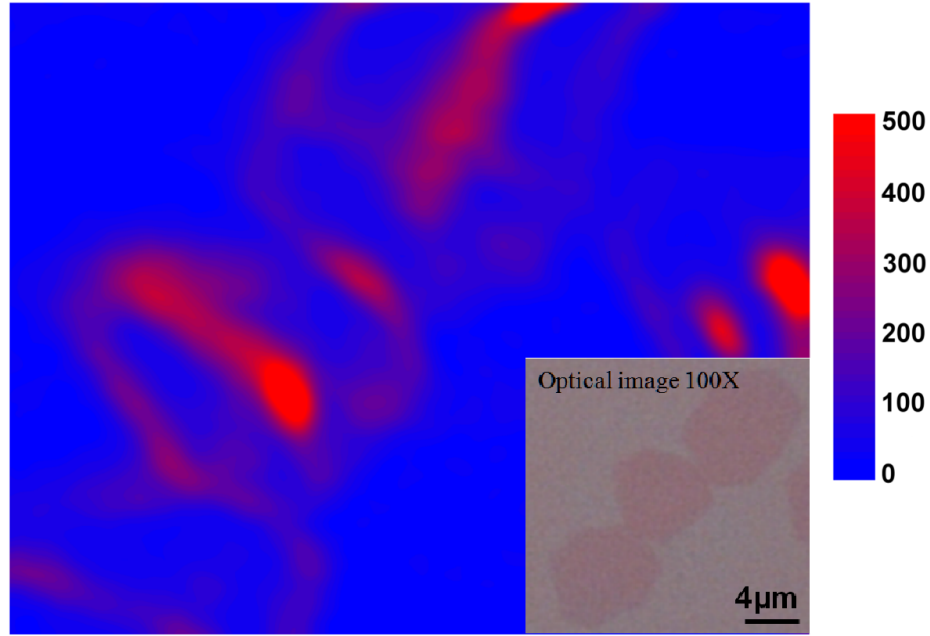


Figure 3.13: Two-dimensional mapping of the intensity of the D peak for a chain of three graphene crystal grains. *Inset:* Optical image of the area shown in the Raman mapping.

be re-examined in Chapter 5.

The measurement of a single Raman spectrum takes about 10 s, and is suitable for quickly identifying the structure of small or large/uniform samples. Performing high resolution Raman mappings is quite time consuming. The above mapping has a spacing of $0.33\ \mu\text{m}$ between scans, and took overnight to fully collect all the spectra. There are several other uses for Raman spectroscopy of graphene that haven't been discussed. Graphene derivatives, such as graphene oxide, have similar but distinct features in their spectra, which makes this technique quite a valuable tool for material characterization [51, 52].

CHAPTER IV

THERMOELECTRIC POWER OF GRAPHENE

Thermoelectric power (TEP) refers to the Seebeck effect discovered by physicist Thomas Seebeck in 1821. When two differing materials, (two metals, oppositely doped semiconductors, etc.) experience a temperature gradient, a potential difference develops across their junction. This effect also extends to a single piece of material. TEP is of great interest for harvesting/converting heat to electricity, leading to green energy solutions beyond fossil fuels.

Due to its extraordinary surface to volume ratio, graphene is highly sensitive to its environment. The thermal and electronic properties depend greatly on not only the supporting substrate of graphene but also on the chemicals that are adsorbed on its surface. Several groups have previously reported on TEP measurements of exfoliated [53, 54, 55], and epitaxial graphene [56]. This Chapter presents the study of the TEP of CVD grown graphene in various environments, with a focus on applications using graphene as a chemical/bio sensor.

4.1 Theoretical Background

The Seebeck coefficient S relates the induced voltage ΔV to the thermal gradient applied, and in simple terms it can be expressed as

$$S = -\frac{\Delta V}{\Delta T}, \quad (4.1)$$

when the temperature difference ΔT is small between the two ends (in a linear response regime). This is a material dependent property and can depend, among other things, on the temperature of a sample and the chemical potential. A key point to note is that the thermal voltage depends on the direction of heating.

The basic physical mechanism of TEP is the diffusion of charge carriers through a material. By placing a thermal gradient, electrons diffuse from the hot region to the colder region. A voltage develops from the separation of excess electrons at the cold end and the remaining positively charged ions at the hot end. There is a corresponding process for the holes as well. In normal metals the

diffusion of electrons and holes is roughly equal due to half filled bands, which gives only a small Seebeck coefficient $\sim \mu\text{V/K}$. If there is a majority of one type of carrier, the thermoelectric voltage developed by those carriers dominates the Seebeck coefficient, and determines the sign. For p-type materials $S > 0$, and for n-type materials $S < 0$, but this can of course be tuned by changing the Fermi level, as will be shown later.

4.1.1 The Mott Formula for $S(T)$

An expression for the temperature dependent Seebeck coefficient $S(T)$ was derived by Mott in 1968 [57] which predicts a linear temperature dependence at temperatures well below the Fermi temperature T_F . In the linear response approximation [58], the electric current density \mathbf{j} , and the thermal current density \mathbf{j}^{th} depend on the applied electric field \mathbf{E} and the thermal gradient ∇T as follows:

$$\mathbf{j} = L^{11}\mathbf{E} + L^{12}(-\nabla T), \quad (4.2)$$

and

$$\mathbf{j}^{\text{th}} = L^{21}\mathbf{E} + L^{22}(-\nabla T). \quad (4.3)$$

The coefficients L^{ij} are defined in terms of the integral expression

$$\begin{aligned} I^{(\alpha)} &= e^2 g \sum_{\mathbf{k}} \tau(\epsilon_{\mathbf{k}}) \mathbf{v}_{\mathbf{k}} \mathbf{v}_{\mathbf{k}} [\epsilon_{\mathbf{k}} - \mu]^\alpha \left(-\frac{\partial f_{\mathbf{k}}^0}{\partial \epsilon_{\mathbf{k}}} \right) \\ &= \int (\epsilon - \mu)^\alpha \left(-\frac{\partial f^0(\epsilon)}{\partial \epsilon} \right) \sigma(\epsilon) d\epsilon. \end{aligned} \quad (4.4)$$

In this expression $\epsilon_{\mathbf{k}} = \hbar v_F |\mathbf{k}|$ for low energy electrons in graphene, $f_{\mathbf{k}}^0$ is the equilibrium Fermi-Dirac distribution function, τ is the relaxation time, μ is the chemical potential, and $g = 4$ is the total degeneracy. The term $\sigma(\epsilon)$ is defined from this expression, and can also be expressed as

$$\sigma(\epsilon) = e^2 v_F^2 D(\epsilon) \frac{\tau(\epsilon)}{2}, \quad (4.5)$$

where $D(\epsilon)$ has been defined in Eq. (2.35). With these definitions, the coefficients L^{ij} can be defined as

$$L^{11} = I^{(0)}, \quad (4.6)$$

$$L^{12} = -\frac{1}{eT} I^{(1)}, \quad (4.7)$$

$$L^{21} = -\frac{1}{e} I^{(1)}, \quad (4.8)$$

and

$$L^{22} = \frac{1}{e^2 T} I^{(2)}. \quad (4.9)$$

Comparing with Eqs. (4.2) and (4.3), the thermoelectric power is defined as

$$S = \frac{L^{12}}{L^{11}}. \quad (4.10)$$

In the low temperature limit ($T \ll T_F$), the integrals $I^{(\alpha)}$ can be approximated by taking the first temperature correction in the Sommerfield expansion. So, to order $(k_B T / \varepsilon_F)^2$, the linear response coefficients are

$$L^{11} = \sigma(\varepsilon_F), \quad (4.11)$$

and

$$L^{21} = T L^{12} = -\frac{\pi^2}{3e} (k_B T)^2 \left(\frac{\partial \sigma(\varepsilon)}{\partial \varepsilon} \right)_{\varepsilon=E_F}. \quad (4.12)$$

This then gives the simplified expression

$$S = -\frac{\pi^2}{3e} \frac{k_B^2 T}{\sigma(E_F)} \left(\frac{\partial \sigma(\varepsilon)}{\partial \varepsilon} \right)_{\varepsilon=E_F}, \quad (4.13)$$

which is the Mott expression for the Seebeck coefficient of a metal.

4.1.2 Deviations From the Mott Formula

The linear temperature dependence of S is accurate for systems with unscreened Coulomb impurities. These impurities are thought to be the main scattering mechanism in clean graphene samples. Indeed with this scattering mechanism, we can take the energy dependent scattering time of the form $\tau = \varepsilon^m$, where m has weak temperature and density dependence [59]. With this expression for scattering time, the Seebeck coefficient reduces to

$$S = -\frac{\pi^2}{3e} \frac{k_B T}{T_F} (m + 1). \quad (4.14)$$

Taking into account charge screening will alter the energy dependent scattering time. For a screened charge q , the Fourier transformed Coulomb potential is

$$v_i(q) = 2\pi e^2 \frac{e^{-qd}}{\epsilon_r q}, \quad (4.15)$$

where $\epsilon_r \approx 2.3$ is the effective dielectric constant of graphene on a SiO_2 substrate, and d is the average distance of the charge impurities from the graphene layer (approximately the thickness of graphene for monolayer samples) [60]. This leads to a scattering time

$$\frac{1}{\tau(\epsilon_k)} = \frac{\pi n_i}{\hbar} \int \left| \frac{v_i(q)}{\epsilon(q, T)} \right|^2 \delta(\epsilon_k - \epsilon_{k'}) (1 - \cos \theta)^2 \frac{d^2 k'}{(2\pi)^2}, \quad (4.16)$$

where θ is the scattering angle, and $\epsilon(q, T)$ is the finite temperature static random phase approximation dielectric function for graphene [60]. With this expression for scattering time, the conductivity and therefore the Seebeck coefficient can be deduced. Within this framework, both quantities depend quadratically with temperature, and holds for neutral scatterers as well [59].

4.2 Experimental Setup

For our measurements of the TEP of graphene we used large area CVD grown samples. The samples used were obtained from collaborators at the University of Houston, and grown using an ambient pressure CVD process described elsewhere [61]. This process is almost entirely the same as described in Chapter 3, but with differing gas flow rates and without pumping on the growth chamber (instead allowing the excess gas to exhaust). The sample was transferred onto oxidized silicon wafer in the usual manner. The graphene sample is monolayer over a large area, as was confirmed by Raman spectroscopy. Figure 4.1 shows a 2D mapping of the Raman spectrum of this graphene sample over a $10 \times 10 \mu\text{m}^2$ area. The color contrast shows the ratio of peak intensities ($I_{G'}/I_G > 2$) which is characteristic of monolayer, even for the smallest ratio area in the mapping (indicated by spot (a)). This large area monolayer graphene allows for measurement of TEP without undergoing any microfabrication steps. This avoids any further chemical treatment that could dope the graphene, or create additional surface charge that would alter the material's characteristics.

Figure 4.2 shows the experimental setup for the measurement of the TEP of the graphene samples. Two Chromel-Alumel thermocouples are placed at two points along the surface of the graphene, and are attached using a small amount of silver epoxy to ensure good physical and electrical connection to the graphene. A small platinum resistive heater (approximately the same length as the width of the graphene sample) is placed near the end of the graphene with silver epoxy, for use as a heat source. Two other copper wires (not shown in the diagram) were also attached at the

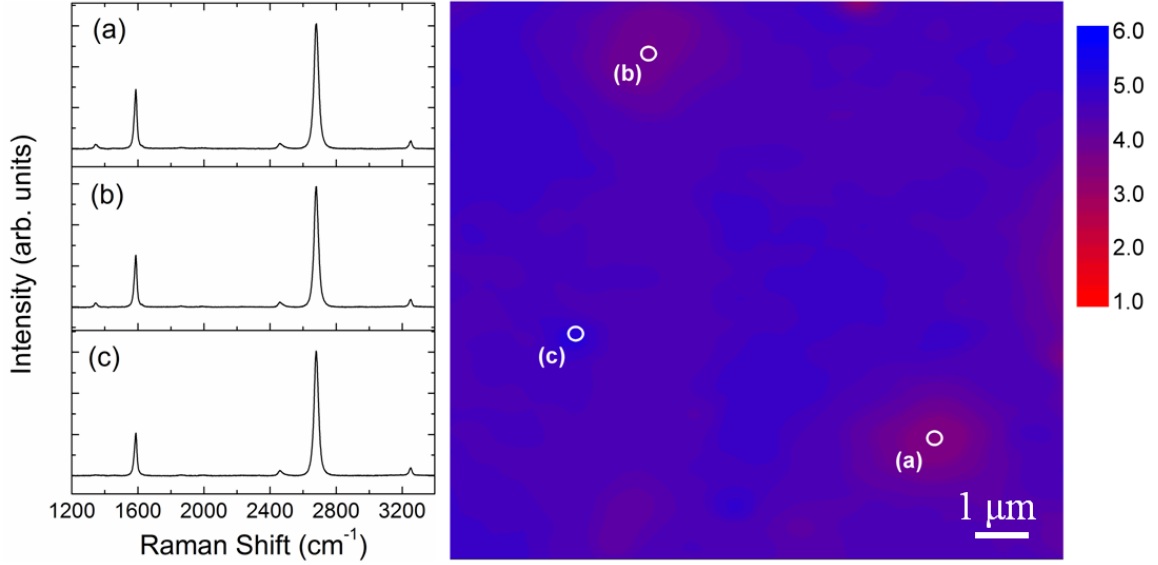


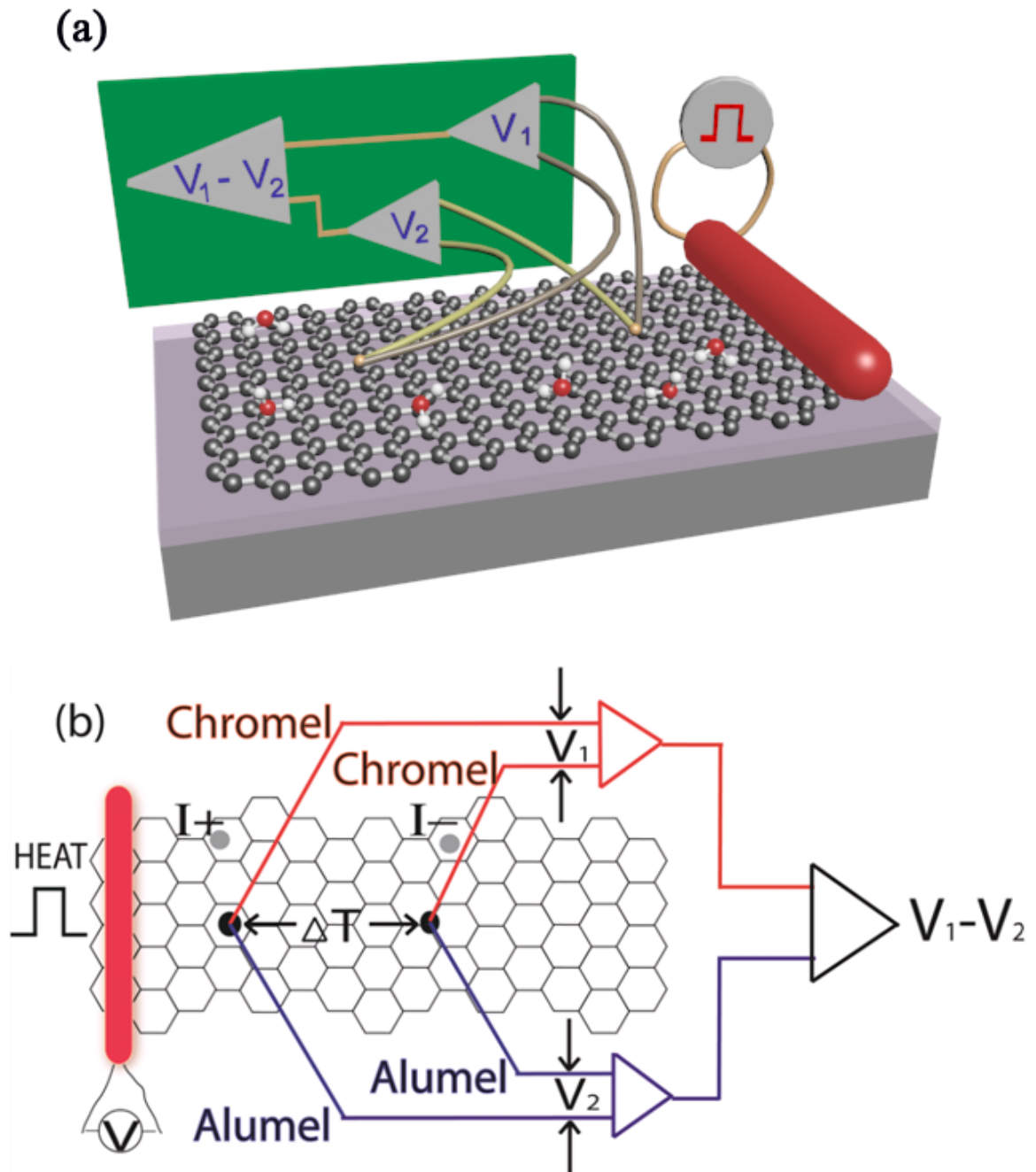
Figure 4.1: *Right:* Two-dimensional mapping of the Raman spectrum of the graphene sample used for the TEP measurement. The color contrast is the ratio of the peak intensities ($I_{G'}/I_G$). Panels (a)-(c) show selected spectra from individual points on the sample marked by circles.

same positions as the thermocouple junctions to allow for measurement of the four-probe resistance of the graphene.

The thermocouples used in this measurement are a combination of Alumel and Chromel wires (both alloys), and are referred to as K-type. Chromel is an alloy of 90% nickel and 10% chromium. Alumel is an alloy consisting of 95% nickel, 2% manganese, 2% aluminum, and 1% silicon. The wires are welded together using a special spot welding technique. The Alumel and Chromel wires are held together at one end by an alligator clip (electrically connected to the ground). A large voltage ($\sim 60 - 120$ V) is applied to a copper rod. The joint between the two wires is brought into contact with the rod. This transient contact creates a spark of plasma, which forms a bond approximately $120 \mu\text{m}$ in diameter. A typical junction is shown in Figure 4.3. These standard K-type thermocouples are calibrated to accurately relate the temperature T_{tc} at the junction to the thermo-voltage V_{tc} across the wires. This relationship is modeled using a polynomial expansion of the form

$$T_{\text{tc}} = \sum_{n=1}^9 d_n V_{\text{tc}}^n. \quad (4.17)$$

Values for the coefficients d_n are listed on the National Institute of Standards and Technology website (<http://srdata.nist.gov/its90/main/>), for various temperature ranges, with a listed error of



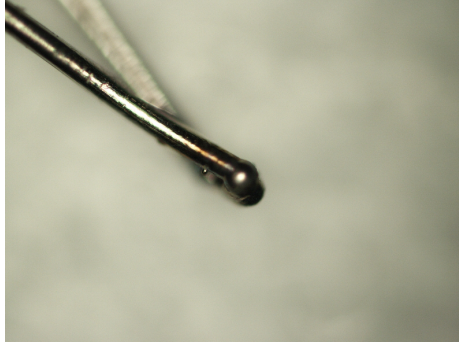


Figure 4.3: Optical micrograph of the junction between bare Alumel and Chromel wires, forming a K-type thermocouple.

Table 4.1: Coefficients used to calibrated K-type thermocouple voltage vs. temperature as in Eq. (4.17).

Expansion index, n	d_n ($^{\circ}\text{C}/\text{mV}^n$)	
	$-200 - 0$ $^{\circ}\text{C}$	$0 - 500$ $^{\circ}\text{C}$
1	$2.5173462 \times 10^{+1}$	$2.508355 \times 10^{+1}$
2	-1.1662878×10^0	7.860106×10^{-2}
3	-1.0833638×10^0	-2.503131×10^{-1}
4	$-8.9773540 \times 10^{-1}$	8.315270×10^{-2}
5	$-3.7342377 \times 10^{-1}$	-1.228034×10^{-2}
6	$-8.6632643 \times 10^{-2}$	9.804036×10^{-4}
7	$-1.0450598 \times 10^{-2}$	-4.413030×10^{-5}
8	$-5.1920577 \times 10^{-4}$	1.057734×10^{-6}
9		-1.052755×10^{-8}

-0.05°C to 0.04°C . In the range of temperatures used for this measurement ($300 - 500$ K), these coefficients d_n have a fixed set of values. Their values are listed in Table 4.2, as well as values for a lower temperature range which is used for experiments in Chapter 5. Comparing the values listed in the table, the linear terms' coefficient are about one or two orders of magnitude larger than the next largest coefficient for each range, respectively. So, to a good approximation the temperature read by the thermocouple is linear to the induced thermo-voltage between the wires.

A graphene sample is mounted onto a ceramic holder, with electrical connections made through a hermetically sealed feed through attached to a CF vacuum flange. The wires used for the holder/feed through connections were of the same corresponding thermoelectric materials as on the sample. This stage/seal setup allows for loading a sample into a vacuum environment. Further, by placing the sample holder in a vacuum sealed quartz tube, the sample can be heated to several

hundred degrees Celsius inside of a tube furnace. In this experiment, the voltage V_1 between the pair of chromel wires of the two thermocouples is measured with a Keithley 2182 nanovoltmeter. The corresponding voltage V_2 between the pair of alumel wires is measured similarly with a second nanovoltmeter. A temperature gradient is formed using a ceramic wire-wound Pt heater ($100\ \Omega$), by applying a ~ 10 mW square wave pulse with a duration of 3 – 5 s. The measured voltages are defined in terms of the Seebeck coefficients of the wires (S_A for Alumel, S_C for Chromel) and of graphene (S_G) and the temperature difference ΔT between the junctions:

$$V_1 = (S_G - S_C)\Delta T, \quad (4.18)$$

and

$$V_2 = (S_G - S_A)\Delta T. \quad (4.19)$$

Taking the difference in these voltages allows for extraction of the actual temperature difference between the two thermocouple junctions:

$$\Delta V = V_1 - V_2 = (S_A - S_C)\Delta T. \quad (4.20)$$

For the listed experimental conditions, this gives a difference in temperature of $\Delta T \approx 1$ K. The value of S_G is then obtained using the basic definition from Eq. (4.1), by using either of V_1 or V_2 .

4.3 Results & Discussion

Now that the basic techniques of this measurement have been developed, this section will discuss specific experiments measuring TEP in CVD grown graphene. The Seebeck coefficient was measured under ambient conditions, in vacuum during an annealing process, and under exposure to various gaseous species. The implications of all of these processes are discussed in terms of possible device applications with graphene acting as a chemical/biological sensor.

4.3.1 Vacuum Annealing

In ambient conditions, graphene is in the presence of O_2 and H_2O as well as other trace gases. This is especially true for CVD graphene samples that have undergone several treatments in aqueous solutions for the transfer process. These species generally create p-type doping of the graphene, and shift the Fermi level below the charge neutral point. To obtain a true measure of graphene's intrinsic

Seebeck coefficient requires the removal of these surface adsorbates. To this end, a standard annealing process is to place a graphene sample in ultra high vacuum (UHV), and to heat it until all of the O_2 and H_2O is desorbed. As a first experiment, this was performed by placing the aforementioned graphene sample setup into a UHV chamber which was placed into a tube furnace with control from room temperature to 500 K in this case, following a similar recipe for annealing carbon nanotubes [62].

The results of this annealing process are shown in Figure 4.4. The sample was pre-pumped to a base pressure below 10^{-6} Torr with a turbo molecular pump, and was pumped on during the entire measurement. The temperature was changed in three stages: (1) heating to the maximum, (2) dwelling at the highest temperature, (3) cooling back to room temperature. During the stage (1), initially S increases quadratically with temperature as is expected for the screened charge impurities. This increase in S is followed by a sharp reversal (at $\sim 400 - 500$ K), decreasing dramatically and reaching a negative value ($S \approx -50 \mu V/K$) at the maximum temperature $T = 500$ K, only changing slightly during the dwell period. As the sample is cooled back to room temperature S increases linearly and then saturates at $-32 \mu V/K$. This linear increase is as expected from the Mott formula, and from measurements on exfoliated graphene [53]. During this same process, the sample resistance increases from the initial value $R \approx 3.7 k\Omega$, reaching a peak of $5.4 k\Omega$ before the maximum temperature is reached. The resistance decreases to $2.3 k\Omega$, as the temperature is maintained at the constant 500 K. During cooling, R decreases further, reaching a final saturated value near $2.0 k\Omega$.

Figure 4.4 (c) plots both variables (S and R) on the same graph over the range of heating and part of the dwell period. This data was acquired by our collaborators at the University of Louisville. From this graph it is clear that the crossover in the sign of S occurs at the same time R reaches its peak value. This correspondence is as expected from the behavior of increasing the Fermi level from the valence band through the charge neutral point and then filling states in the conduction band. As the sample is annealed, degassing decreases the density of holes, accompanied by the decreasing positive Seebeck coefficient. The Fermi level passes through the Dirac point ($S = 0$), and then increases filling more electron states increasing their density. The Seebeck coefficient becomes increasingly negative until fully degassed. All samples undergoing this annealing process show this

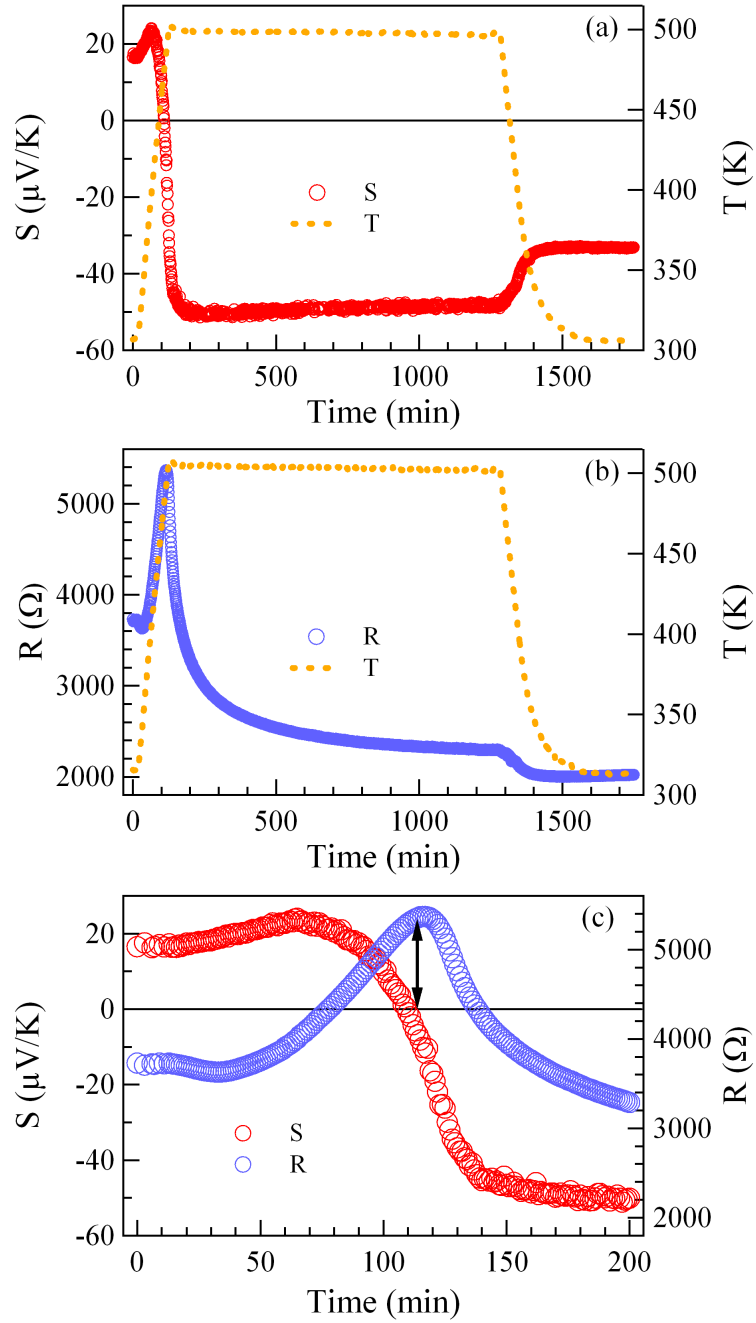


Figure 4.4: Simultaneous measurements of (a) the Seebeck coefficient S and temperature T , (b) sample resistance R and T , and (c) S and T during the annealing process.

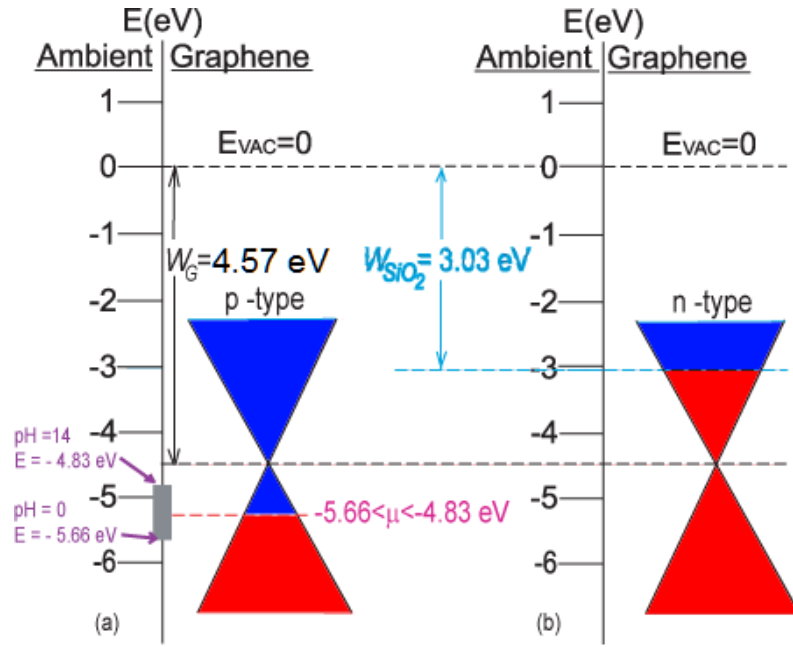


Figure 4.5: Electronic band structure lineup of graphene with its surroundings for (a) ambient conditions and (b) the degassed SiO₂ substrate.

final n-type behavior.

Both the initial p-type behavior, and the final (annealed) n-type behavior can be explain in terms of charge transfer between the graphene and its substrate. The same behavior has been seen in various carbon systems: for mats of single wall carbon nanotubes (CNT) [62], CNT field effect transistors [63, 64], diamond [65], and hydrogen-terminated diamond electrodes [66]. Figure 4.5 demonstrates the lineup of the band structure of graphene with its surroundings. For samples in ambient conditions, the charge transfer is mediated by the water and oxygen present between the graphene and SiO₂ substrate, and on the graphene surface. In this environment there is a redox coupled reaction leading to a mildly acid layer:



Depending on the pH of this ambient layer, the redox potential of the oxygen is between -5.66 eV (pH = 0) and -4.83 eV (pH = 14) with respect to the vacuum energy level [65]. By comparison the work function for electrons in graphene near the Dirac point is approximately 4.57 eV for single layer graphene [67]. When the Fermi level of the graphene lies within the range of energies for the redox couple, there is simultaneous charge transform from the graphene to the oxygen/water layer.

This explains the p-type behavior of graphene, as the relevant energy range is well below the Dirac point.

In the fully degassed conditions, the oxygen/water layer is not present. Graphene is then sitting on a bare SiO₂ substrate without the presence of surface adsorbates. The work function for SiO₂ can vary depending on its amorphous structure, but is on the order of 3 eV [68]. From Figure 4.5 (b), we can make an analogous argument about the lineup of the band structure of graphene with the substrate. In this case, there is a simultaneous charge transfer of electrons from the substrate to the graphene which pins the Fermi level near the work function of the SiO₂. It is clear this gives rise to the n-type behavior of the degassed graphene samples.

4.3.2 Sensing Applications

The last section demonstrated that the thermoelectric power of graphene is highly sensitive to surface adsorbates and charge doping. This opens the possibility of exploiting this property for using graphene as a gas sensor. Measurements of TEP on graphene have been performed for various gas environments. TEP is both sensitive to the presence of gas environments, but is also sensitive to the type of environment as well through the charge doping. The electrical resistance of CVD grown graphene can also be used as a sensitive probe of its environment.

Taking the same experimental setup, graphene samples were fully degassed using the aforementioned annealing process. This left the graphene sample with $S = -32 \mu\text{V/K}$, for the characteristic n-type behavior discussed. The sample was then exposed to either air, N₂O, or NH₃. The Seebeck coefficient was monitored over a long time until it reached a saturated value. The results are shown in Figure 4.6. For the exposure to air and N₂O, the TEP saturated to a positive value, indicating p-type doping of the graphene. The final saturated values for S , and dS/dt were different for the two gases. For exposure to NH₃, S reaches a negative saturated value, indicating n-type doping of the graphene. This difference in S for the two adsorbed nitrogen containing species is consistent with the charge transfer predicted by density function theoretical calculations [69]. These calculations show a charge transfer of $-0.099e$ and $0.027e$ from/to graphene for the adsorption of N₂O and NH₃, respectively. This agrees with the qualitative behavior of each gas, and the relative magnitude of the response of S . The value of saturated value of S , and its rate of change could be exploited for

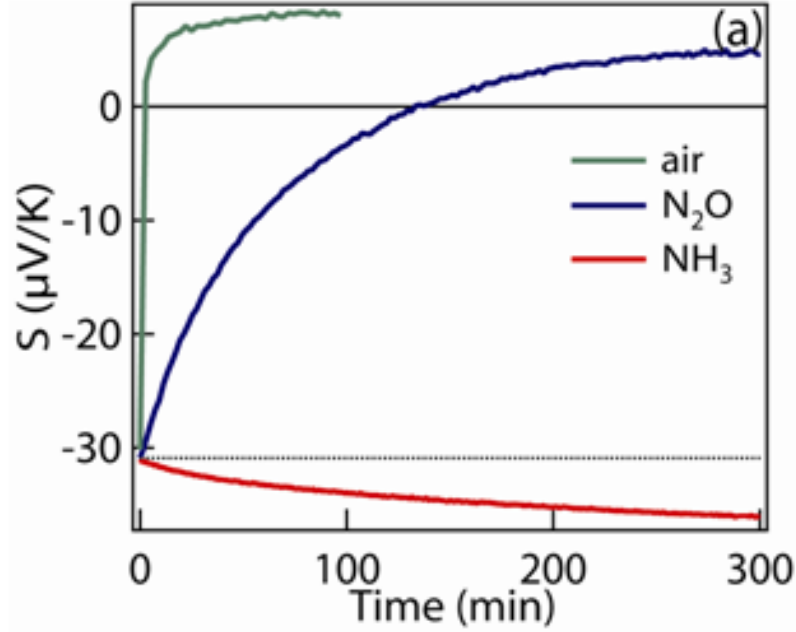


Figure 4.6: Response of the thermoelectric power of graphene upon exposure to various gaseous species.

not only sensing gases, but also for differentiation between similar species. Lastly, the annealing process described here consistently recovers the final degassed value of $S = -32 \mu\text{V/K}$. Repeated cycling of samples to gas exposure and annealing shows no poisoning effects, regardless of the type/amount of gas introduced.

Graphene has also been proposed as a sensor for biological applications as well. One particular type of sensor involves testing small samples of blood. Two controlled experiments were performed comparing the resistance of CVD graphene under exposure to water and blood. Large area samples of graphene were transferred onto Si/SiO₂ substrates and aluminum leads were placed in the standard 4-point probe configuration for measuring resistance. The sample resistance in both cases were on the order of $\sim 300 \Omega$ under ambient conditions.

For both samples of graphene, the resistance was recorded over time as a single drop of each agent was introduced onto the sample surface. The response of the change in sample resistance ΔR for both experiments is shown in Figure 4.7. Both for the water and blood, there is a sharp increase in resistance over a few seconds. For the case of introducing water, ΔR reaches a peak value of 420Ω , then gradually decreases and reaches a steady state value of 310Ω . This steady state is

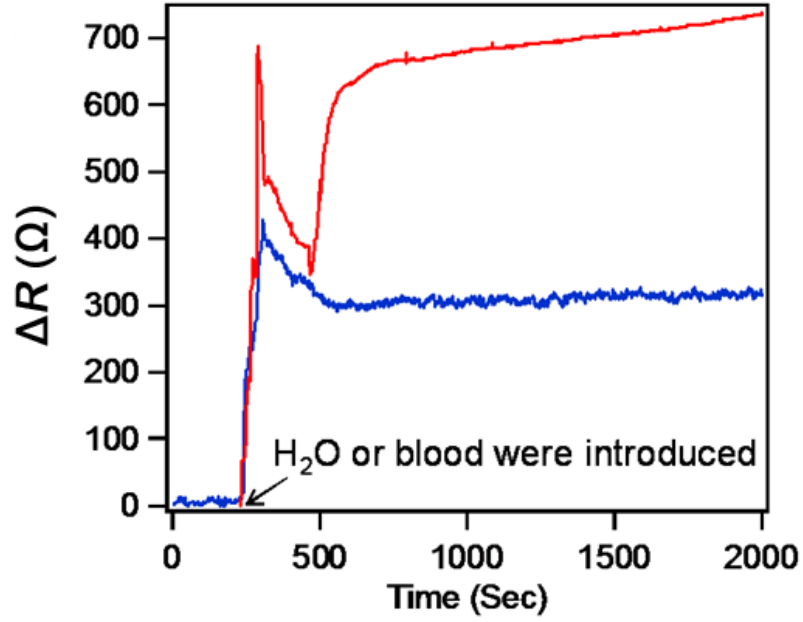


Figure 4.7: Change of the resistance of CVD graphene samples with the introduction of water (blue) and blood (red).

presumably reached when the excess water on the graphene surface evaporates to conditions that match the surrounding humidity. For the introduction of blood, ΔR reaches a peak value of $\sim 700 \Omega$, and then sharply decreases to 350Ω at nearly the same rate as for the water drop. This decrease in ΔR is followed by another sharp increase, eventually reaching values larger than for the initial introduction to the graphene surface. This last dramatic change in ΔR is attributed to clot formation, which has been previously observed in graphene oxide [70].

4.4 Conclusion

We have measured the thermoelectric power of CVD grown graphene in response to various environments. Making a comparison of the TEP of graphene in a vacuum annealed environment to that of the ambient we have illustrated the applicability of a charge transfer mechanism between graphene's adsorbates and its substrate. With this understanding of the TEP response we have measured its changes with the introduction of various pure gaseous environments. Comparing this with concurrent measurements of resistance change it is clear that TEP of graphene is a strong sensor to gas adsorbates. Further studies on the exact sensitivity and the ability to differentiate between gases in a mixed environment would be required for building commercial sensors with graphene. The

sensitivity of graphene based sensors to liquid (e.g., blood) might open up a new area of research and development in medical/bio device applications.

CHAPTER V

THERMAL CONDUCTIVITY OF GRAPHENE

As alluded to in the overview of graphene, it is expected to be an excellent thermal conductor. Generally this is due to the strong covalent bonding between carbon atoms which supports high frequency phonon transport. Similarly, this property accounts for the high thermal conductivities of graphite, carbon nanotubes, and to some extent diamond. Some efforts have been made to measure the thermal conductivity κ of graphene on small samples, but suffer from deficiencies in their measurement techniques, and in most cases have a large range of values.

A summary of the previous measurements is listed in Table 5. As one can see, there is a strong dependence of the values on what type of sample is measured, and what technique is utilized. There is an urgent need for knowing a precise value at room temperature, specifically for use in manufacturing graphene devices that exploit this thermal property. Beyond that, the physical mechanism for the heat conduction in graphene should be understood. The description of this mechanism can be most effectively understood by studying the temperature dependent thermal conductivity $\kappa(T)$. The measurements presented in this Chapter will focus on the temperatures range around room temperature (200 – 400 K).

Table 5.1: Comparison of various measurements of thermal conductivity κ for graphene.

Sample Type						
Ref.	CVD/Exfoliated	Layers	κ (W/m K)		Method	Suspended/Supported
[71]	Exfoliated	1	3080 - 5300	350 K	optical	Suspended
[72]	CVD	1	1450 - 3600	350 K	optical	Suspended
			920 - 1900	500 K		
[72]	CVD	1	50 - 1020	300 K	optical	Supported
[73]	Exfoliated	3	170 - 1250	300 K	electrical	Supported
			220 - 1350	350 K		
[74]	Exfoliated	1	545 - 613	300 K	electrical	Supported

5.1 Theoretical Background

Thermal conductivity is a measure of how well heat is transmitted through a solid material. It depends greatly on the type of material (metal/semiconductor/insulator). Generally materials that are good electrical conductors are also good thermal conductors, with a couple notable exceptions being diamond and sapphire (Al_2O_3). For a bulk piece of material, the rate at which heat flows \dot{Q} follows Fourier's law:

$$\dot{Q} = -\kappa A \nabla T, \quad (5.1)$$

where A is the cross-sectional area, and T is the local temperature. This law is the steady state description of the heat equation. The general heat equation for a spatio-temporal temperature distribution $T(\mathbf{r}, t)$ is $\partial_t T \propto \nabla^2 T$. This is a partial differential equation, and can be solved with given boundary conditions. For the purposes of this thesis, only the steady-state situation will be considered.

In the linear response regime, we can recover the Fourier law in the semi-classical approximation. Equations (4.2) and (4.3) related the electrical and thermal current to an applied electric field and thermal gradient. If there is no electrical current ($\mathbf{j} = 0$), then the electric field can be written in terms of the thermal gradient:

$$\mathbf{E} = -(L^{11})^{-1} L^{12} (-\nabla T). \quad (5.2)$$

The thermal current can then be expressed as

$$\mathbf{j}^{\text{th}} = \kappa (-\nabla T), \quad (5.3)$$

where κ has been defined in terms of the L^{ij} as $\kappa = L^{22} - L^{21}(L^{11})^{-1}L^{12}$. This is exactly the Fourier law, with the identification of $\mathbf{j}^{\text{th}} = \dot{Q}/A$. If we make the same approximation as before, using a Sommerfield expansion of the coefficient L^{22} , then to order $(k_B T/\varepsilon_F)^2$,

$$\kappa = L^{22} = \frac{\pi^2}{3} \frac{k_B^2 T}{e^2} \sigma. \quad (5.4)$$

This equation is also known as the Wiedemann-Franz law (WF), where the ratio κ/σ is proportional to the temperature, with a proportionality constant $L_0 \approx 2.4 \times 10^{-8} \text{ W } \Omega \text{ K}^{-2}$ (Lorenz number). This equation can hold over a wide range of temperatures, as long as the condition of elastic scattering

holds. Of course for the case of graphene, this expression is not known to hold, and it has been shown that inelastic phonon scattering also plays a large role [8]. In fact, in the range of temperatures studied, the electronic contribution to κ is negligible compared to that of the phonons in graphene [75].

5.1.1 Phonon Contribution to κ

The collective lattice vibrations of graphene (phonons) give rise to the majority contribution to the thermal conductivity at medium to high temperatures ($T \gtrsim 200$ K). For monolayer graphene there are six phonon branches: three optical, and three acoustic phonons. The amount of energy they carry and their contribution to κ depend on their energy dispersion. Figure 5.1 shows the dispersion of these phonon modes along the $\Gamma - M$, $M - K$, and $\Gamma - K$ directions calculated using the valence-force field (VFF) method [8]. The VFF method, which accounts for the the force constants from both in-plane and out-of-plane bending and stretching. The phonons are labeled for the longitudinal (L), transverse (T), out-of-plane (Z), acoustic (A) or optical (O) modes. The following calculations for κ will concern the three acoustic modes (that dominate the heat transport). Of those, the in-plane (LA, TA) modes follow approximately linear dispersion with a frequency given by

$$\omega_s = v_s q, \quad (5.5)$$

where s labels the mode, and v_s is the corresponding group velocity ($d\omega_s/dq$); $q = 0$ is taken at Γ . The ZA phonon mode follows a quadratic dispersion, with a frequency

$$\omega_{ZA} = \alpha q^2 \quad (5.6)$$

where α is a proportionality constant.

The heat flux due to phonons can be expressed in terms of the mode energy $\hbar\omega_s$ and the non-equilibrium part of the phonon distribution function $N = N_0 + n$. Taking $N_0 = [\exp(\hbar\omega_s/k_B T) - 1]^{-1}$ as the Bose-Einstein distribution function, we can define the non-equilibrium part as

$$n = -\tau_{\text{tot}} \frac{\partial \omega_s}{\partial q} \frac{\partial N_0}{\partial T} \nabla T, \quad (5.7)$$

where τ_{tot} represents the total phonon relaxation time. With this definition, we can write the heat

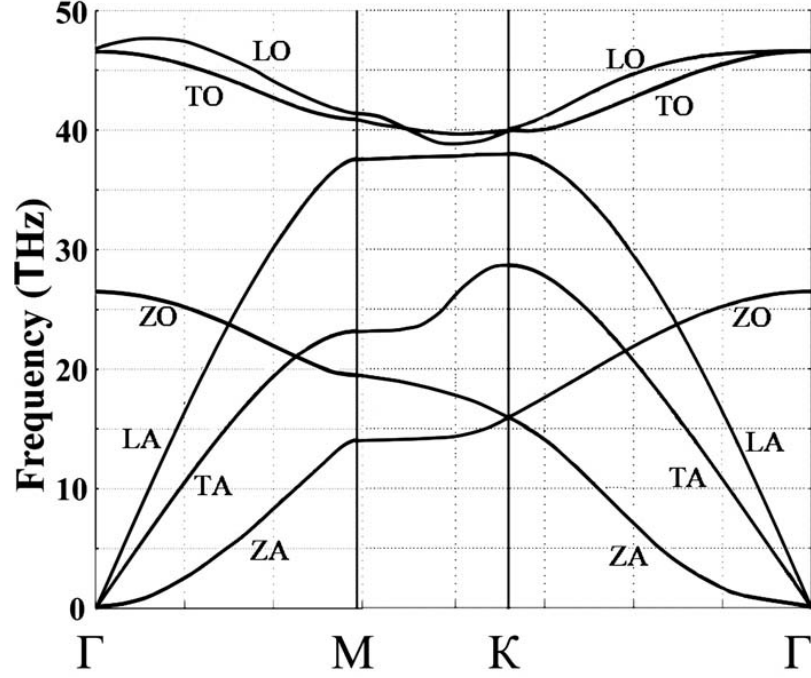


Figure 5.1: Dispersion of the phonon modes of graphene calculated using the valence-force field method. Taken from [8].

flux as

$$\begin{aligned}\dot{Q} &= \sum_{s,q} \hbar \omega_s(q) n(q, \omega_s) \frac{\partial \omega_s}{\partial q} \\ &= - \sum_{\beta} (\nabla T)_{\beta} \sum_{s,q} \tau_{\text{tot}}(s, q) \left(\frac{\partial \omega_s}{\partial q} \right)_{\beta} \frac{\partial N_0}{\partial T} \frac{\partial \omega_s}{\partial q} \hbar \omega_s(q).\end{aligned}\quad (5.8)$$

Comparing this expression with Eq. (5.1), we can find an expression for κ . If we make the transformation from a sum to an integral using the expression for the phonon density of states the final result is for the scalar thermal conductivity is

$$\kappa = \frac{1}{4\pi k T^2 d} \sum_s \int_0^{q_{\text{max}}} \left[\hbar \omega_s(q) \frac{d\omega_s(q)}{dq} \right]^2 \tau_{\text{tot}}(s, q) \frac{\exp[\hbar \omega_s(q)/kT]}{[\exp[\hbar \omega_s(q)/kT] - 1]^2} q dq, \quad (5.9)$$

where again $s = \text{LA, TA, ZA}$ are the three acoustic modes.

As proposed by Nika, *et al.*, the phonon relaxation channels in graphene are predominated by three-phonon umklapp processes. A thorough calculation of the relaxation time accounting for all possible channels has been performed [8]. The end result is a relaxation time for Umklapp scattering τ_u that is extracted from a simple analytical expression for the phonon mean free path:

$$\tau = \frac{1}{\gamma_s^2} \frac{M v_s^2}{k_B T} \frac{\omega_{s,\text{max}}}{\omega^2}, \quad (5.10)$$

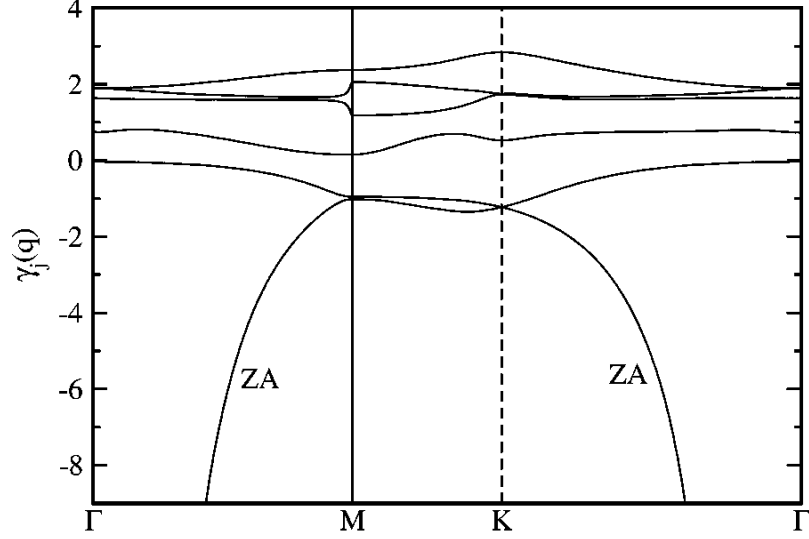


Figure 5.2: Grüneisen parameters for each phonon mode in graphene, calculated *ab initio* using the quasiharmonic approximation in density-functional perturbation theory. Taken from [9].

where M is the mass of a graphene unit cell, $\omega_{s,\max}$ is the maximum cut-off frequency for a given phonon branch, and γ_s is a mode dependent Grüneisen parameter [76]. The Grüneisen parameters for each of the phonon modes of graphene have been calculated using density functional theoretical models, and are shown in Figure 5.2 [9]. Furthermore, there is a limitation on the maximum phonon mean free path being no larger than the sample dimension L . In the case studied for polycrystalline CVD grown graphene, we can take $L (\lesssim 10 \text{ } \mu\text{m})$ to represent the average size of single crystal domains. This leads to a minimum cut-off phonon frequency

$$\omega_{s,\min}^2 = \frac{v_s}{\gamma_s^2} \frac{M v_s^2}{k_B T} \frac{\omega_{s,\max}}{L}. \quad (5.11)$$

With these considerations, we can calculate an analytical model for the lattice thermal conductivity of graphene. The summation in Eq. (5.9) includes two linear modes, and one quadratic mode. The contribution from the two linear modes has the same algebraic form, just with differing parameters. Substituting in the expression in Eq. (5.10) for the linear mode dispersion into Eq. (5.9) gives the expression

$$\frac{M}{4\pi T d} \frac{\omega_{s,\max} v_s^2}{\gamma_s^2} F^{(1)}(\omega_{s,\max}, \omega_{s,\min}), \quad (5.12)$$

where the function $F^{(1)}$ is defined as

$$\begin{aligned} F^{(1)}(\omega_{s,\max}, \omega_{s,\min}) &= \int_{\hbar\omega_{s,\min}/k_B T}^{\hbar\omega_{s,\max}/k_B T} x \frac{e^x}{(e^x - 1)^2} dx \\ &= \left[\ln(e^x - 1) + \frac{x e^x}{1 - e^x} \right]_{\hbar\omega_{s,\min}/k_B T}^{\hbar\omega_{s,\max}/k_B T}. \end{aligned} \quad (5.13)$$

Note that in this instance, the s refers to the modes LA and TA only. For the quadratic mode, the corresponding expression is

$$\frac{2k_B M}{\pi \hbar h} \frac{\alpha \omega_{ZA,\max}}{\gamma_{ZA}^2} F^{(2)}(\omega_{ZA,\max}, \omega_{ZA,\min}), \quad (5.14)$$

where the function $F^{(2)}$ is defined as

$$\begin{aligned} F^{(2)}(\omega_{ZA,\max}, \omega_{ZA,\min}) &= \int_{\hbar\omega_{ZA,\min}/k_B T}^{\hbar\omega_{ZA,\max}/k_B T} x^2 \frac{e^x}{(e^x - 1)^2} dx \\ &= \left[2x \ln(1 - e^x) + \frac{x^2 e^x}{1 - e^x} + 2 \sum_{n=1}^{\infty} \frac{e^x}{n^2} \right]_{\hbar\omega_{ZA,\min}/k_B T}^{\hbar\omega_{ZA,\max}/k_B T}. \end{aligned} \quad (5.15)$$

With these calculated expressions, the total lattice thermal conductivity is then the sum over the contribution from each part. While not very simply defined, this is in fact an analytical model for thermal conductivity which can be used to fit experimental data.

5.2 Comparative Measurement of Thermal Conductivity

The actual measurement of the thermal conductivity of graphene poses quite a technical challenge. Typical measurement techniques for thin films include: thermoreflectance, the 3ω method, scanning thermal microscopy, and various custom methods employing microfabricated structures [77]. The most popular of these methods (3ω) has a requirement that the sample thickness is more than five times larger than the lateral dimension of the temperature sensors, which is difficult to satisfy for monolayer graphene [78]. The 3ω method has been modified for multilayer systems [79], and there could be a possibility of modifying this method for such a thin layer. Thermoreflectance measurements generally require ultrafast lasers and measures interface conductance [80]. The remaining methods will be discussed further in this section and the next.

As mentioned in the introduction of this Chapter, several measurements of κ have already been made on graphene. The optical measurements use a Raman setup for both laser heating of the

sample, and measurement. This technique tracks the shift in the G peak position as a function of applied power (and thus sample local temperature)[71]. Since this G peak position is associated with the inelastic light scattering process near the Γ point, there is ambiguity on the contribution coming from either the LO or TO phonon branches. The accurate measurement of temperature using this method is difficult, and has not been fully characterized. Also, the laser has the possibility of altering the graphene by thermal annealing surface adsorbates. The electrical measurements employ complicated microfabricated structures. This suffers from exposing the graphene sample to further chemical processing that can induce charge doping [74]. Our method avoids microfabrication for depositing metal contacts to graphene and allows for more accurate temperature measurements.

To measure κ for our large area CVD grown graphene samples we employ a comparative technique similar to measure mats of SWCNTs [81]. The basis for this method is to have a material with a known thermal conductivity in series with the material under test (graphene). By minimizing the heat loss due to radiation and convection, the heat flow through both materials should be nearly the same. A sample of graphene grown by the CVD method described in Chapter 3 is transferred onto either a small piece of a pre-cleaned glass slide or oxidized silicon wafer. The choice of substrate will be discussed later. The substrate is large enough to allow enough room on either side of the graphene for blank substrate. For use as a comparative sample, we chose evaporated gold. A carefully prepared shadow mask of aluminum foil is used to cover a small section of the graphene sample. A bilayer of Ti/Au (5 nm/50 nm thickness) is then deposited in a CVC Electron Beam Evaporator. The thin layer of titanium is used as an adhesion layer between the substrate and the gold film. These deposited films are generally polycrystalline in nature. It has been shown that the WF law is applicable to these types of films down to 80 K, with the Lorenz number being independent of temperature [82]. A separate sample of the same clean substrate (no graphene) is also deposited with metal in the same run for metal film characterization.

The clean substrate with just the deposited gold is used to measure the thermal conductivity of the film used for actual graphene measurement. The electrical conductivity is measured at room temperature by the van der Pauw method. A probe station allows for measurement of the four-probe resistance in varying configurations, from which σ is extracted. Using the WF law, κ for gold is calculated, with typical values of $\kappa_{Au} \sim 100$ W/m K. This is lower than the bulk value (~ 300 W/m

K), but typical for these types of nanofilms.

The gold/graphene sample is loaded onto a ceramic sample stage by placing a small amount of silver paint on the back side as an adhesive. The measurement setup is shown schematically in Figure 5.3 (a). A ceramic coated Pt heater is mounted near either end of the sample with a small amount of GE varnish, for use in creating a thermal gradient. Three sets of K-type differential thermocouples are mounted with varnish or high temperature thermal epoxy. Two of the differential thermocouples are mounted entirely on the gold coated substrate portion (no graphene), while the last differential thermocouple straddles the graphene portion of the sample. Differential thermocouples are used to measure the change in temperature ΔT_j between the two junction points. The dimensions of the sample, and the lengths between the two junctions of each thermocouple are carefully measured using an optical microscope. A photograph of a fully wired sample is shown in Figure 5.3 (b). The other ends of the heater and thermocouple wires are attached to electrical leads which are connected to a hermetic feed through mounted onto a custom CF flange. This flange can be used to seal this sample mount in a vacuum enclosure to be pumped to UHV conditions.

The comparative technique exploits the condition that the heat flowing measured by one set of differential thermocouples (e.g., on gold film) must be nearly the same as that measured by the next set (on graphene). Due to the interface, there may be some thermal resistance between the gold films and the graphene. In general, this means as heat flows away from the source (Pt heater), there must be a larger amount of heat flowing through the material closer to the source than that of the differing material further from the source. Referring to the diagram, taking the gold film to the left of graphene, this would require $\dot{Q}_{\text{Au}^{\text{left}}} \geq \dot{Q}_{\text{gr}}$. For the other pair, the situation would be the opposite. In this case, the graphene would be closer to the heat source, and therefore, the (far) gold film would have a smaller amount of heat flow than that of graphene, $\dot{Q}_{\text{gr}} \geq \dot{Q}_{\text{Au}^{\text{right}}}$. In this manner, depending on which pair of differential thermocouples is used from the measurement, an upper and lower bound for the thermal conductivity of graphene can be obtained. Defining x_j to be the distance between the junctions of the differential thermocouple (ΔT_j), the heat flow through the corresponding material can be written as

$$\dot{Q}_j = \kappa_j A_j \frac{\Delta T_j}{x_j}, \quad (5.16)$$

where A_j is the cross sectional area of that film. Using the conditions on the heat flow outlined

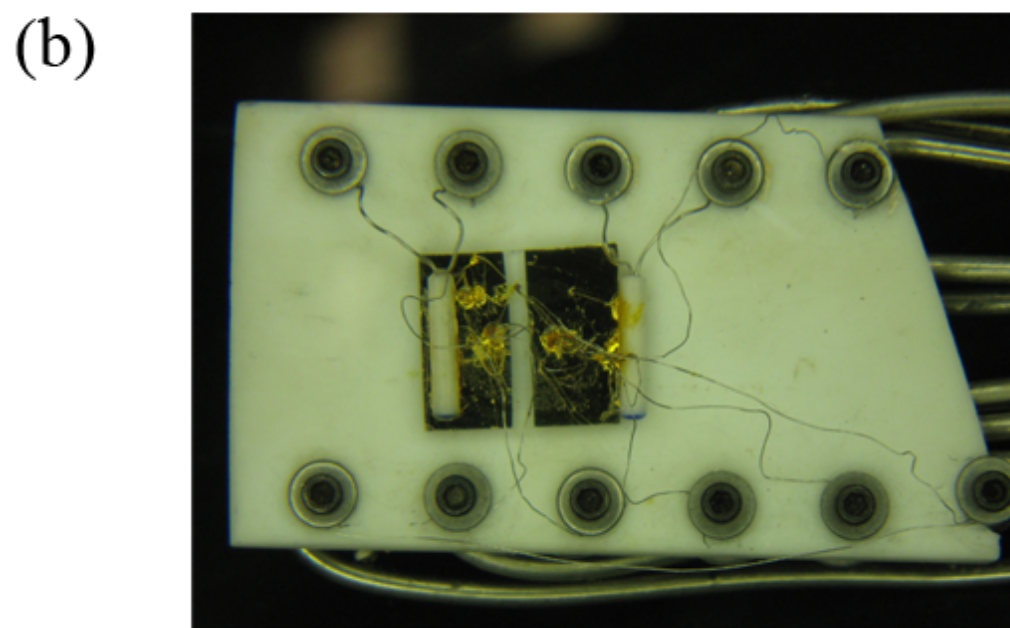
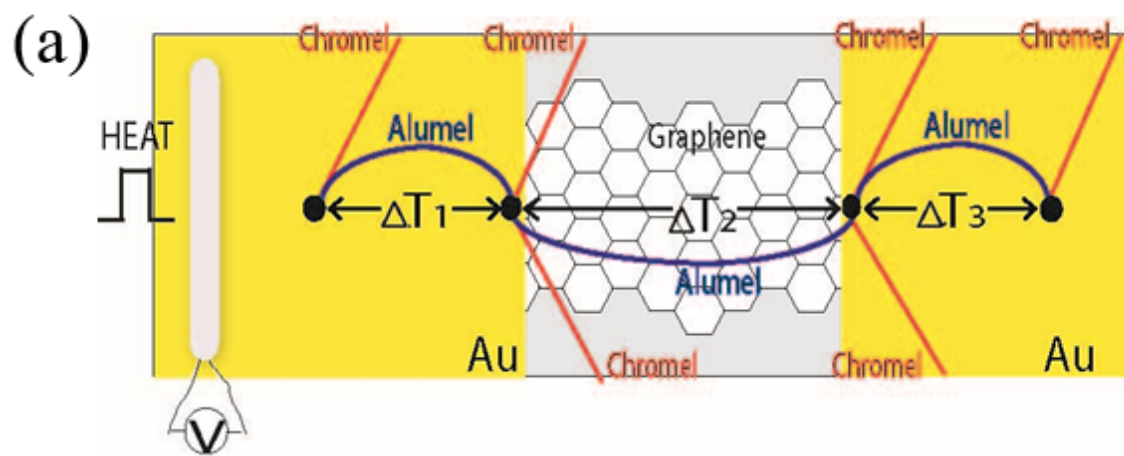


Figure 5.3: (a) Schematic of the sample setup for the (all electrical) measurement of the thermal conductivity of graphene. (b) Photograph of an actual measured sample mounted on the sample stage.

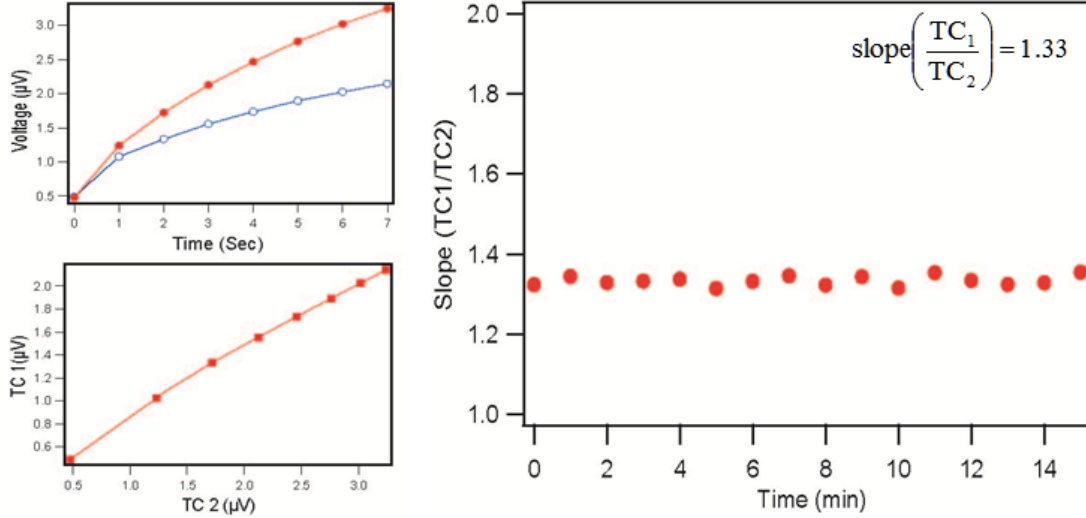


Figure 5.4: *Left:* Typical thermocouple response. *Right:* Corresponding ratio of thermocouple voltages.

above, we can write expressions for the bounds on κ_{gr} as:

$$\kappa_{gr} \leq \kappa_{Au} \frac{\Delta T_1}{\Delta T_2} \frac{x_2}{x_1} \frac{A_1}{A_2}, \quad (5.17)$$

and

$$\kappa_{gr} \geq \kappa_{Au} \frac{\Delta T_3}{\Delta T_2} \frac{x_2}{x_3} \frac{A_3}{A_2}. \quad (5.18)$$

To illustrate the data collection process, and the check the validity of this method, a control measurement was made, but with only a gold film (no graphene). Two pairs of differential thermocouples were compared on the same continuous film. The film was heated by applying ~ 1 mW of power to the Pt heater, which produces a thermal gradient ($\Delta T \approx 1$ K between the differential thermocouple junctions). The voltage difference between the two pairs of thermocouples is recorded over time using a custom LabView program. The results for this calibration test are shown in Figure 5.4. Clearly, the ratio of the thermocouple voltages is approximately constant as required for the steady-state assumption. Using a calculation similar to that of Eq. (5.17) the result was that the extracted value for thermal conductivity of gold was within a 5% error. This can be taken as the relative error for this type of measurement scheme. Independent calculations of the heat flow between successive pairs of thermocouples show less than a 1% error. This means the major source of overall error comes from the measurements of the geometric dimensions.

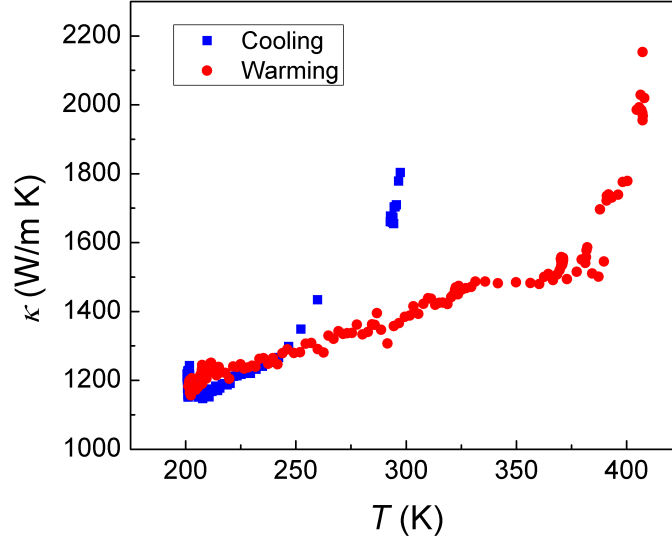


Figure 5.5: Temperature dependence of κ_{gr} for supported CVD grown graphene on glass. Blue squares represent data taken during cooling from room temperature. Red circles are data taken while warming from the lowest to the highest achievable temperatures.

We performed measurements of κ_{gr} using this technique on both glass and oxidized silicon substrates. Using glass as a substrate, a graphene sample was placed on our custom sample mount and a large (25 Ω , 100 W) cartridge heater was fixed to the backside. The entire stage was placed into a vacuum sealed stainless steel enclosure. The sample was pumped to low pressures (10^{-7} Torr) to minimize any effects of convective heat transfer. The entire sample enclosure was slowly placed in a filled liquid nitrogen dewar. A custom Labview program records measurements at various points during the cooling of the sample. For each measurement, the local temperature recoded by the thermocouples fixed on the sample is allowed to equilibrate. The listed values of temperature were those determined by the thermocouples before any heat was applied by the Pt heater. The results of these measurements are shown in Figure 5.5. Two stages of measurements are shown: one as the sample is cooled from room temperature to the lowest base temperature, and also as it is heated to the highest attainable temperature. The value of κ_{gr} measured at room temperature was ~ 1800 W/m K. During the cooling cycle, there is a sharp decrease in κ_{gr} , reaching ~ 1200 W/m K at the lowest temperature ($T \sim 200$ K). This low temperature is well above that of the liquid nitrogen (77 K) illustrating how well the sample is thermally insulated from the surroundings. For the warming cycle,

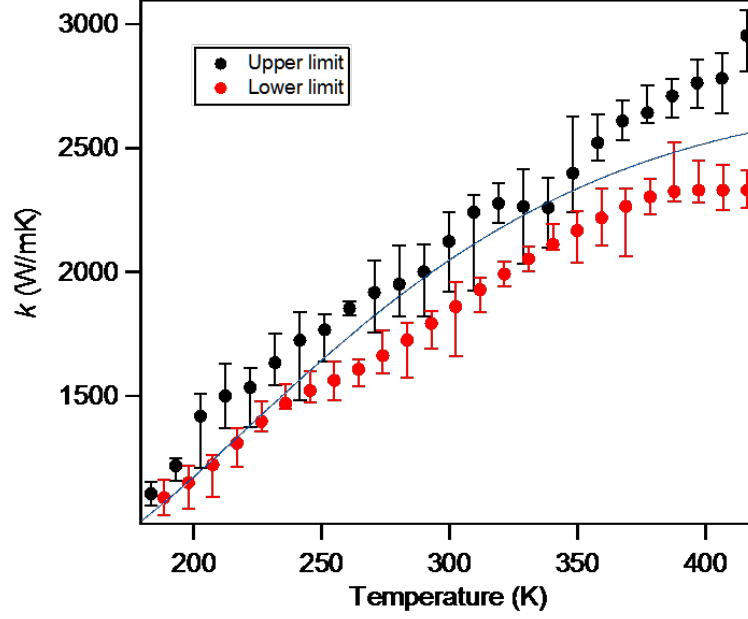


Figure 5.6: Temperature dependence of κ_{gr} for supported CVD grown graphene on SiO_2/Si . Black circles show the upper boundary limit for κ_{gr} , while red circles show the lower boundary limit. The solid blue line is a fit of the data to our theoretical model.

κ_{gr} retraces the same values from the cooling cycle up until $T \sim 250$ K. At this point, there is a large relative divergence between the two curves. Furthermore, there is an abrupt increase in κ_{gr} around $T \sim 375$ K, with κ_{gr} reaching 2,150 W/m K at the highest temperature. We attribute the hysteresis, and sharp changes to a physical rearrangement of the graphene on the substrate. Graphene has a negative coefficient of thermal expansion ($\beta \approx -6 \times 10^{-6} \text{ K}^{-1}$, nearly constant for $T > 200$ K) [83]. Our AFM measurements show that the glass substrate has a large surface roughness, meaning the graphene has relatively poor surface adhesion. These effects create ambiguity in determining what the true value for κ_{gr} is at a given temperature.

To eliminate this difficulty, we also measured graphene samples on oxidized silicon substrates. The root mean squared surface roughness of thermally grown SiO_2 is about 0.2 nm [84], which is 5 - 10 times smaller than that of typical polished glass [85]. The typical 300 nm thick oxide layer silicon wafers were used as the sample substrate. Measurements similar to that outlined for the glass substrate samples were performed. In this case, we performed two or more full thermal cycles (cooling/warming) for several samples. Data obtained from one of these samples is presented in Figure 5.6. Each data point shown represents the average of data taken in a small window of

temperatures, with the error bars shown being computed from the variations of that same subset of measurements. At room temperature κ_{gr} is bonded between 1750 - 2000 W/m K. Further, both bounds start to show a saturation of κ_{gr} near 400 K.

The blue line shown in Figure 5.6 is a curve of best fit using the three-phonon model described above. Due to the large number of free parameters in the model, obtaining a full non-linear regression of the data is problematic. Calculated fits are compared to the data in successive iterations, as the model phonon cut-off frequencies, Grüneisen parameters, and L are varied until the best fit is achieved as determined by inspection. In the range of temperatures shown, variation of parameters in a wide range for the ZA phonon mode made no apparent change in the shape or position of the curve. Comparing the value for γ_{ZA} from Figure 5.2, it is clear that it takes on very large negative values over the entire BZ, down to -80 near the Γ point (not shown in the figure). Comparing with Eq. (5.14), large values for γ_{ZA} diminish the contribution to the overall thermal conductivity. The values for the remaining phonon parameters were in reasonable agreement with those extracted from the DFT model calculations. The obtained model curve was greatly dependent on L , which for this fit had a value of 3.4 μm . This agrees with the notion that the phonon mode mean free path is to the dimensions of single crystal domain size for our CVD graphene samples.

5.3 *AFM Measurements*

The other alternative for measuring thermal conductivity of graphene utilizes atomic force microscopy (AFM). AFM can measure a variety of physical quantities on a nano-scale sample depending on the mode of operation (add-ons), with the basic function being to measure the sample topography. The AFM used for our measurements is a Park XE-100, with the standard topography mode, scanning thermal microscopy (SThM) mode, electron force microscopy (EFM) mode, and conductive AFM mode. Generally AFM measurement utilizes a cantilever (typically Si) with a fine tip (radius $\sim 10-100$ nm). With the cantilever mounted onto a probe head, there is three axis control using two decoupled sets of piezoelectric materials (piezos). One piezo controls the xy (horizontal, sample plane) motion of the cantilever, and another decoupled piezo controls the z (vertical) motion. By adjusting the voltage on either piezo, a horizontal area up to $\sim 50 \times 50 \mu\text{m}^2$ can be scanned, with a vertical resolution up to 0.01 nm. The precise position and vertical displacement is measured by

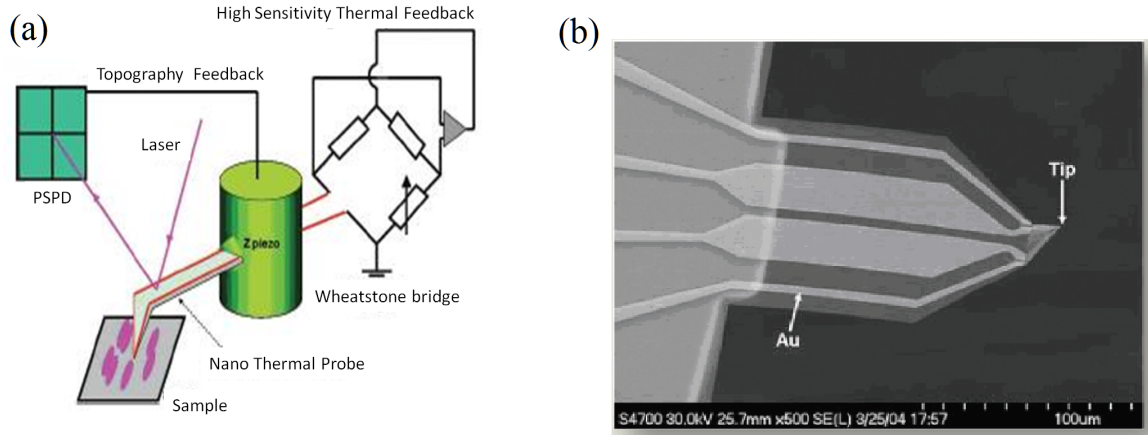


Figure 5.7: (a) Block diagram outlining the measurement setup for SThM mode (from Park website: www.parkafm.com). (b) SEM image of a microfabricated SThM cantilever and tip.

the deflection of a laser off the backside of the cantilever, using a photodiode.

The thermal measurements performed with the AFM utilize a special external setup, and custom tips shown in Figure 5.7. The custom nanofabricated SThM tip shown has four gold contact lines meeting at the tip, which is coated by a thin layer of Pd. This allows for the four-probe measurement of the resistance of the tip in contact with the sample surface. This resistance signal is sent to a Wheatstone bridge which is coupled to a feedback loop. Thus, the tip acts not only as a local heater, but can be used to measure the local sample temperature. In the temperature contrast microscopy (TCM) mode, a fixed current (power) is applied to the tip, and the fluctuations in sample temperature are recorded. In conductivity contrast microscopy (CCM) mode, a finite temperature is maintained by applying varying amounts of current to the tip. In this fashion, regions of higher thermal conductivity require a larger power to maintain the same rise in temperature as regions of lower thermal conductivity.

While a clear contrast in thermal conductivity is easily obtained with the SThM mode, extracting absolute quantitative values for κ is quite a technical challenge. Several methods for extracting κ have been proposed including: an AFM version of the 3ω technique [86], double-scanning [87], and a comparative method [88]. We attempted to use the comparative technique to make a nanometer resolution mapping of thermal conductivity of graphene samples. In this method, the material under test (graphene) must be in proximity with another material with a known thermal conductivity. We attempted this measurement with a sample of CVD graphene transferred onto a gold coated

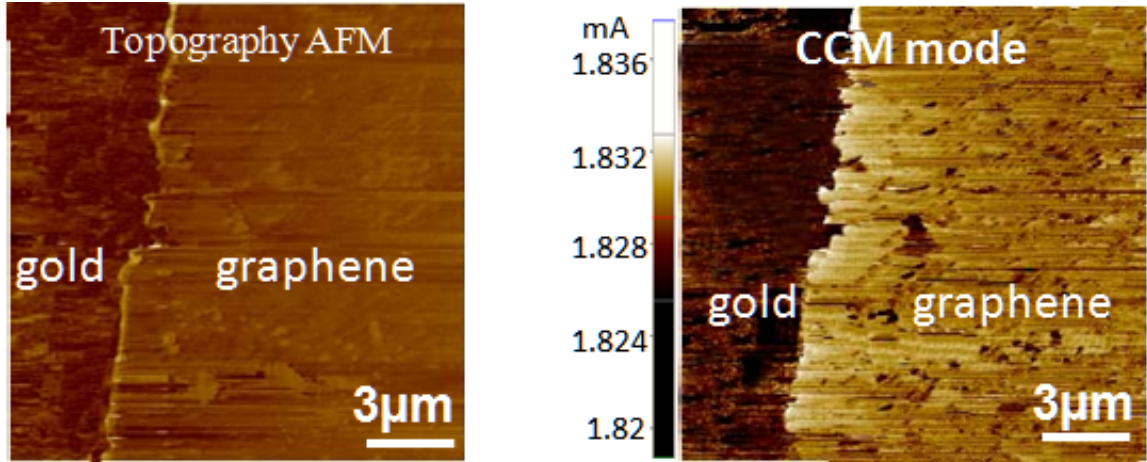


Figure 5.8: *Left:* AFM topographic mapping of CVD graphene on gold. *Right:* Thermal conductivity contrast mapping of the same region.

piece of Si wafer. The gold was pre-deposited onto the Si wafer using our standard technique of e-beam evaporation of Ti/Au (5 nm/ 50 nm thickness). Figure 5.8 shows both topographic and CCM mappings obtained with our AFM. This method is still being developed by our group, but does show some promise. A detailed description of the calculations shall not be given here, but initial computations show local values for κ_{gr} on our CVD samples in good agreement with the macroscopic measurement described above. The measurement was taken in ambient conditions, which allows for heat loss to the surroundings. But even these preliminary results are compatible with the room temperature values outlined above. When perfected, this type of measurement would be quite a powerful tool for measuring the local thermal conductivity of graphene.

We also performed several AFM studies using the various modes described above on a CVD graphene sample obtained from our collaborators at the University of Houston. The sample contains individual grains, and slightly merging single crystal grains from an abrupt CVD growth process described elsewhere [45]. The single crystal grains are transferred onto a Si/SiO₂ substrate, and are randomly located. We studied one chain of three grains that are barely merged into one another. Each crystal grain is monolayer graphene, which was independently verified with Raman spectroscopy (shown in Figure 3.13). Figure 5.9 shows the combined results from all of the AFM scans performed. The optical image, and topographic scan suggest that the three grains have partially merged into each other. The EFM image is a measurement of the voltage between the tip and

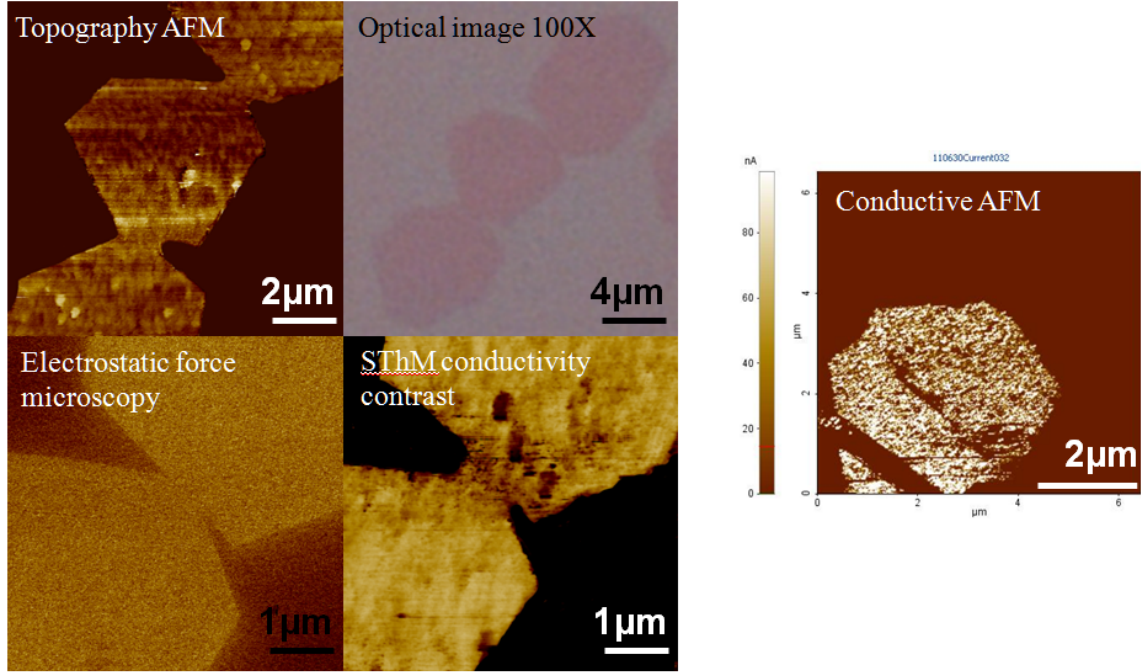


Figure 5.9: Various AFM measurements on the same chain of three single crystal grains of graphene on Si/SiO₂. The *top middle* image is an optical micrograph taken with the camera mounted on the AFM. All other images are labeled with their respective mode.

the sample, which is affected by bias applied to the tip, and the surface potential on the sample. The mapping of this surface potential appears uniform over the merged area, further indicating that the grains are connected graphene.

It has been claimed that the electrical and thermal conductivity of polycrystalline graphene films is dominated by size of the single crystal domains and the properties of the boundaries [89, 90]. This can be probed by thermal and conductive AFM modes. The SThM image shows that the individual crystal grains have mostly uniform and very similar thermal conductivity. There is however a clear drop in thermal conductivity at the junction where the two grains are merged. Further, we studied the electrical connection continuity of two merged grains. Using the standard electron beam lithography technique we placed a gold contact on one corner of the graphene grain at the bottom. This gold contact is connected to a large gold pad and to an external voltage source. For the conductive AFM measurement, the tip is grounded, and scans the sample in a contact mode so that it is physically in contact with surface. The measured signal is the current between the sample area and the tip. From the image, it is clear that the crystal gain in contact with the gold is at roughly the same potential,

while the other two grains that should appear in the upper right corner are absent (showing no current in the conductive mapping). Evidently, the merged boundary of the bottom two grains are slightly electrically insulated. STM and TEM studies have shown that the boundaries between grains show several crystal defects and fault lines where there is a crystal lattice mismatch [45, 91]. Further studies are needed to fully characterize these effects on the conductivity of large area polycrystalline graphene films.

5.4 Conclusion

We have made measurements of the thermal conductivity of CVD grown graphene. Using a comparison technique, we obtained temperature dependent data with measurement error far below any other measurements currently published. Furthermore, the measured thermal conductivity is in good agreement with a relatively simple theoretical model that is entirely explained by the phonon thermal conduction of graphene. By obtaining high quality CVD grown graphene samples, and avoiding chemical doping from microfabrication procedures we ensure this thermal conductivity is indeed the true material property graphene. Further studies would involve suspended graphene samples to reduce the effects of the substrate.

CHAPTER VI

PHOTOCONDUCTIVITY OF GRAPHENE IN HIGH MAGNETIC FIELDS

Due to its unique band structure, the quantum Hall effect (QHE) in graphene displays a rich variety of new physics. High electron mobility has been achieved in graphene, and remains nearly unchanged from low temperatures to room temperature. The integer QHE has been observed at room temperature [92], and the fractional quantum Hall effect (FQHE) has also been reported recently [93, 94]. Here we present the studies of the QHE in graphene monolayers, measured by differential photoconductive spectroscopy. In high magnetic fields a splitting of the four-fold Landau level (LL) degeneracy is observed. The sensitivity to infrared (IR) light used in this technique highlights the possibilities of optoelectronic devices and applications that could be met with graphene [95].

6.1 Theoretical Background

The Landau level spectrum of graphene was first calculated by McClure in 1956 [96], based on the low-energy Hamiltonian that is given by Eq. (2.24). When a magnetic field \mathbf{B} is applied perpendicular to the graphene plane, the Hamiltonian is modified by the standard replacement of the momentum $\mathbf{p} = \hbar\mathbf{q} \rightarrow \boldsymbol{\pi} \equiv \mathbf{p} + e\mathbf{A}$, where $\mathbf{A} = (-By, 0)$ is the vector potential (in the Landau gauge). Taking $\psi_{A,B}^K$ as the wavefunction near the K point, localized near the A or B site atoms in the unit cell, leads to a system of equations for the eigenenergies:

$$\begin{aligned} E\psi_A^K &= v_F(\pi_x - i\pi_y)\psi_B^K \\ E\psi_B^K &= v_F(\pi_x + i\pi_y)\psi_A^K. \end{aligned} \quad (6.1)$$

For the chosen gauge $[H, p_x] = 0$, the equations can be completely decoupled. Substituting one equation into the other gives after some simplification

$$\frac{1}{2m} \left(\frac{E^2}{v_F^2} + \hbar e B \right) \psi_A^K = \left[\frac{p_y^2}{2m} + \frac{1}{2} \tilde{k}(y - y_0)^2 \right] \psi_A^K, \quad (6.2)$$

where $y_0 = p_x/eB$, and $\tilde{k} = e^2 B^2/m$. The right side of this equation is simply the harmonic oscillator equation. This has eigenvalue solutions $\hbar\omega_c(n + \frac{1}{2})$, where $n = 0, 1, 2, \dots$, and $\omega_c = eB/m$ is the cyclotron frequency. This leads to both positive and negative roots for E , so that the eigenenergies can be written as

$$E_N = \text{sgn}(N) \sqrt{2e\hbar v_F^2 |N| B}, \quad (6.3)$$

where $N = 0, \pm 1, \pm 2, \dots$ is the LL index. The remarkable features of this energy spectrum are that the E_N is proportional to both \sqrt{N} and \sqrt{B} . In conventional two-dimensional electron gas (2DEG) systems, the LLs are directly proportional to N and B . Due to this interesting level structure, the spacing between levels is non-uniform. Furthermore, the energy gap between the $N = 0$ and $N = 1$ states can be quite large at high fields ($E_{0 \rightarrow 1} \approx 2800$ K for $B = 45$ T), which explains why the QHE can persist even at room temperature [92]. A visualization of the LLs in graphene is shown in Figure 6.1. The Gaussian line shape in the density of states is due to disorder broadening [97]. Note that these levels have the same valley degeneracy ($g_v = 2$) and spin degeneracy ($g_s = 2$) as the electrons in the zero field case, giving a total of four-fold degeneracy ($g = 4$). When the lifting of the LL degeneracy is considered, the filling factor ν is often used to label the sub-levels. The filling factor ν is defined in terms of the electron (hole) density n_s relative to the Dirac point

$$\nu = n_s \Phi_0 / B, \quad (6.4)$$

where $\Phi_0 = h/e$ is the magnetic flux quantum.

This LL structure gives rise to an interesting half-integer QHE in monolayer graphene. In a typical QHE experimental setup a current I is driven in the longitudinal direction (x -direction), and two voltages are measured: V_{xx} along the direction of current flow, and V_{xy} transverse to the current (Hall voltage). The corresponding magneto-resistance $R_{xx} = V_{xx}/I$, and Hall resistance $R_{xy} = V_{xy}/I$ can then be calculated. These resistance values depend on the sample geometry, and can be converted into geometrically-independent parameters. In the typical Hall bar geometry, with a conducting channel of length L and width W , the longitudinal resistivity is given by $\rho_{xx} = (W/L)R_{xx}$. And in a two-dimensional system $\rho_{xy} = R_{xy}$, but is typically given in units of Ω/\square . The Hall conductivity σ_{xy} can be determined from its relationship with the symmetric resistivity tensor

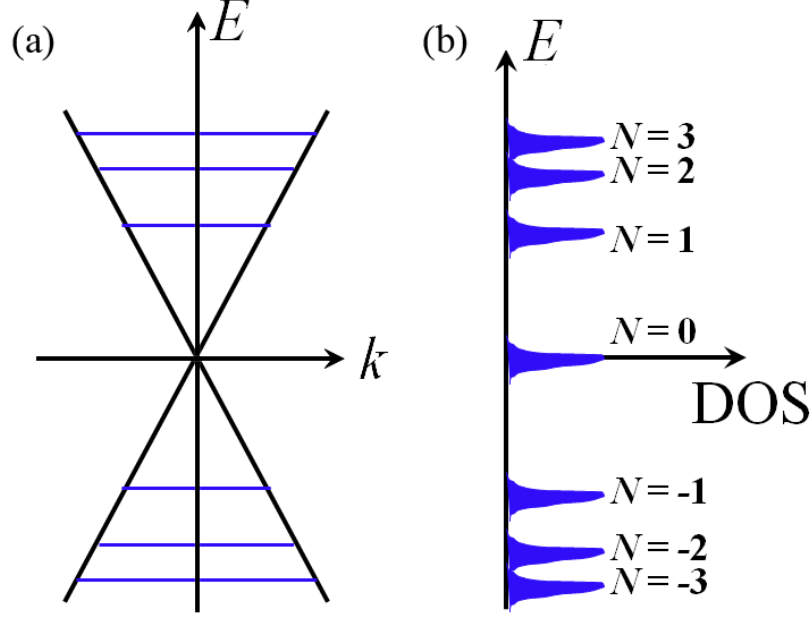


Figure 6.1: (a) Energy spectrum for quantized Landau levels. (b) Corresponding density of states for electrons in graphene in a magnetic field.

$\sigma = \rho^{-1}$ giving

$$\sigma_{xy} = \frac{-\rho_{xy}}{\rho_{xx}^2 + \rho_{xy}^2} = \frac{-R_{xy}}{W^2 R_{xx}^2 / L^2 + R_{xy}^2}. \quad (6.5)$$

In monolayer graphene this Hall conductivity exhibits sets of quantized plateaus, symmetric about the Dirac point ($\nu = 0$) [25]. In the low-field case, these plateaus take on the values [98]

$$\sigma_{xy} = \pm g \left(N + \frac{1}{2} \right) \frac{e^2}{h}. \quad (6.6)$$

This corresponds to plateaus at filling factors $\nu = \pm 2, \pm 6, \pm 10, \dots$. In the high-field limit, when the degeneracy of the $N = 0$ LL is fully lifted, new plateaus occur at $\nu = 0, \pm 1$. This splitting has previously been reported in transport experiments [99] up to $B = 45$ T, and the origin of the splitting is attributed to electron-electron interactions rather than bare Zeeman splitting [100]. Also at high fields, the $N = \pm 1$ LL undergoes degeneracy splitting to $\nu = \pm 4$ being attributed to the spin splitting. The splitting has been observed also by means of tunneling spectroscopy on epitaxial graphene [101], as well as on exfoliated graphene [102], while the exact nature of the splitting is still under debate [103, 104]. New measurement techniques are needed to study these intriguing QH states. Figure 6.2 shows the QHE in a monolayer graphene sample on hexagonal boron nitride (h-BN). The degeneracy splitting of the $N = 0, \pm 1$ LLs are readily seen. In each case a fully-developed

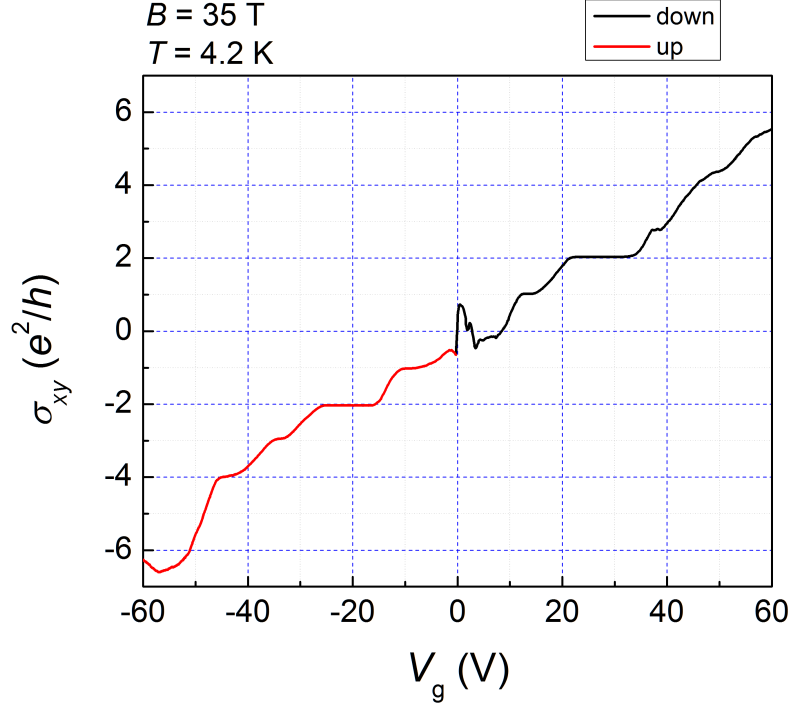


Figure 6.2: Quantized Hall conductivity for graphene in high magnetic field and low temperature. The red/black curves show measurements from the lowest/highest gate voltages swept in the given directions.

plateau in σ_{xy} corresponds to vanishing longitudinal resistivity ($\rho_{xx} = 0$).

The onset of the integer QHE requires high quality samples in terms of their mobility. A general condition is that $\mu B > 1$ [105, 93], requiring larger magnetic fields for lower mobility samples. Typical mobilities for supported graphene samples range from $\mu \sim 2,000 - 25,000 \text{ cm}^2/\text{V s}$. The integer QHE has even been observed in CVD grown graphene ($\mu \sim 3,000 \text{ cm}^2/\text{V s}$) at 18 T [61]. Several groups have used suspended graphene to obtain much higher mobilities, which after current annealing can exceed $\mu \sim 200,000 \text{ cm}^2/\text{V s}$ [105]. In fact, the fractional QHE has been observed in a suspended graphene sample [94], which involves many-body correlations that are sensitive to impurity scattering. The other means of obtaining high mobility ($\mu \sim 100,000 \text{ cm}^2/\text{V s}$) is by placing graphene samples onto a h-BN substrate [11]. In fact, the fractional QHE has recently been observed in these samples as well [106].

At experimentally accessible magnetic fields, the LL spacing of graphene lies within the infrared (IR) spectrum. Using broad band IR absorption spectroscopy, the inter-band and intra-band

transitions between LLs can be probed. These transitions are subject to the dipole transition selection rule $\Delta N = |N_2| - |N_1| = \pm 1$ [107]. Studies on both exfoliated graphene [108] and epitaxial graphene [109] observed several of these transitions with the $-1 \rightarrow 0$ ($0 \rightarrow 1$) LL transitions showing the most intriguing physics [110]. These transitions are indistinguishable with unpolarized light, but can be independently measured using circularly polarized light. To the best of my knowledge, studying LL transitions using polarized light sources is still lacking.

In the absence of a magnetic field, graphene still shows a rich variety of response to light in the IR range. These effects include: interband photoexcitations, generation/recombination processes, intraband quasielastic scattering on acoustic phonons, and scattering due to static disorder [111]. In particular, Vasko, et al. have modeled the photoconductivity of graphene in the context of photoexcited carrier population. In the mid-IR regime, this photoresponse is heavily dependent on the incident radiation power, temperature, and frequency. For light with excitation energy $\hbar\omega = 120$ meV, at liquid helium temperature ($T = 4.2$ K), the increase in carrier concentration is $\gtrsim 10^9 \text{ cm}^{-2}$, and the increase in conductivity is $\sim 2\%$. These effects lead to a photoexcited current I_{ph} , and changes in sample resistance due to radiative heating and shifts in the chemical potential. This forms the basis for the differential photoconductivity spectroscopy method employed for this work.

Gate-voltage tunable IR transmissions have been observed in exfoliated samples in zero field. Resonant IR absorption provides a method for opto-electronic sensing in graphene. The relative change in reflectivity $\delta\mathcal{R}/\mathcal{R}$ is proportional to the optical conductivity $\sigma(\omega)$:

$$-\frac{\delta\mathcal{R}}{\mathcal{R}} = \frac{1}{c} \text{Re } \eta \cdot \sigma(\omega), \quad (6.7)$$

where c is the speed of light, and η is a dimensionless factor that depends on the refractive indices of the substrate [112]. Some groups have exploited this effect to sense changes in $I - V$ characteristics with IR light [60, 113], and as a compliment to currently used HgCdTe (MCT) IR detectors [114].

6.2 *Experimental Methods*

Photoconductivity spectroscopy has been shown to be a powerful method for exploring the LL structure in graphene [23]. The previous measurement observed strong cyclotron resonance, and demonstrated an asymmetry in the electron and hole velocities. Also, conventional two-dimensional

electronic systems must satisfy Kohn's theorem, where the cyclotron resonance is completely independent of many-body electron interactions [115]. Due to the unique linear bandstructure of graphene, this theorem is thought not to apply. Recently developed graphene on h-BN samples with very high mobilities and the availability of high magnetic fields ($B \leq 45$ T) have made the observation of LL states splitting possible. These high quality graphene samples allow for studying the applicability of Kohn's theorem for systems with linear band structure. A special double modulation technique allows for unambiguous measurement of the photo-response of graphene to IR light.

6.2.1 Graphene on h-BN

The graphene samples used for these measurements were obtained from a group at Columbia University. The general procedure for fabricating these devices is discussed elsewhere [11]; this section gives a brief outline of their process. Hexagonal boron nitride has a honeycomb structure similar to graphene, with alternating boron and nitrogen atoms. There is a small lattice mismatch between h-BN and graphene of about 1.7%, and h-BN is insulating due to its large bandgap (4.97 eV). It has a large breakdown voltage (0.7 V nm^{-1}) compared to SiO_2 , and is atomically flat, with a surface roughness better than 0.5 nm. Most importantly, monolayer graphene samples on h-BN have very high mobilities as previously mentioned.

Starting with thick single crystals of h-BN, and using the mechanical exfoliation technique thin h-BN layers are pressed onto an oxidized silicon wafer which serves as the final sample substrate. Another wafer is coated with a proprietary water-soluble layer and PMMA with appropriate thickness so that monolayer graphene can appear visible under a microscope. Flakes of graphene are exfoliated onto this sacrificial wafer, identified under a microscope, and then measured for film thickness using Raman spectroscopy. This graphene coated wafer is then placed in DI water leaving graphene coated PMMA floating. The graphene is then fished out onto a glass slide. Using a micromanipulator, the graphene flake can be carefully aligned and pressed onto the h-BN flake on the final substrate and heated to 110°C to drive out any water. Electrical leads are placed onto the graphene flake using the standard electron beam lithography procedure. Finally, the samples are annealed in forming gas at 340°C for 3.5 hours to remove any residual resist. The final fabricated samples are placed onto a dual-inline package (DIP) and wires are bonded to the electrical leads and

to the silicon back side for the application of a gate voltage.

6.2.2 Optical Measurement Setup

This section describes the photoconductivity technique used to observe the LL spectrum of graphene in a magnetic field. The following experiments were performed at the National High Magnetic Field Laboratory in Tallahassee, FL. This lab houses the world’s strongest continuous field hybrid magnet (45 T), as well as several other high field resistive magnets (35 T) and superconducting magnets (17.5 T). We made photoconductivity measurements of several samples in both the superconducting and resistive magnet, making this work the first “high-field” photoconductivity measurement ever performed.

An overview of the basic experimental setup is shown in Figure 6.3 (a). A monolayer graphene sample is loaded at the end of a vacuum sealed probe, with electrical wiring connecting the sample leads to the top of the probe which remains at room temperature. A diamond window is fixed at the top of the probe, which allows for nearly full transmission over a wide range of incident light wavelengths. The probe is pumped out with a turbo molecular pump to $\sim 10^{-5}$ Torr, and then backfilled with helium gas for use as heat exchange gas. The probe is loaded into a Janis liquid helium cryostat at the center of the bore of the magnet. The magnet provides a variable field in the direction perpendicular to the plane of the graphene sample.

The optical source used was a (1.2 W) CO₂ laser, with a temperature tunable wavelength $\lambda = 10.6 \pm 0.1 \mu\text{m}$. For all measurements, we used the center value, allowing enough time after turning on the laser power to reach full thermal equilibrium (constant λ). A chopper is placed in front of the laser beam on an optical table, which is controlled by a variable frequency controller that has a TTL output for use as a reference signal. The frequency ω_{ch} that the copper actually blocks/allows the laser light is measured by a photodiode mounted on the chopper. The phase of the chopper reference and the laser are carefully matched using a MCT photodiode, comparing their signals on an oscilloscope as the chopper is moved slightly around the path of the laser beam. The laser beam is reflected off a mirror through a wire grid (ZnSe) linear polarizer, and then to the probe/sample. Since the light beam is already linearly polarized as it exits the laser cavity, the polarizer allows for tuning of the laser intensity by rotating the direction of polarization.

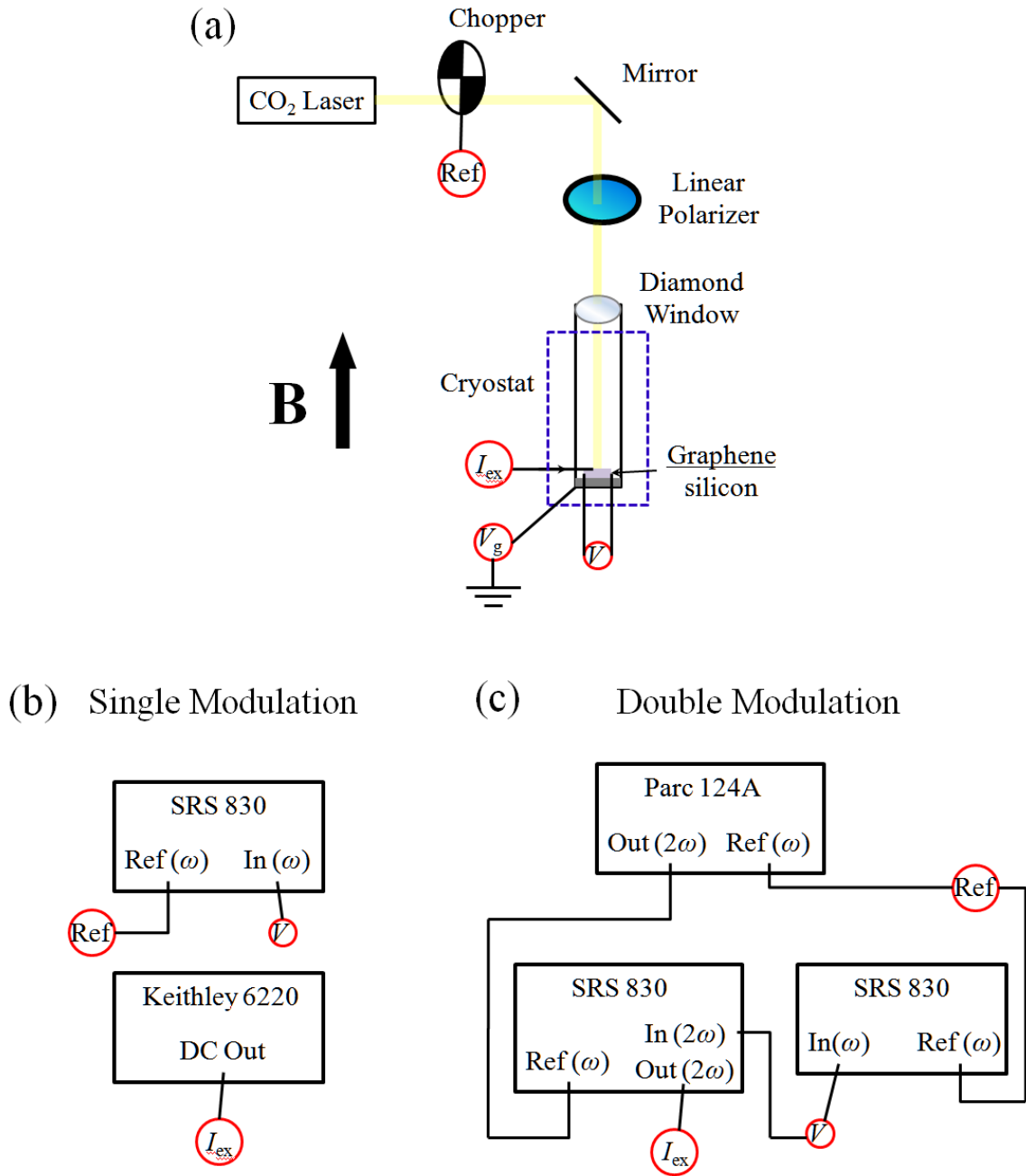


Figure 6.3: (a) Photograph of linear polarizer and aperture for laser conditioning and alignment. (b) Infrared photograph of the same setup. (c) Infrared photograph of the same setup with the laser beam on.

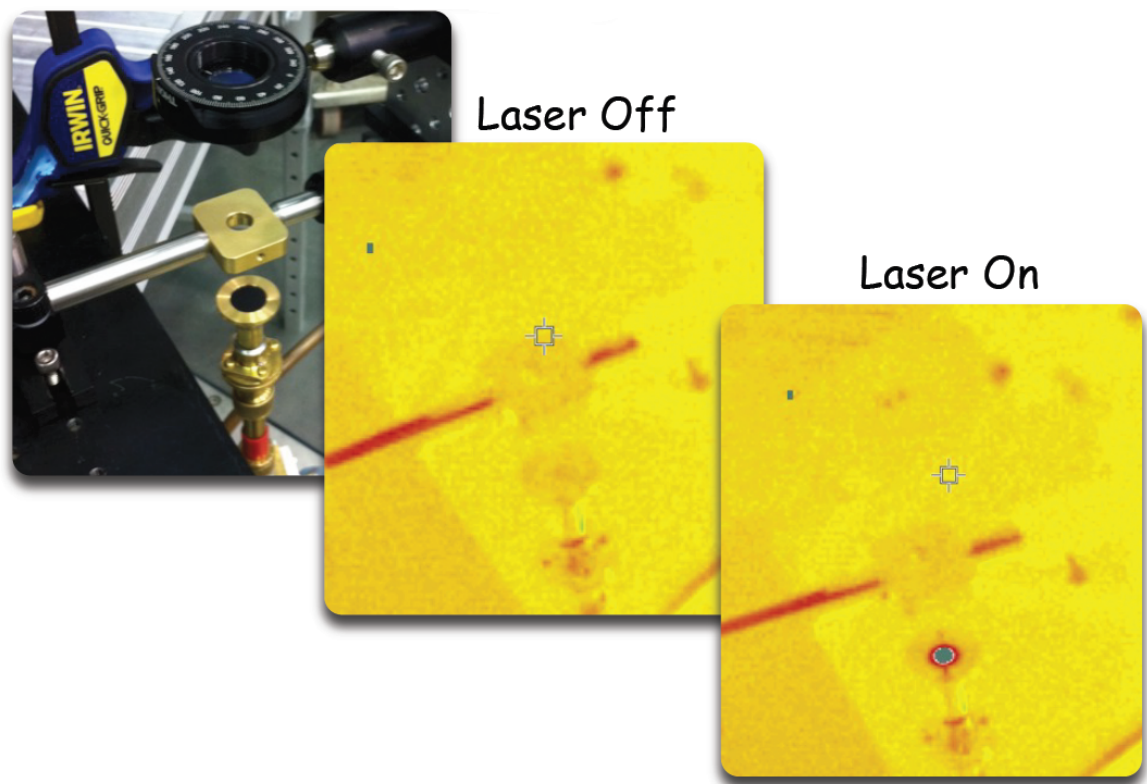


Figure 6.4: (a) Optical setup for the photoconductivity measurement. Measurement schemes for (b) single modulation, and (c) double modulation.

All of the optical elements are carefully aligned so that the beam passes as close to the center of the probe as possible. This is to avoid the beam scattering off the brass walls of the probe which can destroy the beam's phase coherence and the polarization. Figure 6.4 illustrates the procedure used to align the beam. Using a Fluke Infrared thermal imaging camera, the beam position can be determined by blocking the path with an absorbing material. We placed a small piece of rubber over the top of the probe to block the beam, and the camera picks up the heat signature from where the laser hits it.

6.2.3 Modulation Technique for Photoconductivity

The transport measurements of sample resistance R taken use phase-locked detection. In the standard technique, an alternating excitation current $I_{\text{ex}} \sin(\omega t)$ is applied to a sample, and the voltage response is measured at the same modulation frequency ω . Using a lock-in amplifier, this measured signal is multiplied by an internal reference signal, then filtered, and averaged over one period. The lock-in allows for simultaneous measurement of the in-phase (X), and out-of-phase (Y) signals. These X and Y signals are given, respectively, by the following (using the notation $x = \omega t$)

$$\frac{1}{2\pi} \int_0^{2\pi} I_{\text{ex}} R \sin x \sin x \, dx = \frac{1}{2} I_{\text{ex}} R \quad (6.8)$$

$$\frac{1}{2\pi} \int_0^{2\pi} I_{\text{ex}} R \sin x \cos x \, dx = 0, \quad (6.9)$$

assuming the sample has no reactive component causing a phase shift. This technique has an improved signal/noise ratio due to the measurement being taken in a narrow band around the excitation frequency.

For a differential photoconductivity measurement, this technique is altered by the introduction of light. The light creates a change in the sample resistance δR , and the lock-in can detect this photoresponse. We measured samples using two techniques: “single modulation,” and “double-modulation.” Their measurement schemes are illustrated in Figure 6.3 (b) and (c), respectively. For a single-modulation measurement, a direct current I_{dc} is applied through two leads on the graphene sample, and the light hits the sample at the chopped frequency. This leads to a total sample resistance

R_{tot} that varies as a square wave as

$$R_{\text{tot}} = R + \delta R \text{sq}(x), \quad (6.10)$$

where $\text{sq}(x)$ is a square wave defined as

$$\text{sq}(x) = \begin{cases} 1, & 0 < x < \pi; \\ 0, & \pi < x < 2\pi. \end{cases} \quad (6.11)$$

Furthermore, the introduction of the light induces a photocurrent I_{ph} at the chopper frequency which adds to the applied direct current giving a total sample current

$$I_{\text{tot}} = I_{\text{dc}} + I_{\text{ph}} \text{sq}(x). \quad (6.12)$$

The (longitudinal) photoresponse δV is measured at the chopper reference frequency $\omega = \omega_{\text{ch}}$, with the respective X and Y components given by the following

$$\frac{1}{2\pi} \int_0^{2\pi} I_{\text{tot}} R_{\text{tot}} \sin x \, dx = \frac{1}{\pi} I_{\text{dc}} \delta R + \frac{1}{\pi} I_{\text{ph}} (R + \delta R) \quad (6.13)$$

$$\frac{1}{2\pi} \int_0^{2\pi} I_{\text{tot}} R_{\text{tot}} \cos x \, dx = 0. \quad (6.14)$$

A problem arises with taking measurements in this fashion, as is evident from Eq. (6.13). There is mixing between the normal sample resistance and the photoconductivity that we are interested in.

A clever technique that avoids this problem, and fully separates out a component that only depends on the photoconductivity, is double-modulation. In this case, the excitation current applied to the sample is driven at twice the chopper frequency ($2\omega_{\text{ch}}$), and the photoresponse is measured at $\omega = \omega_{\text{ch}}$. Actually performing this measurement required three separate lock-in amplifiers: two SRS 830 digital lock-in amplifiers, and one EG&G Par 124A analog lock-in amplifier. The Par amplifier has a unique feature to create an output at twice the reference input frequency, which acted as the excitation current. One possible issue could be that this method introduces a small ($< 10^\circ$) phase shift ϕ to the excitation current, relative to the chopper's reference signal. For this situation, the total current reaching the sample is

$$I_{\text{tot}} = I_{\text{ex}} \sin(2x + \phi) + I_{\text{ph}} \text{sq}(x). \quad (6.15)$$

The respective components of the photoresponse are

$$\frac{1}{2\pi} \int_0^{2\pi} I_{\text{tot}} R_{\text{tot}} \sin x \, dx = \frac{1}{3\pi} I_{\text{ex}} \delta R \sin \phi + \frac{1}{\pi} I_{\text{ph}} (R + \delta R) \quad (6.16)$$

$$\frac{1}{2\pi} \int_0^{2\pi} I_{\text{tot}} R_{\text{tot}} \cos x \, dx = \frac{1}{3\pi} I_{\text{ex}} \delta R \cos \phi. \quad (6.17)$$

From these expressions, it is evident why this method is so useful. The out-of-phase component is now entirely the photoconductivity response, with no mixing whatsoever.

Finally, we performed a concurrent measurement of the longitudinal and transverse voltages in this same double modulation technique. For these voltage responses, we used additional lock-in amplifiers to measure at the same double modulated frequency $\omega = \omega_{\text{ch}}$. In this setup, the respective measured components are as follows:

$$\frac{1}{2\pi} \int_0^{2\pi} I_{\text{tot}} R_{\text{tot}} \sin 2x \, dx = \frac{1}{2} I_{\text{ex}} \left(R + \frac{1}{2} \delta R \right) \cos \phi + \frac{1}{2\pi} I_{\text{ph}} (R + \delta R) \quad (6.18)$$

$$\frac{1}{2\pi} \int_0^{2\pi} I_{\text{tot}} R_{\text{tot}} \cos 2x \, dx = \frac{1}{2} I_{\text{ex}} \left(R + \frac{1}{2} \delta R \right) \sin \phi. \quad (6.19)$$

In this case, the R could represent R_{xx} or R_{xy} depending on the contact orientation. Looking at the real component, we can make a comparison of the relative magnitude of the terms. As will be seen in the next section, the magnitude of δR is on the order of 1000 times smaller than the actual sample resistance R . Furthermore, the photocurrent I_{ph} is significantly smaller compared to the applied excitation current ($I_{\text{ph}} \ll I_{\text{ex}}$). So to a good approximation, the real component of the measurement at frequency $2\omega_{\text{ch}}$ is $\sim \frac{1}{2} I_{\text{ex}} R$. This is the same expression obtained for the normal transport measurement method described at the beginning of the section. This allows for comparison of the photoresponse to the normal transport response without the need for collecting data from two separate measurements.

6.3 Results & Discussion

As a first study of photoconductivity, we made measurements of graphene on h-BN using a 17.5 T superconducting magnet. For this sample, we used the single modulation technique, with a chopper frequency $\omega_{\text{ch}} \sim 100$ Hz. In this measurement scheme, we collected data for photoconductivity

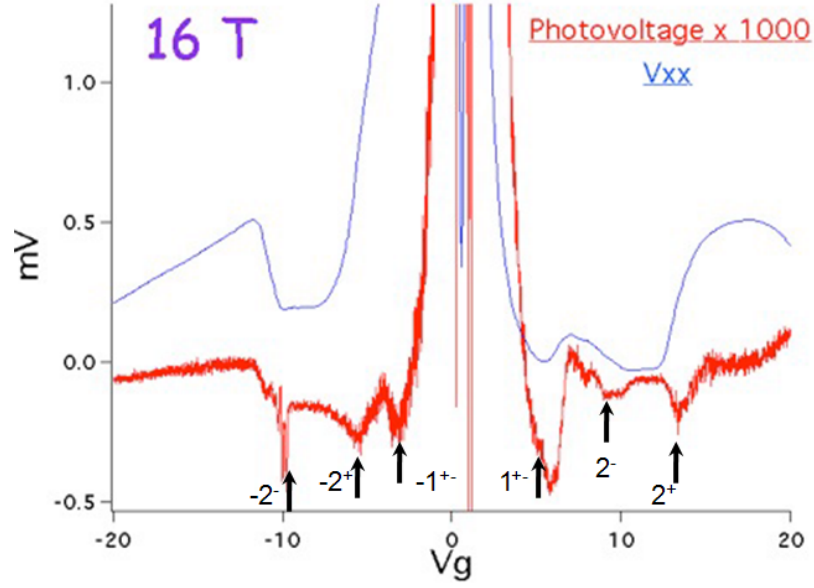


Figure 6.5: Measured photoresponse and longitudinal voltage for graphene in a magnetic field. The photoconductivity features appear at the edge of the QH states as labeled.

and normal transport in separate runs at the same corresponding magnetic fields. For the photoconductivity measurements, we utilized the setup illustrated in Figure 6.3 (b). Figure 6.5 shows the combined results from two measurements taken at liquid helium temperature, and $B = 16$ T. The blue curve shows a fully developed QH state for the $\nu = +2$ state, where $V_{xx} \approx 0$. This curve also shows the development of the $\nu = -2$ state with $V_{xx} \approx 0.2$ mV, and the partial development of the $\nu = +1$ state. The red curve represents the (scaled 1000 \times) photovoltage curve. This curve clearly shows similar overall structure to the V_{xx} curve, which is as expected from the above discussion on single modulation. There are additional peaks and dips that appear near the edges of the QH states seen in the V_{xx} curve, but their interpretation is masked by the mixing of the photoresponse with the transport response.

Figure 6.6 shows the collection of photoresponse curves taken at various magnetic fields from 0 T to 17.5 T. This two-dimensional contour map plots the photovoltage intensity by the color scale shown. There is a structure of changes in intensity that tracks linearly with the applied gate voltage, as expected from Eq. (6.4) since $n_s \propto V_g$. The white lines drawn on the figure correspond to the gate voltages at the middle of each QH plateau, obtained from the V_{xx} transport data. Each line meets at zero field at the gate voltage corresponding to the Dirac point. The peaks in intensity of

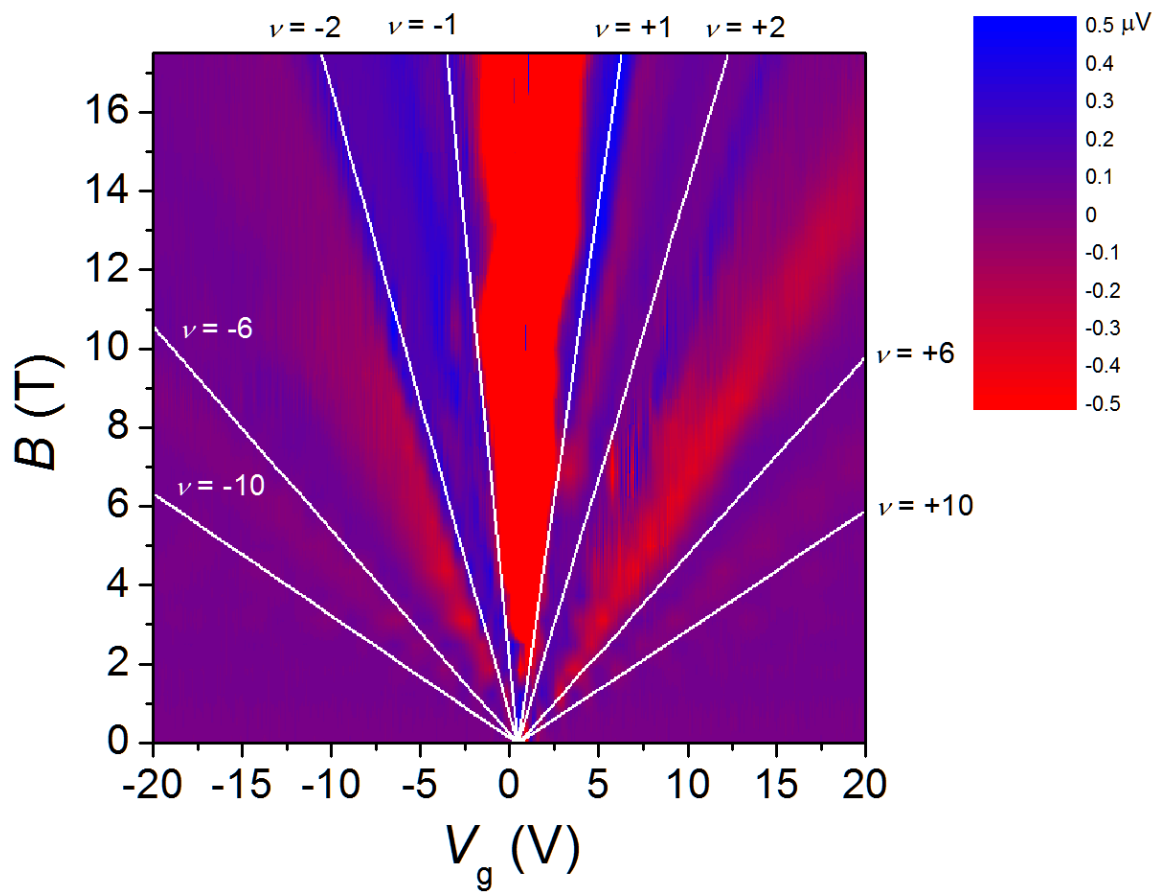


Figure 6.6: Contour map showing the photoresponse as a function of magnetic field and gate voltage.

the photovoltage correspond very well with the $\nu = \pm 1, \pm 2$ states, but again, this correspondence is plagued by the problem of mixing in the photovoltage data. Comparing the various QH states seen in the transport and photoconductivity data, there is an apparent asymmetry in their gate voltage dependence up to 6%, for example, comparing the slope of the +2 and -2 states.

To obtain a clear photoconductivity response, we performed measurements using the double modulation technique. We measured several samples of monolayer graphene on h-BN in a resistive magnet that provides fields up to 35 T, and with a chopper frequency $\omega_{\text{ch}} \sim 75$ Hz. We utilized the measurement setup outlined in Figure 6.3 (c). As described in the previous section, we took measurements of photoconductivity at the chopper frequency ω_{ch} , and concurrent measurements of V_{xx} and V_{xy} at $\omega = 2\omega_{\text{ch}}$ using two separate SRS 830 lock-in amplifiers. We also took normal transport measurements using the standard technique to confirm the full development of the QH states at the highest available field. The Hall conductivity for this measurement was presented in Figure 6.2. From this data, we can see well developed Hall plateaus for the $\nu = \pm 1, \pm 2$ states. The following photoconductivity study focuses mainly on these states. Note that the two curves shown differ in the direction that the gate voltage was swept. Due to hysteresis (because of gate-dependent charge trapping), some of the features for one sweep direction appear better developed than the corresponding feature for sweeping in the opposite manner. To this end, when measuring photoconductivity two separate measurements were taken for both positive and negative values of gate voltage.

Figure 6.7 shows the combined measurements of V_{xx} , V_{xy} and the photoresponse (labeled V_{pc} in the figure) at the highest available field. Note that the photoresponse is scaled by a factor of 500, so that its variations ($\sim \mu\text{V}$) appear visible in relation to the other two curves. The two transport curves clearly show the presence of the $\nu = +1, +2$ QH states. For each QH state, the Hall voltage reaches a constant plateau value in exactly the same gate voltage ranges where the longitudinal voltage almost vanishes. As discussed, with transport data measured at the double modulation frequency, there is a small contribution from the photocurrent and photoconductance. This effect is barely visible on the graph at this scale. The minimum longitudinal voltage is ≈ 0.02 mV for the $\nu = +1$ state, and ≈ 0.004 mV for the $\nu = +2$ state. Unfortunately, there is no simple means to extract I_{ph} from this data. The most important features to notice are the peaks in the photoresponse near the

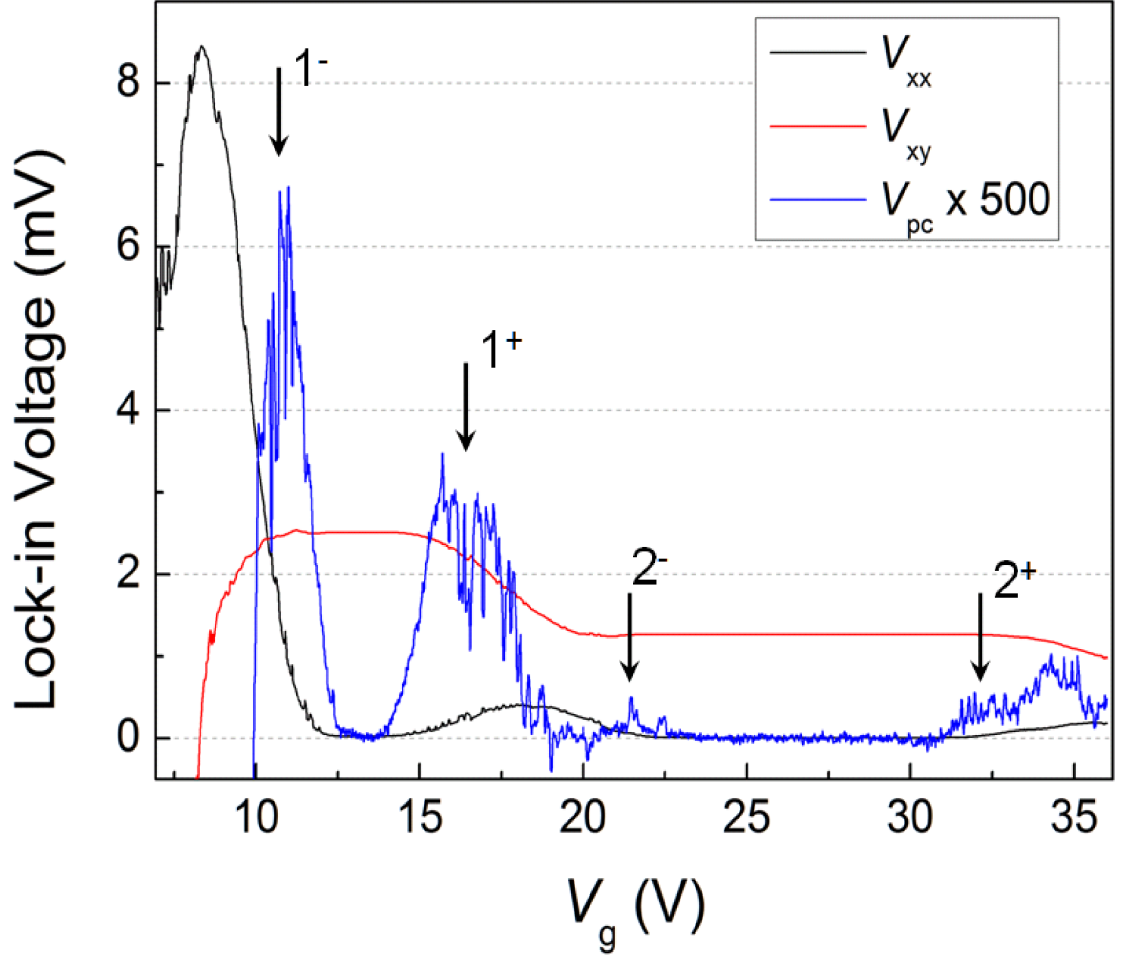


Figure 6.7: Lock-in response of the longitudinal voltage (black curve), and the Hall voltage (red curve) measured at frequency $\omega = 2\omega_{\text{ch}}$. Photoresponse (blue curve) measured at frequency ω_{ch} (scaled by 500 \times). Measurement taken at $T = 4.2$ K, and $B = 35$ T, with an excitation frequency $\omega = 2\omega_{\text{ch}}$.

edge of the QH states. These peaks are primarily due to the change in resistance δR from the slight heating caused by the IR light. The edges of the QH states present the largest change in sample resistance from nearly zero to finite values. For this measurement, there are two large peaks in the photoresponse near the edges of the $\nu = +1$ state (labeled 1^+ and 1^-), two other smaller peaks near the edges of the $\nu = +2$ state (labeled by 2^+ and 2^-), and some other peaks appearing at the highest gate voltages.

To track the field dependence, photoconductance spectra were taken at every odd integer value for magnetic field from 1 T to 35 T. These data are presented in Figure 6.8. The curves are offset vertically for clarity, and are measured over increasing ranges of gate voltage to allow for tracking

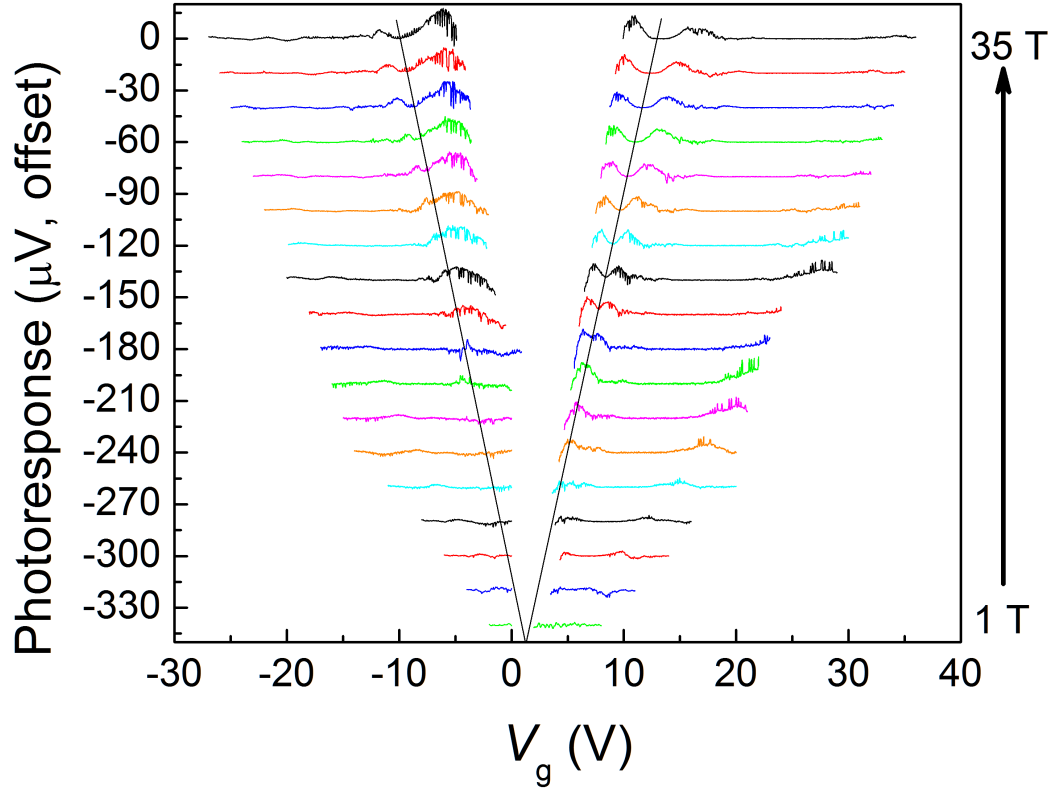


Figure 6.8: Photoresponse of monolayer graphene on h-BN at odd integer values of magnetic field between 1 T and 35 T. The black lines are visual guides tracking the $\nu = \pm 1$ QH states.

QH features as a function of magnetic field. The main features tracked are the two peaks in photoconductivity around both the $\nu = \pm 1$ states. The actual QH states occur at the minima between these peaks. These features show a clear linear dependence on the magnetic field and gate voltage as expected. Note that the peaks in photoconductivity for the $\nu = +1$ state persist down to $B = 17$ T, are completely merged at $B = 15$ T, and disappear by $B = 9$ T. For the $\nu = -1$ state, these changes occur at much higher fields, with the evidence for this state vanishing at $B = 13$ T. We again see the apparent asymmetry between electron and hole states previously noted in the single modulation results. In addition, there is the ubiquitous presence of noise fluctuations in the photoconductivity data, especially near the peaks in the response. The source of these fluctuations is unclear. This noise is present in almost all of photoconductivity data taken, and more probably is due to some physical process rather than electrical noise from the measurement setup.

6.4 Conclusion

These measurements show great ability for identifying QH states in graphene that aren't necessarily clear in the Hall conductivity data. Small features in Hall conductivity are amplified by this differential method in photoconductivity. In fact, the $\nu = \pm 1$ QH states were observed in the photoconductivity response. The observed response is mainly due to laser induced sample resistance changes, but there is also a resonant contribution due to the LL transition that matches the IR laser energy. This effect has been studied in previous photoconductivity measurements in lower mobility samples and lower magnetic fields[11]. Due to the high quality of graphene samples on BN, the temperature dependence due to laser heating is much more pronounced. The resonant contribution can be identified in further experiments by the use of circularly polarized light, which can filter the two allowed LL transitions by the corresponding angular momentum change, while the left and right circularly polarized light will cause the same amount of heating. Also, by decreasing the background sample temperature to below 1 K, the effect would be enhanced with an improved signal to noise ratio. These improved techniques will be utilized in future work.

CHAPTER VII

CONCLUSION

The work presented in this thesis deals with the growth and characterization of graphene obtained by mechanical exfoliation and by chemical vapor deposition on metal substrates. Having developed a method for reliably producing large area monolayer graphene samples has enabled characterization of thermal and electrical properties by novel means not available to smaller exfoliated samples. Most importantly, the electrical measurements of TEP and thermal conductivity exploited micro thermocouples, which can be attached to samples without the requirements of chemical processing.

The TEP of CVD grown graphene was measured for large area samples in various environments from vacuum/temperature annealed to gaseous and liquid surroundings. Measuring both the resistance and the TEP of a graphene sample shows that graphene is very especially sensitive to its environment due to the fact that the entire sample is a surface. We have clearly seen the interaction of charge transfer to and from graphene to its surroundings and its substrate. In fact, the monotonic crossover of the sign of TEP for graphene during annealing allows unambiguous detection of environmental changes compared to the typical electrical resistance change detection. We have exploited this interaction, and show that a single graphene sample can repeatedly be used by cycling between exposure and thermal annealing. By comparing environments and substrates this sensitivity is proposed to be exploited for various sensing applications. The measurements presented here serve as a proof of principle for graphene sensors, but much work remains on creating sensing that can differentiate between differing concentrations and mixtures of gases and or liquids.

Graphene is also remarkable in the fact that its thermal conductivity is among the highest of all known materials, ~ 1700 W/m K at room temperature for our CVD grown samples. By producing large area samples that aren't contaminated by chemical processes, we have probed the intrinsic thermal conductivity of substrate supported CVD grown graphene. Our novel electrical measurement technique gives strict upper and lower bounds for the temperature dependent thermal conductivity. Furthermore, the measured values for thermal conductivity are far more accurate than

those obtained from the current optical and electrical measurements which have errors on the order of several tens of percent. In fact, the data presented here are well modeled by the phonon interactions in graphene. Further measurements on higher quality graphene samples and also suspended graphene samples could refine the accuracy of the thermal conductivity obtained. If future work can obtain this higher accuracy, more intricate models accounting for the substrate and various scattering mechanisms present in graphene could be developed to describe the relative magnitude of these effects for thermal transport in graphene.

Finally, we have shown the strong interaction of infrared light and high quality exfoliated graphene samples. By transferring graphene to substrates of hexagonal BN the highest achievable electron mobilities for graphene have been observed. Due to this high mobility, the photo-voltage across the graphene due to laser excitations allows for observation of fully split Landau level degeneracy. Using the clever double modulation technique we have tracked the $\nu = \pm 1$ LLs in high magnetic fields. Observation of these LLs shows the sensitivity of light to many body interaction induced LL splitting. Since Kohn's theorem is not valid in graphene due to its linear band structure, our infrared photoconductivity measurement opens the possibility of using cyclotron resonance to study many body effects in graphene. Further experiments utilizing circularly polarized light and possibly higher field/temperature ratios could serve to improve the measurement technique and sensitivity.

APPENDIX A

TECHNIQUES FOR GRAPHENE SAMPLE PRODUCTION

A.1 Sample Fabrication

The method for producing the different types of samples used for my experiments follows the same basic outline.

1. Substrate Preparation
2. Collection of graphene flakes
3. Device patterning
4. Oxygen plasma etching
5. Patterning of contacts
6. Metal deposition
7. Wire bonding and packaging

A.1.1 Substrate Preparation

The substrates used for all devices are 4 inch diameter (100), highly doped, silicon wafers obtained from the MEMS exchange. The wafers come with a thermally grown, 300 nm thick native oxide layer. This oxide layer makes the wafers appear violet to purple in color under normal white light. Using a diamond scribe the wafers are scratched along the crystal axes so that they easily cleave under slight pressure. The wafer is then diced into square chips roughly $1 \times 1 \text{ cm}^2$ in size.

The wafers are cleaned to remove any organic and inorganic impurities present. First, the chips are given a general cleaning in acetone and isopropanol (IPA) solvents. The chips are placed in a beaker filled with acetone and placed in an ultrasonic cleaner for 5 minutes. The chips are then transferred (while remaining wet) into a beaker of IPA. The chips are ultrasonically cleaned for 5

minutes and then rinsed with deionized (DI) water. The chips are then dipped into another beaker of IPA and then blown dry with N₂ gas. This process removes inorganic and some organic impurities.

To fully remove any organic impurities, the wafer chips are then cleaned using a Piranha etch. The solution is prepared in a Pyrex glass dish as follows. 300 mL of sulfuric acid (H₂SO₄ 96%) is poured into the dish and heated to 130°C on a hot plate. Once the acid is at the correct temperature, 100 mL of hydrogen peroxide (H₂O₂ 30%) is added; this starts a violent reaction. The wafer chips are then placed in the piranha solution using teflon (PTFE) tweezers. After the reaction subsides, the chips are removed from the solution and rinsed in DI water. They are then dipped in IPA and blown dry with N₂ gas.

The previous steps involve several wet chemical processes. The substrate needs to be as dry as possible for the best adhesion of graphene to the substrate surface. To remove any residual water or other solvents, the cleaned wafer chips are placed on a hotplate (at 180°C) for 10 minutes. Finally, the chips are ready for further processing.

A.1.2 Collection of Graphene Flakes

Most commonly we use either mechanical exfoliation of graphene from kish graphite, or the CVD deposition method to obtain graphene. Both of these processes were described in Chapter 3. In either case, flakes/sheets of graphene are left deposited on the surface of a substrate. For the Si/SiO₂ substrate, the flakes are visible under an optical microscope. Otherwise, there must be knowledge of the approximate location of the graphene. For all substrates, the nature of the graphene samples is characterized using Raman spectroscopy to determine layer thickness and overall uniformity.

A.1.3 Device Patterning

A graphene device is, put simply, a sample of graphene (often patterned into particular shapes) that has metal contact lines for making electrical connection to external voltage sources and sensors. The patterning of the shape of the graphene sample, and the placement of the metal contacts is performed by electron beam lithography. A scanning electron microscope allows not only for imaging of samples, but can be used to expose electron sensitive chemical resists in a manner analogous to light exposing photographic film. We use the electron beam resist polymethyl methacrylate (PMMA), which acts as a positive resist. This means whatever areas that are exposed to the electron beam will

950PMMA A Resists Solids: 2% - 7% in Anisole

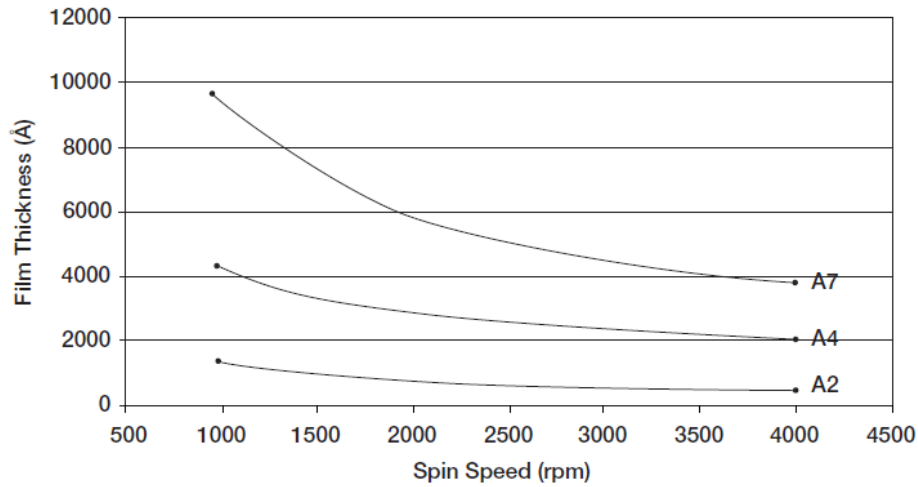


Figure A.1: Final thickness of spin coated PMMA versus angular speed. The graph shows three concentrations (% anisole) of the solvent. Taken from the Microchem data sheet.

be dissolved and removed in the development step, leaving the sample exposed in those areas. The remaining unexposed areas remain covered by PMMA until removed by chemical strippers such as acetone.

A pattern is designed on the computer aided design software DesignCAD LT 2000. Individual elements that will become exposed are patterned using polylines to complete an enclosed area. Since the pattern usually involves more than one exposure step, the first pattern drawn is rectangular array of alignment marks (small + signs). These alignment marks allow for accurate registration between patterns. The following patterns will follow a similar procedure exposure/development procedure, with the main difference being a pre-alignment step before exposure.

A sample to be exposed is first spin coated by PMMA using a vacuum chuck spinner than can turn at angular speeds up to 5000 rpm. The PMMA (MicroChem) comes in a variety of form of varying amounts of solvent (anisole). The concentration of the solvent, and the spin speed allow for control of the final PMMA layer thickness. The final thickness t_{PMMA} is generally related to the spin speed ω by

$$t_{\text{PMMA}} \propto \frac{1}{\sqrt{\omega}}. \quad (\text{A.1})$$

The final thickness is chosen for the particular application, but in our case we want to perform lift-off after the metal deposition. For a lift-off process, the general rule of thumb is to set the resist thickness at least three times that of the metal thickness used. A graph of thickness versus spin speed is shown in Figure A.1. After spin coating PMMA, the entire sample is placed onto a hot plate at 180 °C for 60 s to bake and drive out some of the solvent.

The PMMA coated sample is placed into the chamber of the department's shared JEOL 9700 SEM. The chamber is evacuated to low pressure. A rough pre-alignment is performed by moving the sample stage to the approximate location of the flake to be patterned. The SEM works together with a program called nano pattern generation system (NPGS) to translate the designed DesignCAD patterns into points of exposure with the electron beam. The program rasterizes the electron beam, exposing overlapping spots to fill an entire enclosed pattern element. The beam dwells at any particular point for an amount of time determined by the dose ($\sim 300 \mu\text{C}/\text{cm}^2$) and the measured beam current. After exposure, the sample is removed from the SEM, and ready for development. A developer solution is (1:3) methyl isobutyl ketone/IPA. The exposed sample is gently agitated in the developer solution for about 45 s, and then rinsed with IPA and DI water. What is left is the sample coated by PMMA except in the regions that have been exposed (where the PMMA is fully removed). Figure A.2 shows a sample of graphene with the alignment grid that has been through the development step.

For the patterning of devices, such as a Hall bar structure, there is another patterning step. In the same manner as the exposure of the alignment grid, the sample is aligned to the grid of now removed PMMA + 's. Carefully aligning the physical structure of the sample to the desired pattern alignment windows creates a registration match to the alignment grid. Generally, the Hall bar is patterned out of a larger flake of graphene, so the bar is left unexposed by the electron beam, and the surrounding area is fully exposed. After development, the Hall bar is the only structure left covered by the PMMA. An example of a sample after this stage is shown in Figure A.3.

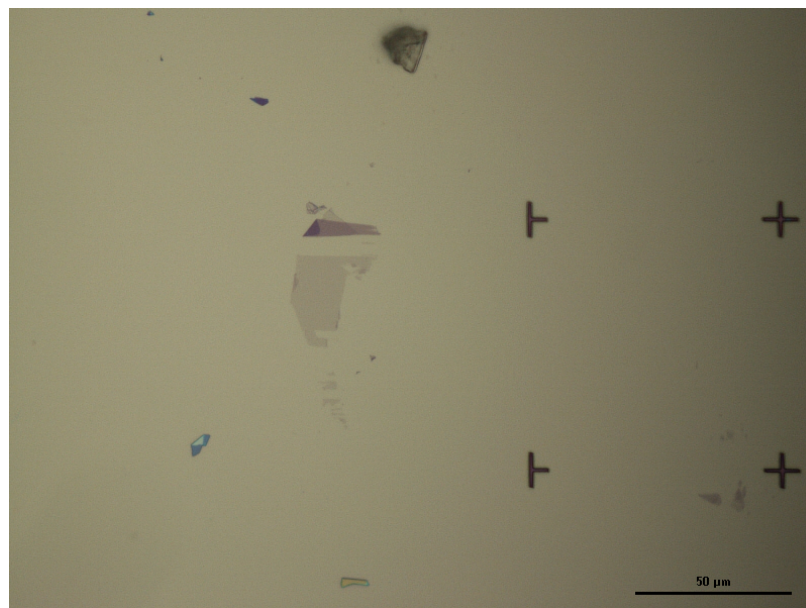


Figure A.2: Optical micrograph of a graphene flake coated by PMMA. The +’s on the right side are alignment mark that have been exposed and developed in the resist.



Figure A.3: Optical micrograph of a Hall bar patterned onto a graphene flake after the plasma etch of exposed graphene.



Figure A.4: Optical micrograph of a graphene/gold contact lines after developing the PMMA.

A.1.4 Oxygen Plasma Etching

This process was previously described (Chapter 3) for use in etching one side of as grown CVD graphene samples on copper. For graphene that has been patterned into a device structure, the oxygen plasma allows etching of the undesired portions of a graphene flake. Particularly for exfoliated graphene samples, there are scattered pieces of thicker graphite flakes as well. The etch process is run long enough (30 - 60 s) to remove the undesired graphene, and as much of the other thicker flakes as possible. PMMA is also etched by this process. This fact places a limit on the amount of time the etch can run before the entire PMMA layer is etched along with the desired graphene. A sample that has been etched by oxygen plasma is shown in Figure A.4.

A.1.5 Patterning of Contacts

After the graphene is etched by oxygen plasma, the PMMA is fully stripped. A new layer of PMMA is spin coated onto the sample for a new round of patterning. The basic technique is similar to that described previously. The same set of alignment grid marks are fully patterned and developed. For making contacts to the graphene device precise control on the alignment and placement is required. For the JEOL system used, this requires using a magnification of at least 1000 \times (94.8 μm field of view). These contacts are too small to be used for wire bonding, so another two layers of contact

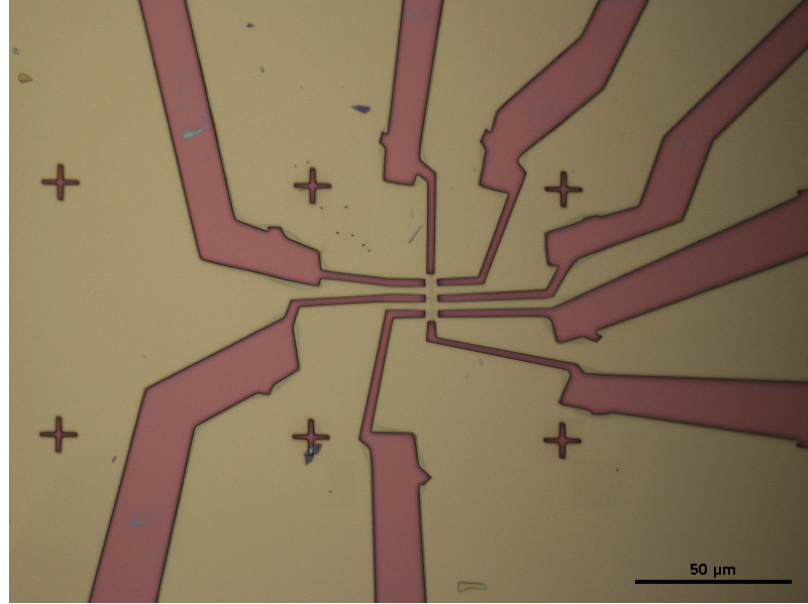


Figure A.5: Optical micrograph of the graphene Hall bar, with gold contact lines after evaporation.

lines are patterned on top of the first contacts. A small shift that occurs when changing magnification levels must be accounted for in the pattern design. The large contact lines and then wire bonding pads ($\sim 200 \times 200 \mu\text{m}^2$) are patterned at the lowest magnification level of the microscope. Figure A.5 shows the developed pattern of the contacts to graphene, and the overlapping pattern of the contact lines.

A.1.6 Metal Deposition

For metal contacts to graphene, we use gold, which is resistant to corrosion, and has a high electrical conductivity ($\sigma_{\text{Au}} = 4.5 \times 10^7 \text{ S/m}$ for bulk). Gold has poor adhesion to SiO_2 , so a very thin layer of another metal (Ti/Cr/Pd) is used as an intermediary between the substrate and the gold. The exposed/developed PMMA has a slight undercut which facilitates which allows for a lift-off process as long as the deposited metal is discontinuous between the open regions and the PMMA top surface. This requires that the metal deposition be anisotropic to avoid the metal conformal coating the entire sample surface. The choices of deposition method are then evaporation, either by electron beam, or thermally activated.

We most typically use the CVC e-beam evaporator in the MiRC Pettit clean room. This tool allows for multiple metal targets to be evaporated without having to evacuated the chamber between



Figure A.6: Optical micrograph of a graphene device after wire bonding to the gold contact pads.

runs. The sample to be deposited is mounted on a metal plate, placed in the deposition chamber, and pumped down to $\sim 6 \times 10^{-6}$ Torr. The adhesion layer metal (most often Ti) is deposited at a rate of 0.1 nm/s, for a final thickness of 5 nm. Then gold is deposited at a rate of 0.2 nm/s for a final thickness of 30 nm.

After the metal deposition, the sample is placed in a bath of acetone to strip the PMMA. Typically, we heat the solution on a hot plate to speed up the chemical process, but is kept well below the boiling point of acetone (56 °C). The sample is rinsed by IPA, which removes the remaining gold that has been lifted off the surface, and then rinsed by DI water. If the gold is not fully removed by the IPA, brief sonication can be used. This involves placing the sample in a beaker full of IPA which is then dipped into the sonication bath for less than a second. Sonication is a very harsh process, which has the ability to remove the graphene from the substrate completely. Figure A.6 shows a sample that has been deposited with metal, lifted-off, and cleaned.

A.1.7 Wire Bonding and Packaging

The electrical connection to the final graphene device is made from the gold contact pads to a wafer package. We most commonly use a ceramic DIP, which has a recess for the wafer, and elevated gold contacts that are connected to the pins. For a Si/SiO₂ backgated sample, the back of the substrate



Figure A.7: Optical micrograph of a Hall bar patterned onto a graphene flake after the developing the PMMA.

is scratched with a diamond scribe to remove some of the native oxide. The back of the wafer is coated with a small amount of quick drying silver paint, and then the wafer is carefully pressed into the recess of the package.

The sample contact pads are electrically connected to the package contact pads by means of wire bonding. We use a wedge type manual wire bonder with 1 mil aluminum wires. This creates wire contacts that are roughly 50 μm in size. Each sample contact is bonded to a separate package contact, and the package recess is connected to another package contact for making connection to the Si gate. Figure A.7 shows a graphene device that has been fully wire bonded to the external package.

REFERENCES

- [1] A. K. Geim and K. S. Novoselov, “The rise of graphene,” *Nat Mater* **6**, 183 (2007), 10.1038/nmat1849.
- [2] F. Schwierz, “Graphene transistors,” *Nat Nano* **5**, 487 (2010), 10.1038/nnano.2010.89.
- [3] Y.-M. Lin, C. Dimitrakopoulos, K. A. Jenkins, D. B. Farmer, H.-Y. Chiu, A. Grill, and P. Avouris, “100-GHz Transistors from Wafer-Scale Epitaxial Graphene,” *Science* **327**, 662 (2010) <http://www.sciencemag.org/content/327/5966/662.full.pdf>.
- [4] S. Bae, H. Kim, Y. Lee, X. Xu, J.-S. Park, Y. Zheng, J. Balakrishnan, T. Lei, H. Ri Kim, Y. I. Song, Y.-J. Kim, K. S. Kim, B. Ozyilmaz, J.-H. Ahn, B. H. Hong, and S. Iijima, “Roll-to-roll production of 30-inch graphene films for transparent electrodes,” *Nat Nano* **5**, 574 (2010), 10.1038/nnano.2010.132.
- [5] J.-C. Charlier, X. Gonze, and J.-P. Michenaud, “First-principles study of the stacking effect on the electronic properties of graphite(s),” *Carbon* **32**, 289 (1994).
- [6] L. Malard, M. Pimenta, G. Dresselhaus, and M. Dresselhaus, “Raman spectroscopy in graphene,” *Physics Reports* **473**, 51 (2009).
- [7] A. C. Ferrari, J. C. Meyer, V. Scardaci, C. Casiraghi, M. Lazzeri, F. Mauri, S. Piscanec, D. Jiang, K. S. Novoselov, S. Roth, and A. K. Geim, “Raman Spectrum of Graphene and Graphene Layers,” *Phys. Rev. Lett.* **97**, 187401 (2006).
- [8] D. L. Nika, S. Ghosh, E. P. Pokatilov, and A. A. Balandin, “Lattice thermal conductivity of graphene flakes: Comparison with bulk graphite,” *Applied Physics Letters* **94**, 203103 (2009).
- [9] N. Mounet and N. Marzari, “First-principles determination of the structural, vibrational and thermodynamic properties of diamond, graphite, and derivatives,” *Phys. Rev. B* **71**, 205214 (2005).
- [10] J. C. Meyer, A. K. Geim, M. I. Katsnelson, K. S. Novoselov, T. J. Booth, and S. Roth, “The structure of suspended graphene sheets,” *Nature* **446**, 60 (2007), 10.1038/nature05545.
- [11] C. R. Dean, A. F. Young, MericI, LeeC, WangL, SorgenfreiS, WatanabeK, TaniguchiT, KimP, K. L. Shepard, and HoneJ, “Boron nitride substrates for high-quality graphene electronics,” *Nat Nano* **5**, 722 (2010), 10.1038/nnano.2010.172.
- [12] R. Murali, Y. Yang, K. Brenner, T. Beck, and J. D. Meindl, “Breakdown current density of graphene nanoribbons,” *Applied Physics Letters* **94**, 243114 (2009).
- [13] C. Lee, X. Wei, J. W. Kysar, and J. Hone, “Measurement of the Elastic Properties and Intrinsic Strength of Monolayer Graphene,” *Science* **321**, 385 (2008).

- [14] R. R. Nair, P. Blake, A. N. Grigorenko, K. S. Novoselov, T. J. Booth, T. Stauber, N. M. R. Peres, and A. K. Geim, “Fine Structure Constant Defines Visual Transparency of Graphene,” *Science* **320**, 1308 (2008).
- [15] E. V. Castro, K. S. Novoselov, S. V. Morozov, N. M. R. Peres, J. M. B. L. dos Santos, J. Nilsson, F. Guinea, A. K. Geim, and A. H. C. Neto, “Biased Bilayer Graphene: Semiconductor with a Gap Tunable by the Electric Field Effect,” *Phys. Rev. Lett.* **99**, 216802 (2007).
- [16] V. M. Pereira, A. H. Castro Neto, and N. M. R. Peres, “Tight-binding approach to uniaxial strain in graphene,” *Phys. Rev. B* **80**, 045401 (2009).
- [17] S. Russo, M. Craciun, M. Yamamoto, A. Morpurgo, and S. Tarucha, “Contact resistance in graphene-based devices,” *Physica E: Low-dimensional Systems and Nanostructures* **42**, 677 (2010), 18th International Conference on Electron Properties of Two-Dimensional Systems.
- [18] F. Schedin, A. K. Geim, S. V. Morozov, E. W. Hill, P. Blake, M. I. Katsnelson, and K. S. Novoselov, “Detection of individual gas molecules adsorbed on graphene,” *Nat Mater* **6**, 652 (2007), 10.1038/nmat1967.
- [19] C. Chen, S. Rosenblatt, K. I. Bolotin, W. Kalb, P. Kim, I. Kymissis, H. L. Stormer, T. F. Heinz, and J. Hone, “Performance of monolayer graphene nanomechanical resonators with electrical readout,” *Nat Nano* **4**, 861 (2009), 10.1038/nnano.2009.267.
- [20] Y. Liu, B. Xie, Z. Zhang, Q. Zheng, and Z. Xu, “Mechanical Properties of Graphene Papers,” 2011 arXiv:1105.0138.
- [21] P. R. Wallace, “The Band Theory of Graphite,” *Physical Review* **71**, 622 (1947).
- [22] A. H. Castro Neto, F. Guinea, N. M. R. Peres, K. S. Novoselov, and A. K. Geim, “The electronic properties of graphene,” *Rev. Mod. Phys.* **81**, 109 (2009).
- [23] R. S. Deacon, K.-C. Chuang, R. J. Nicholas, K. S. Novoselov, and A. K. Geim, “Cyclotron resonance study of the electron and hole velocity in graphene monolayers,” *Phys. Rev. B* **76**, 081406 (2007).
- [24] K. S. Novoselov, A. K. Geim, S. V. Morozov, D. Jiang, Y. Zhang, S. V. Dubonos, I. V. Grigorieva, and A. A. Firsov, “Electric Field Effect in Atomically Thin Carbon Films,” *Science* **306**, 666 (2004).
- [25] K. S. Novoselov, A. K. Geim, S. V. Morozov, D. Jiang, M. I. Katsnelson, I. V. Grigorieva, S. V. Dubonos, and A. A. Firsov, “Two-dimensional gas of massless Dirac fermions in graphene,” *Nature* **438**, 197 (2005), 10.1038/nature04233.
- [26] P. L. McEuen, M. Bockrath, D. H. Cobden, Y.-G. Yoon, and S. G. Louie, “Disorder, Pseudospins, and Backscattering in Carbon Nanotubes,” *Phys. Rev. Lett.* **83**, 5098 (1999).
- [27] T. Ando, T. Nakanishi, and R. Saito, “Berry’s Phase and Absence of Back Scattering in Carbon Nanotubes,” *Journal of the Physical Society of Japan* **67**, 2857 (1998).
- [28] M. S. Dresselhaus and G. Dresselhaus, “Intercalation compounds of graphite,” *Advances in Physics* **51**, 1 (2002).
- [29] T. Fang, A. Konar, H. Xing, and D. Jena, “Carrier statistics and quantum capacitance of graphene sheets and ribbons,” *Applied Physics Letters* **91**, 092109 (2007).

- [30] K. S. Novoselov, A. K. Geim, S. V. Morozov, D. Jiang, Y. Zhang, S. V. Dubonos, I. V. Grigorieva, and A. A. Firsov, "Electric Field Effect in Atomically Thin Carbon Films," *Science* **306**, 666 (2004) <http://www.sciencemag.org/content/306/5696/666.full.pdf>.
- [31] Pachoud, A., Jaiswal, M., Ang, P. K., Loh, K. P., and Özyilmaz, B., "Graphene transport at high carrier densities using a polymer electrolyte gate," *EPL* **92**, 27001 (2010).
- [32] D. Kondo, S. Sato, K. Yagi, N. Harada, M. Sato, M. Nihei, and N. Yokoyama, "Low-Temperature Synthesis of Graphene and Fabrication of Top-Gated Field Effect Transistors without Using Transfer Processes," *Applied Physics Express* **3**, 025102 (2010).
- [33] Z. H. Ni, H. M. Wang, J. Kasim, H. M. Fan, T. Yu, Y. H. Wu, Y. P. Feng, and Z. X. Shen, "Graphene Thickness Determination Using Reflection and Contrast Spectroscopy," *Nano Letters* **7**, 2758 (2007).
- [34] P. Blake, E. W. Hill, A. H. C. Neto, K. S. Novoselov, D. Jiang, R. Yang, T. J. Booth, and A. K. Geim, "Making graphene visible," *Applied Physics Letters* **91**, 063124 (2007).
- [35] X. Li, W. Cai, J. An, S. Kim, J. Nah, D. Yang, R. Piner, A. Velamakanni, I. Jung, E. Tutuc, S. K. Banerjee, L. Colombo, and R. S. Ruoff, "Large-Area Synthesis of High-Quality and Uniform Graphene Films on Copper Foils," *Science* **324**, 1312 (2009) <http://www.sciencemag.org/content/324/5932/1312.full.pdf>.
- [36] X. Li, C. W. Magnuson, A. Venugopal, E. M. Vogel, R. S. Ruoff, and L. Colombo, "Large domain graphene," 2010 arXiv:1010.3903.
- [37] M. P. Levendorf, C. S. Ruiz-Vargas, S. Garg, and J. Park, "Transfer-Free Batch Fabrication of Single Layer Graphene Transistors," *Nano Letters* **9**, 4479 (2009).
- [38] L. Zhao, K. T. Rim, H. Zhou, R. He, T. F. Heinz, A. Pinczuk, G. W. Flynn, and A. N. Pasupathy, "Influence of copper crystal surface on the CVD growth of large area monolayer graphene," *Solid State Communications* **151**, 509 (2011).
- [39] A. Srivastava, C. Galande, L. Ci, L. Song, C. Rai, D. Jariwala, K. F. Kelly, and P. M. Ajayan, "Novel Liquid Precursor-Based Facile Synthesis of Large-Area Continuous, Single, and Few-Layer Graphene Films," *Chemistry of Materials* **22**, 3457 (2010) <http://pubs.acs.org/doi/pdf/10.1021/cm101027c>.
- [40] A. Guermoune, T. Chari, F. Popescu, S. S. Sabri, J. Guillemette, H. S. Skulason, T. Szkopek, and M. Siaj, "Chemical vapor deposition synthesis of graphene on copper with methanol, ethanol, and propanol precursors," *Carbon* **In Press, Accepted Manuscript** (2011).
- [41] Z. Z. Sun, Z. Yan, J. Yao, E. Beitler, Y. Zhu, and J. M. Tour, "Growth of graphene from solid carbon sources," *Nature* **468**, 549 (2010).
- [42] W. Zhang, P. Wu, Z. Li, and J. Yang, "First-Principles Thermodynamics of Graphene Growth on Cu Surface," 2011 arXiv:1101.3851.
- [43] S. S. Chen, L. Brown, M. Levendorf, W. W. Cai, S. Y. Ju, J. Edgeworth, X. S. Li, C. W. Magnuson, A. Velamakanni, R. D. Piner, J. Y. Kang, J. Park, and R. S. Ruoff, "Oxidation Resistance of Graphene-Coated Cu and Cu/Ni Alloy," *Acs Nano* **5**, 1321 (2011).

- [44] A. W. Robertson and J. H. Warner, “Hexagonal Single Crystal Domains of Few-Layer Graphene on Copper Foils,” *Nano Letters* **11**, 1182 (2011) <http://pubs.acs.org/doi/pdf/10.1021/nl104142k>.
- [45] Q. Yu, L. A. Jauregui, W. Wu, R. Colby, J. Tian, Z. Su, H. Cao, Z. Liu, D. Pandey, D. Wei, T. F. Chung, P. Peng, N. P. Guisinger, E. A. Stach, J. Bao, S.-S. Pei, and Y. P. Chen, “Control and characterization of individual grains and grain boundaries in graphene grown by chemical vapour deposition,” *Nat Mater* **10**, 443 (2011), 10.1038/nmat3010.
- [46] A. N. Sidorov, M. M. Yazdanpanah, R. Jalilian, P. J. Ouseph, R. W. Cohn, and G. U. Sumanasekera, “Electrostatic deposition of graphene,” *NANOTECHNOLOGY* **18** (2007).
- [47] C. Mattevi, H. Kim, and M. Chhowalla, “A review of chemical vapour deposition of graphene on copper,” *J. Mater. Chem.* **21**, 3324 (2011).
- [48] Z. Luo, T. Yu, J. Shang, Y. Wang, S. Lim, L. Liu, G. G. Gurzadyan, Z. Shen, and J. Lin, “Large-Scale Synthesis of Bi-layer Graphene in Strongly Coupled Stacking Order,” *Advanced Functional Materials* **21**, 911 (2011).
- [49] J. Hass, F. Varchon, J. E. Millán-Otoya, M. Sprinkle, N. Sharma, W. A. de Heer, C. Berger, P. N. First, L. Magaud, and E. H. Conrad, “Why Multilayer Graphene on 4H-SiC(000 $\bar{1}$) Behaves Like a Single Sheet of Graphene,” *Phys. Rev. Lett.* **100**, 125504 (2008).
- [50] J. Park, A. Reina, R. Saito, J. Kong, G. Dresselhaus, and M. Dresselhaus, “G’ band Raman spectra of single, double and triple layer graphene,” *Carbon* **47**, 1303 (2009).
- [51] K. N. Kudin, B. Ozbas, H. C. Schniepp, R. K. Prud’homme, I. A. Aksay, and R. Car, “Raman Spectra of Graphite Oxide and Functionalized Graphene Sheets,” *Nano Letters* **8**, 36 (2008) <http://pubs.acs.org/doi/pdf/10.1021/nl071822y>, PMID: 18154315.
- [52] D. Yang, A. Velamakanni, G. Bozoklu, S. Park, M. Stoller, R. D. Piner, S. Stankovich, I. Jung, D. A. Field, C. A. V. Jr., and R. S. Ruoff, “Chemical analysis of graphene oxide films after heat and chemical treatments by X-ray photoelectron and Micro-Raman spectroscopy,” *Carbon* **47**, 145 (2009).
- [53] Y. M. Zuev, W. Chang, and P. Kim, “Thermoelectric and Magnetothermoelectric Transport Measurements of Graphene,” *Phys. Rev. Lett.* **102**, 096807 (2009).
- [54] P. Wei, W. Bao, Y. Pu, C. N. Lau, and J. Shi, “Anomalous Thermoelectric Transport of Dirac Particles in Graphene,” *Phys. Rev. Lett.* **102**, 166808 (2009).
- [55] J. G. Checkelsky and N. P. Ong, “Thermopower and Nernst effect in graphene in a magnetic field,” *Phys. Rev. B* **80**, 081413 (2009).
- [56] X. Wu, Y. Hu, M. Ruan, N. K. Madiomanana, C. Berger, and W. A. de Heer, “Thermoelectric effect in high mobility single layer epitaxial graphene,” 2011 arXiv:1104.1248.
- [57] M. Cutler and N. F. Mott, “Observation of Anderson Localization in an Electron Gas,” *Phys. Rev.* **181**, 1336 (1969).
- [58] N. W. Ashcroft and D. N. Mermin, *Solid State Physics*, 1 ed. (Thomson Learning, Toronto, 1976).

- [59] E. H. Hwang, E. Rossi, and S. Das Sarma, “Theory of thermopower in two-dimensional graphene,” *Phys. Rev. B* **80**, 235415 (2009).
- [60] E. H. Hwang and S. Das Sarma, “Screening-induced temperature-dependent transport in two-dimensional graphene,” *Phys. Rev. B* **79**, 165404 (2009).
- [61] H. Cao, Q. Yu, L. A. Jauregui, J. Tian, W. Wu, Z. Liu, R. Jalilian, D. K. Benjamin, Z. Jiang, J. Bao, S. S. Pei, and Y. P. Chen, “Electronic transport in chemical vapor deposited graphene synthesized on Cu: Quantum Hall effect and weak localization,” *Applied Physics Letters* **96**, 122106 (2010).
- [62] G. U. Sumanasekera, C. K. W. Adu, B. K. Pradhan, G. Chen, H. E. Romero, and P. C. Eklund, “Thermoelectric study of hydrogen storage in carbon nanotubes,” *Phys. Rev. B* **65**, 035408 (2001).
- [63] V. Derycke, R. Martel, J. Appenzeller, and P. Avouris, “Carbon Nanotube Inter- and Intramolecular Logic Gates,” *Nano Letters* **1**, 453 (2001).
- [64] C. M. Aguirre, P. L. Levesque, M. Paillet, F. Lapointe, B. C. St-Antoine, P. Desjardins, and R. Martel, “The Role of the Oxygen/Water Redox Couple in Suppressing Electron Conduction in Field-Effect Transistors,” *Advanced Materials* **21**, 3087 (2009).
- [65] V. Chakrapani, J. C. Angus, A. B. Anderson, S. D. Wolter, B. R. Stoner, and G. U. Sumanasekera, “Charge Transfer Equilibria Between Diamond and an Aqueous Oxygen Electrochemical Redox Couple,” *Science* **318**, 1424 (2007) <http://www.sciencemag.org/content/318/5855/1424.full.pdf>.
- [66] W. Zhang, J. Ristein, and L. Ley, “Hydrogen-terminated diamond electrodes. II. Redox activity,” *Phys. Rev. E* **78**, 041603 (2008).
- [67] Y.-J. Yu, Y. Zhao, S. Ryu, L. E. Brus, K. S. Kim, and P. Kim, “Tuning the Graphene Work Function by Electric Field Effect,” *Nano Letters* **9**, 3430 (2009), PMID: 19719145.
- [68] H. E. Romero, N. Shen, P. Joshi, H. R. Gutierrez, S. A. Tadigadapa, J. O. Sofo, and P. C. Eklund, “n-Type Behavior of Graphene Supported on Si/SiO₂ Substrates,” *ACS Nano* **2**, 2037 (2008).
- [69] O. Leenaerts, B. Partoens, and F. M. Peeters, “Adsorption of H₂O , NH₃ , CO, NO₂ , and NO on graphene: A first-principles study,” *Phys. Rev. B* **77**, 125416 (2008).
- [70] S. K. Singh, M. K. Singh, M. K. Nayak, S. Kumari, S. Shrivastava, J. J. A. Gracio, and D. Dash, “Thrombus Inducing Property of Atomically Thin Graphene Oxide Sheets,” *ACS Nano* **5**, 4987 (2011) <http://pubs.acs.org/doi/pdf/10.1021/nn201092p>.
- [71] A. A. Balandin, S. Ghosh, W. Bao, I. Calizo, D. Teweldebrhan, F. Miao, and C. N. Lau, “Superior Thermal Conductivity of Single-Layer Graphene,” *Nano Letters* **8**, 902 (2008), PMID: 18284217.
- [72] W. Cai, A. L. Moore, Y. Zhu, X. Li, S. Chen, L. Shi, and R. S. Ruoff, “Thermal Transport in Suspended and Supported Monolayer Graphene Grown by Chemical Vapor Deposition,” *Nano Letters* **10**, 1645 (2010).

- [73] Z. Wang, R. Xie, C. T. Bui, D. Liu, X. Ni, B. Li, and J. T. L. Thong, "Thermal Transport in Suspended and Supported Few-Layer Graphene," *Nano Letters* **11**, 113 (2011).
- [74] J. H. Seol, I. Jo, A. L. Moore, L. Lindsay, Z. H. Aitken, M. T. Pettes, X. Li, Z. Yao, R. Huang, D. Broido, N. Mingo, R. S. Ruoff, and L. Shi, "Two-Dimensional Phonon Transport in Supported Graphene," *Science* **328**, 213 (2010) <http://www.sciencemag.org/content/328/5975/213.full.pdf>.
- [75] K. Saito, J. Nakamura, and A. Natori, "Ballistic thermal conductance of a graphene sheet," *Phys. Rev. B* **76**, 115409 (2007).
- [76] P. G. Klemens, "Theory of Thermal Conduction in Thin Ceramic Films," *International Journal of Thermophysics* **22**, 265 (2001), 10.1023/A:1006776107140.
- [77] D. G. Cahill, W. K. Ford, K. E. Goodson, G. D. Mahan, A. Majumdar, H. J. Maris, R. Merlin, and S. R. Phillpot, "Nanoscale thermal transport," *Journal of Applied Physics* **93**, 793 (2003).
- [78] D. G. Cahill, "Thermal conductivity measurement from 30 to 750 K: the 3 omega method," *Review of Scientific Instruments* **61**, 802 (1990).
- [79] B. W. Olson, S. Graham, and K. Chen, "A practical extension of the 3ω method to multilayer structures," **76**, 053901 (2005).
- [80] R. J. Stoner and H. J. Maris, "Kapitza conductance and heat flow between solids at temperatures from 50 to 300 K," *Phys. Rev. B* **48**, 16373 (1993).
- [81] J. Hone, M. Whitney, C. Piskoti, and A. Zettl, "Thermal conductivity of single-walled carbon nanotubes," *Phys. Rev. B* **59**, R2514 (1999).
- [82] Q. G. Zhang, B. Y. Cao, X. Zhang, M. Fujii, and K. Takahashi, "Influence of grain boundary scattering on the electrical and thermal conductivities of polycrystalline gold nanofilms," *Phys. Rev. B* **74**, 134109 (2006).
- [83] V. Singh, S. Sengupta, H. S. Solanki, R. Dhall, A. Allain, S. Dhara, P. Pant, and M. M. Deshmukh, "Probing thermal expansion of graphene and modal dispersion at low-temperature using graphene nanoelectromechanical systems resonators," *Nanotechnology* **21**, 165204 (2010).
- [84] A. Crossley, C. J. Sofield, J. P. Goff, A. C. I. Lake, M. T. Hutchings, and A. Menelle, "A study comparing measurements of roughness of silicon and SiO₂ surfaces and interfaces using scanning probe microscopy and neutron reflectivity," *Journal of Non-Crystalline Solids* **187**, 221 (1995), Amorphous Insulating Thin Films II.
- [85] B. E. Gillman and S. D. Jacobs, "Bound-Abrasive Polishers for Optical Glass," *Appl. Opt.* **37**, 3498 (1998).
- [86] G. B. M. Fiege, A. Altes, R. Heiderhoff, and L. J. Balk, "Quantitative thermal conductivity measurements with nanometre resolution," *Journal of Physics D: Applied Physics* **32**, L13 (1999).
- [87] K. Kim, J. Chung, J. Won, O. Kwon, J. S. Lee, S. H. Park, and Y. K. Choi, "Quantitative scanning thermal microscopy using double scan technique," *Applied Physics Letters* **93**, 203115 (2008).

- [88] H. Fischer, “Quantitative determination of heat conductivities by scanning thermal microscopy,” *Thermochimica Acta* **425**, 69 (2005).
- [89] X. Li, C. W. Magnuson, A. Venugopal, J. An, J. W. Suk, B. Han, M. Borysiak, W. Cai, A. Velamakanni, Y. Zhu, L. Fu, E. M. Vogel, E. Voelkl, L. Colombo, and R. S. Ruoff, “Graphene Films with Large Domain Size by a Two-Step Chemical Vapor Deposition Process,” *Nano Letters* **10**, 4328 (2010) <http://pubs.acs.org/doi/pdf/10.1021/nl101629g>.
- [90] A. Venugopal, J. Chan, X. Li, C. W. Magnuson, W. P. Kirk, L. Colombo, R. S. Ruoff, and E. M. Vogel, “Effective mobility of single-layer graphene transistors as a function of channel dimensions,” *Journal of Applied Physics* **109**, 104511 (2011).
- [91] J. An, E. Voelkl, J. W. Suk, X. Li, C. W. Magnuson, L. Fu, P. Tiemeijer, M. Bischoff, B. Freitag, E. Popova, and R. S. Ruoff, “Domain (Grain) Boundaries and Evidence of “Twinlike” Structures in Chemically Vapor Deposited Grown Graphene,” *ACS Nano* **5**, 2433 (2011) <http://pubs.acs.org/doi/pdf/10.1021/nn103102a>.
- [92] K. S. Novoselov, Z. Jiang, Y. Zhang, S. V. Morozov, H. L. Stormer, U. Zeitler, J. C. Maan, G. S. Boebinger, P. Kim, and A. K. Geim, “Room-Temperature Quantum Hall Effect in Graphene,” *Science* **315**, 1379 (2007) <http://www.sciencemag.org/content/315/5817/1379.full.pdf>.
- [93] X. Du, I. Skachko, F. Duerr, A. Luican, and E. Y. Andrei, “Fractional quantum Hall effect and insulating phase of Dirac electrons in graphene,” *Nature* **462**, 192 (2009), 10.1038/nature08522.
- [94] K. I. Bolotin, F. Ghahari, M. D. Shulman, H. L. Stormer, and P. Kim, “Observation of the fractional quantum Hall effect in graphene,” *Nature* **462**, 196 (2009), 10.1038/nature08582.
- [95] F. Bonaccorso, Z. Sun, T. Hasan, and A. C. Ferrari, “Graphene photonics and optoelectronics,” *Nat Photon* **4**, 611 (2010), 10.1038/nphoton.2010.186.
- [96] J. W. McClure, “Diamagnetism of Graphite,” *Phys. Rev.* **104**, 666 (1956).
- [97] W. Zhu, Q. W. Shi, X. R. Wang, J. Chen, J. L. Yang, and J. G. Hou, “Shape of Disorder-Broadened Landau Subbands in Graphene,” *Phys. Rev. Lett.* **102**, 056803 (2009).
- [98] V. P. Gusynin and S. G. Sharapov, “Unconventional Integer Quantum Hall Effect in Graphene,” *Phys. Rev. Lett.* **95**, 146801 (2005).
- [99] Y. Zhang, Z. Jiang, J. P. Small, M. S. Purewal, Y.-W. Tan, M. Fazlollahi, J. D. Chudow, J. A. Jaszczak, H. L. Stormer, and P. Kim, “Landau-Level Splitting in Graphene in High Magnetic Fields,” *Phys. Rev. Lett.* **96**, 136806 (2006).
- [100] Z. Jiang, Y. Zhang, H. L. Stormer, and P. Kim, “Quantum Hall States near the Charge-Neutral Dirac Point in Graphene,” *Phys. Rev. Lett.* **99**, 106802 (2007).
- [101] Y. J. Song, A. F. Otte, Y. Kuk, Y. Hu, D. B. Torrance, P. N. First, W. A. de Heer, H. Min, S. Adam, M. D. Stiles, A. H. MacDonald, and J. A. Stroscio, “High-resolution tunnelling spectroscopy of a graphene quartet,” *Nature* **467**, 185 (2010), 10.1038/nature09330.

- [102] S. Jung, G. M. Rutter, N. N. Klimov, D. B. Newell, I. Calizo, A. R. Hight-Walker, N. B. Zhitenev, and J. A. Stroscio, “Evolution of microscopic localization in graphene in a magnetic field from scattering resonances to quantum dots,” *Nat Phys* **7**, 245 (2011), 10.1038/nphys1866.
- [103] J. G. Checkelsky, L. Li, and N. P. Ong, “Zero-Energy State in Graphene in a High Magnetic Field,” *Phys. Rev. Lett.* **100**, 206801 (2008).
- [104] L. Zhang, Y. Zhang, M. Khodas, T. Valla, and I. A. Zaliznyak, “Metal to Insulator Transition on the $N =$ Landau Level in Graphene,” *Phys. Rev. Lett.* **105**, 046804 (2010).
- [105] K. Bolotin, K. Sikes, Z. Jiang, M. Klima, G. Fudenberg, J. Hone, P. Kim, and H. Stormer, “Ultrahigh electron mobility in suspended graphene,” *Solid State Communications* **146**, 351 (2008).
- [106] C. R. Dean, A. F. Young, P. Cadden-Zimansky, L. Wang, H. Ren, K. Watanabe, T. Taniguchi, P. Kim, J. Hone, and K. L. Shepard, “Multicomponent fractional quantum Hall effect in graphene,” *Nat Phys* **advance online publication** (2011), 10.1038/nphys2007.
- [107] V. P. Gusynin, S. G. Sharapov, and J. P. Carbotte, “Anomalous Absorption Line in the Magneto-Optical Response of Graphene,” *Phys. Rev. Lett.* **98**, 157402 (2007).
- [108] Z. Jiang, E. A. Henriksen, L. C. Tung, Y.-J. Wang, M. E. Schwartz, M. Y. Han, P. Kim, and H. L. Stormer, “Infrared Spectroscopy of Landau Levels of Graphene,” *Phys. Rev. Lett.* **98**, 197403 (2007).
- [109] M. L. Sadowski, G. Martinez, M. Potemski, C. Berger, and W. A. de Heer, “Landau Level Spectroscopy of Ultrathin Graphite Layers,” *Phys. Rev. Lett.* **97**, 266405 (2006).
- [110] E. A. Henriksen, P. Cadden-Zimansky, Z. Jiang, Z. Q. Li, L.-C. Tung, M. E. Schwartz, M. Takita, Y.-J. Wang, P. Kim, and H. L. Stormer, “Interaction-Induced Shift of the Cyclotron Resonance of Graphene Using Infrared Spectroscopy,” *Phys. Rev. Lett.* **104**, 067404 (2010).
- [111] F. T. Vasko and V. Ryzhii, “Photoconductivity of intrinsic graphene,” *Phys. Rev. B* **77**, 195433 (2008).
- [112] F. Wang, Y. Zhang, C. Tian, C. Girit, A. Zettl, M. Crommie, and Y. R. Shen, “Gate-Variable Optical Transitions in Graphene,” *Science* **320**, 206 (2008) <http://www.sciencemag.org/content/320/5873/206.full.pdf>.
- [113] G. Hwang, S. Haliyo, and S. Regnier, “Infrared-photovoltaic properties of graphene revealed by electro-osmotic spray direct patterning of electrodes,” *Micro & Nano Letters* **5**, 140 (2010).
- [114] W. Xu, Y. Gong, L. Liu, H. Qin, and Y. Shi, “Can graphene make better HgCdTe infrared detectors?,” *Nanoscale Research Letters* **6**, 250 (2011).
- [115] W. Kohn, “Cyclotron Resonance and de Haas-van Alphen Oscillations of an Interacting Electron Gas,” *Phys. Rev.* **123**, 1242 (1961).

VITA

Dan was born in Florida. He grew up a Florida boy, and graduated from the University of Florida, with degrees in physics and mathematics. Go Gators.

Then he decided he should probably leave the state for graduate school. Eventually he realized this was a bad decision, but decided he had to stick it out in Georgia. After working in vain for years, he found a cool new advisor that helped him graduate.